Doctoral Dissertation

DYNAMIC DRAG EFFECTS ON DISLOCATIONS AND GRAIN BOUNDARIES IN DISCRETE SYSTEM

Soon Kim

Department of Mechanical Engineering

Graduate School of UNIST

2020

DYNAMIC DRAG EFFECTS ON DISLOCATIONS AND GRAIN BOUNDARIES IN DISCRETE SYSTEM

Soon Kim

Department of Mechanical Engineering

Graduate School of UNIST

Dynamic Drag Effects on Dislocations and Grain Boundaries in Discrete System

A thesis/dissertation
submitted to the Graduate School of UNIST
in partial fulfillment of the
requirements for the degree of
Doctor of Philosophy

Soon Kim

12. 12. 2019

Approved by

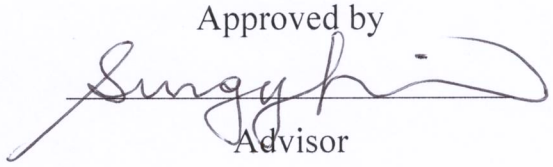

Advisor

Sung Youb Kim

Dynamic Drag Effects on Dislocations and Grain Boundaries in Discrete System

Soon Kim

This certifies that the thesis/dissertation of Soon Kim is approved.

12/12/2019

signature

Advisor: Sung Youb Kim

signature

Prof. Joo Hwan Oh

signature

Prof. Hayoug Chung

signature

Prof. Hyung-Joon Shin

signature

Prof. Seunghwa Ryu

Abstract

Macroscopic plastic deformation is an irreversible consequence proceeded by the motion of dislocations under applied stress in micro- and nano-scales. Therefore, numerous efforts to understand the plastic deformation has finally led one to study the dynamics of individual dislocation. According to the continuum theory, the drag force leads to a linear relationship between the dislocation velocity and the stress. However, a discrete nature of the dislocation core induces *nonlinear* drag force on the moving dislocation in reality. Therefore, the continuum approach is limited in its ability to describe the dislocation motion under the general loading conditions although it has been widely used so far in mesoscale dislocation dynamics (DD) simulation.

In the first part of the dissertation (Chapter 1~4), I focus on fundamentals of the drag force with considering the discrete nature of dislocation and propose a theoretical framework to describe the dislocation motion including the nonlinear drag effect. And the proposed model is supported by molecular dynamics (MD) simulations. In a discrete medium that consists of atoms, the dislocation glides with emitting elastic waves and they are scattered around the dislocation core by various sources. Therefore, the phonon scattering is the dominant drag source and determines the dynamic behaviors of a dislocation. And by extension, the theoretical model is applied to the low-angle grain boundary (LAGB) given that it characterized as an array of dislocations. As a result, the proposed model can describe the dynamics of both dislocation and LAGB in the discrete system and expect unusual behaviors that do not follow the continuum theory.

In the second part of the dissertation (Chapter 5), a deeper analysis of the drag force is carried out in the frame of Eshelbian mechanics. Since the origin of drag force acting on the dislocation stems from interaction between the dislocation and phonons, the drag force is analytically derived by adopting the dislocation-phonon coordinate system. As a result, it is proved that the drag force breaks a path-independent behavior of *J*-integral and its magnitude is determined by structural properties of the dislocation. This reconfirms that the drag force is closely related to the discreteness nature of dislocation.

In this regard, the proposed approach sheds light on the essence of drag effect and further provides an integrated viewpoint on describing various drag mechanisms. Hence, I expect that the present work elucidates the fundamentals of dislocation dynamics in nanoscale in which the discreteness of medium may be important, and contributes to more realistic prediction of material plasticity.

Contents

List of Tables

List of Figures

Chapter 1
Introduction

1.1 Dislocation

Historically, the plastic deformation of materials has played an important role in various manufacturing processes. Since the plastic deformation of most materials begins after 3% strain (~0.2% for metals), it practically governs total deformation of the materials so that understanding the plastic deformation is indispensable. During the plastic deformation, the energy dissipates and it has been proved that dislocations behave as plasticity carriers and the dissipation sources by various experiments. In addition to the experiments, theoretical analysis of the dislocation has been systematically underpinned. In the early twentieth century, the concept of dislocation was first introduced by Volterra (1907)[1] (Fig. 1.1) and the close relation between dislocations and plastic deformation was recognized in the 1930s. In the 1960s, direct observation of dislocations became possible as shown in Fig. 1.2, and since then there have been a lot of efforts to connect between the theories and experiment results.

A development of computer simulations has enabled to study a motion of single dislocation and its mechanical behaviors under external loads[2-4]. Early studies that use the computer simulations have, in particular, focused on measuring mobility and Peierls stress of dislocations depending on their types. Numerous studies have pointed out that both the mobility and Peiers stress are strongly influenced by the dislocation core structures[5-8].

The dislocation core has drawn a lot of attention from many physicists and material scientists because mechanical response in this region does not follow linear elasticity theory. There are two main reasons why the linear elasticity theory cannot describe the core region. First, a strain field applied in the core is too large to use the linear elasticity theory[9]. Second, if the strain field is applied in finite region whose size is limited, an elastic response in a specific point depends not only on stress at that point but also at surrounding volume around the point, so the response is non-local. This behavior comes from discrete nature of the dislocation core[10]. Due to these

theoretical difficulties, atomistic[3,11] and density functional theory (DFT) simulations[12] have been emerged as tools for deeper understanding of the core region since the late twentieth century. In addition to simulation techniques, however, theoretical descriptions of dislocation mobility have been tried by simplifying the actual core structure[13,14] or assuming piecewise harmonic interatomic potential[15].

As the number of dislocations increases in a system, the core of gliding dislocation interacts with other dislocations and/or other defects. As a result, dislocations are created, annihilated, or stored within a grain. These processes determine material microstructures and are closely related to material ductility. As the computer performance has further developed, a lot of attempts to describe the collective behaviors of dislocations have been made on. By considering the long-range interactions and reactions between dislocation segments, the flow curve could be reproduced and this enabled multiscale analysis of material plasticity from nano- to macro-scales. For the multiscale analysis, the dislocation density becomes an important input parameter[16-20]. Especially, in order to predict plastic behaviors of the material under extreme conditions such as large strain or strain rate, the constitutive models should be more carefully handled than under ordinary conditions because the dislocation density abruptly increases[21-23].

Nowadays, many attempts have been actively done to calculate the dislocation density and predict its evolution by using mesoscale dislocation dynamics (DD) simulations[24-26]. To simulate DD, input parameters that characterize each dislocation segment in nanosacle are precedently required. Therefore, without deep understanding of characteristics of individual dislocation, the dislocation density-based constitutive models might experience severe reduce in their accuracy under the extreme conditions.

1.2 Discrete nature of a dislocation

The dislocation mobility M_{dis} connects the dislocation velocity v with the applied stress σ_{app} by Eq. (1.1).

$$v = M_{dis}\sigma_{app}. \tag{1.1}$$

Here, M_{dis} is a function of thermal properties and characteristics of the dislocation. Alternatively, Eq. (1.1) can be described by $\sigma_{app} = B_{dis}v$, where $B_{dis} = 1/M_{dis}$ is a drag coefficient. Interestingly, the dislocation mobility is determined by a dislocation core region although the

radius of its area is extremely small, only a few atomic distances. However, there is theoretical difficulty in studying this region because of its nonlinear behaviors. This nonlinearity is closely related to the discrete nature of the dislocation core, and thus it has revealed the limitations of continuum theory, particularly when the dislocation speed approaches the shear wave speed. According to continuum theory, the dislocation cannot move faster than the transverse shear wave speed C_t, because the energy density and stress field of a moving dislocation diverge at C_t[27,28]. In other words, the dislocation core radiates sound waves that require a supply of infinite energy to satisfy the energy balance. As a result, the shear wave speed has been regarded as a barrier that the dislocation cannot overcome[29,30].

However, the development of atomistic simulations has enabled researchers to simulate individual dislocations on the atomic scale. These simulation studies have shown that dislocations can move faster than C_t[31-33] and in particular, edge dislocations can move even faster than the longitudinal shear wave speed, C_l[34,35]. With these observations, the discrete lattice dynamics (DLD) theory has been suggested as a theoretical method to consider the discrete nature of dislocation cores[36-38]. The DLD theory does not require the singularity that is inevitable in continuum theory. This advantage has provided a theoretical way to explain the motion of dislocation cores when their speed is close to or beyond the shear wave speed. Generally, in this speed regime, phonons are emitted from the dislocation core, and their interactions with the lattice system are significant in determining the relationship between the dislocation speed and applied stress, i.e., the mobility law. As a result of interactions between phonons and the lattice, energy dissipates from the dislocation core, which causes drag on the moving dislocation.

1.3 Drag mechanisms

While a dislocation is set in motion by the external load, a force acts on the moving dislocation in the opposite direction to the load, which keeps its speed constant. This force is defined as the *drag force*. In general, the drag force occurs by the interaction between the moving dislocation and phonons around it. Therefore, in order to understand the drag force acting on the dislocation, the sources of phonon emissions must be revealed. Among various types of phonon sources, we introduce three major ones in the following subsections.

1.3.1 Flutter drag

First, the phonons are emitted by a scattering of elementary excitations caused by external sources. In many cases, temperature as the dominant excitation source induces oscillations in the dislocation, which radiates phonons. This behavior is called *flutter drag*[28,39]. As the phonons impinge on the dislocation, the phonons are scattered and the momentum is transferred to the dislocation. As a result, the dislocation oscillates and secondary waves are emitted from it. This process is described in Fig. 1.3. Recently, Chen et al. (2017)[40] showed that thermal phonons reduce the energy stored in the cores of dislocation arrays, induce the emission of secondary phonon waves, and disperse the waves around the arrays. Since this mechanism depends on the internal degrees of freedom of the dislocation, it is sensitive to temperature. Increasing temperature causes more phonons to radiate from the core, which increases the dissipation.

The influence of fluttering mechanism on the dislocation motion can be understood based on linear elasticity theory[28]. Consider a screw dislocation whose length is L along z axis. Then, a force equilibrium equation becomes

$$\frac{\partial^2 u_z}{\partial x^2}+\frac{\partial^2 u_z}{\partial y^2}=\frac{1}{C_t^2}\frac{\partial^2 u_z}{\partial t^2}, \tag{1.2}$$

where $C_t=\sqrt{\mu/\rho}$ is a transverse shear wave velocity, μ is a shear modulus, and ρ is a density of the system. If the coordinate system $x'y'z'$ attached to the dislocation glides along positive x direction in xz plane with a velocity v, the moving frame is related to the stationary frame by the Lorentz transformation. As a result,

$$\begin{aligned} x' &= \frac{x-vt}{\sqrt{1-(v/C_t)^2}} \\ y' &= y \\ z' &= z \\ t' &= \frac{t-vx/C_t^2}{\sqrt{1-(v/C_t)^2}} \end{aligned} \tag{1.3}$$

By using the Eq. (1.3), the force equilibrium equation in the moving frame can be derived as

$$\frac{\partial^2 u_z}{\partial x'^2}+\frac{\partial^2 u_z}{\partial y'^2}=\frac{1}{C_t^2}\frac{\partial^2 u_z}{\partial t'^2}. \tag{1.4}$$

Then, the energy density of a moving screw dislocation with including the kinetic energy density becomes

$$w = \frac{\mu}{2}\left[\left(\frac{\partial u_z}{\partial x}\right)^2 + \left(\frac{\partial u_z}{\partial y}\right)^2 + \frac{1}{C_t^2}\left(\frac{\partial u_z}{\partial t}\right)^2\right] = \frac{\mu}{2\gamma^2}\left[\left(\frac{\partial u_z}{\partial x'}\right)^2 + \left(\frac{\partial u_z}{\partial y'}\right)^2 + \frac{v^2}{C_t^2}\left\{\left(\frac{\partial u_z}{\partial x'}\right)^2 - \left(\frac{\partial u_z}{\partial y'}\right)^2\right\}\right]. \tag{1.5}$$

This leads an infinitesimal total energy of the system in an infinite slab, whose thickness is δy (in *y* direction) and depth is *L* (in *z* direction), to become

$$dW = \gamma L \delta y \int_{-\infty}^{\infty} w\, dx' = \gamma dW_0, \tag{1.6}$$

where dW_0 is an infinitesimal strain energy of the stationary screw dislocation.

Now consider a situation that a uniformly moving screw dislocation with a velocity, v ($\ll C_t$) is suddenly accelerated to $v + \Delta v$ at *t=0* by an external load. This causes energy change per unit dislocation length as much as

$$\frac{\Delta W}{L} = \frac{W - W_0}{L} \approx \frac{W_0}{2L}\frac{2v\Delta v}{C_t^2} = \frac{\mu b^2 v \Delta v}{4\pi C_t^2}\ln\frac{C_t t}{b}, \tag{1.7}$$

where *b* is Burgers vector. If the dislocation velocity does not change, the back shear stress, $\Delta\sigma$, must be balanced by an external shear stress to satisfy the force equilibrium condition. Since $\Delta\sigma$ does work at a rate$\Delta\sigma b v$, the dissipation power must be equal to energy change per unit time as

$$\Delta\sigma b v = \frac{\partial}{\partial t}\left(\frac{\Delta W}{L}\right). \tag{1.8}$$

As a result,

$$\Delta\sigma = \frac{\mu b \Delta v}{4\pi C_t^2 t} \tag{1.9}$$

is derived. To be more specific, however, since the stress wave propagates with a speed C_t in a continuous solid, the system does not feel any stress if $t < b/C_t$. Therefore,

$$\Delta\sigma = \begin{cases} 0 & \left(t < \dfrac{b}{C_t}\right) \\ \dfrac{\mu b \Delta v}{4\pi C_t^2 t} & \left(t > \dfrac{b}{C_t}\right) \end{cases} \tag{1.10}$$

By using a linear response theory, the shear stress at *t* can be derived as

$$\sigma(t) = \int_{-\infty}^{t-b/C_t} \frac{d\,\Delta\sigma(t-\tau)}{d\tau} d\tau = \frac{\mu b}{4\pi C_t^2} \int_{-\infty}^{t-b/C_t} \frac{d\,v(\tau)}{d\tau} \frac{d\tau}{t-\tau} . \tag{1.11}$$

If we apply Eq. (1.11) to an oscillating dislocation with amplitude $x(t) = Asin(\Omega t)$ in *xz* plane,

$$\sigma(t) = \frac{\mu b A \Omega^2}{4\pi C_t^2} \int_{-\infty}^{t-b/C_t} \frac{\sin \Omega\tau}{t-\tau} d\tau \ . \tag{1.12}$$

Here, we assume that $\Omega A \ll C_t$ and $\Omega b \ll C_t$. By using characteristics of trigonometric functions, Eq. (1.12) becomes

$$\begin{aligned} \sigma(t) &= \frac{\mu b A \Omega^2}{4\pi C_t^2} \left(\sin \Omega t \int_{\Omega b/C_t}^{\infty} \frac{\cos w}{w} dw - \cos \Omega t \int_{\Omega b/C_t}^{\infty} \frac{\sin w}{w} dw \right) \\ &\approx \frac{\mu b A \Omega^2}{4\pi C_t^2} \left(\ln \frac{C_t}{1.78 \Omega b} \right) \sin \Omega t - \frac{\mu b A \Omega^2}{8 C_t^2} \cos \Omega t \ . \end{aligned} \tag{1.13}$$

Since the first term of Eq. (1.13) is proportional to $\ddot{x}$, it represents an inertial force on the oscillating dislocation. On the contrary, the second term is proportional to $\dot{x}$, it acts as a damping force, or *drag force*. The drag force radiates energy per unit length of the dislocation as much as

$$\frac{dW}{L} = \sigma_{drag} b (\dot{x} dt) = \frac{\mu b^2 A^2 \Omega^3}{8 C_t^2} \cos^2 \Omega t \, dt \, , \tag{1.14}$$

and the resulting drag coefficient becomes

$$B_{dis} = \frac{\dot{W}}{\dot{x}^2} = \frac{\mu b^2 \Omega}{8 C_t^2} . \tag{1.15}$$

In addition, the fluttering mechanism can be analyzed through quantum mechanical approach. Due to the energy conservation, the frequency of incoming phonon $\omega_{q'}$ is shifted to outgoing phonon frequency $\omega_{q''}$ after the energy transfer to dislocation $\hbar(\omega_{q'} - \omega_{q''})$, where q', q''

are wave vectors of incoming and outgoing phonons, respectively. Since the momentum must be also conserved, the dislocation frequency becomes $\Omega_q = \omega_{q'} - \omega_{q''}$. Then, the drag coefficient corresponding to the flutter drag can be derived by dividing the energy dissipation per unit time D by the square of the dislocation velocity. As a result, Eq. (1.16) is derived[41].

$$B_{dis}(v,T) \equiv \frac{D}{v^2} = \frac{1}{v^2} \sum_{q',q''} \hbar\Omega_q \left(n_{q'} - n_{q''}\right) W_{q',q''}\,, \tag{1.16}$$

where $n_{q'}$ and $n_{q''}$ are equilibrium incoming/outgoing phonon distribution functions so that $n_{q'} = \left[\exp\left(\hbar\omega_{q'}/k_B T\right) - 1\right]^{-1}$. And $W_{q',q''}$ is the probability of phonon transition from q' to q'' per unit time and unit dislocation length.

1.3.2 Phonon wind

At finite temperature that is comparable or higher than the Debye temperature, the scattering of phonons due to anharmonic strain field around the dislocation core becomes a dominant drag mechanism rather than the fluttering effect[42]. When a dislocation is moving in the phonon gas, the dislocation strain field disturbs the equilibrium state of phonon gas and phonon flux impinging on the dislocation becomes asymmetrical[43]. As a result, the phonons scattered by the strain field imparts a momentum to the dislocation in opposite to its moving direction. This drag is called *phonon wind*. Under the phonon wind mechanism, the drag coefficient is expressed by[42,44,45]

$$B_{dis}(v,T) = \frac{4\pi}{\hbar v^2} \sum_{s',s''} \sum_{q',q''} \int d^2 q \Omega_q \left|\Gamma_{s',s''}(\vec{q}',\vec{q}'',\vec{q})\right|^2 \left(n_{q''} - n_{q'}\right) \delta(\vec{q}' - \vec{q}'' - \vec{q}) \delta(\omega_{q'} - \omega_{q''} - \Omega_q), \tag{1.17}$$

where s', s'' represent polarizations of the wave vectors and $\vec{q}$ is a wave vector that is related to the dislocation strain field. Here, $n_{q'}$, $n_{q''}$ controls the number of scattering events per unit time. And $\Gamma_{s',s''}$ physically implies a scattering probability that depends on the dislocation displacement gradient with high-order elastic constants. Lastly, the delta terms in Eq. (1.17) represent momentum and energy conservations, respectively. A detailed derivation of Eq. (1.17) can be found in Ref. 46.

1.3.3 Radiation drag

Unlike above two drag mechanisms, the dissipation process can occur even when there are no thermal sources or external excitations. In a discrete system, when a dislocation overcomes the Peierls barrier, the changes in its core and irregular motion radiate elastic waves. This mechanism, called *radiation drag*[47-49], occurs solely due to the discreteness of the system. Thus, the magnitude of the drag depends on the speed of the dislocation rather than the temperature. Especially, by considering radiation drag, the existence of a critical speed far below the shear wave speed can be proved by both DLD theory[36,50] and molecular dynamics simulations[38].

By using the DLD theory suggested by Kresse and Truskinovsky (2003)[47], we assume that system consists of one-dimensional atomic chain attached at distance ε to double-well potential $w(\tilde{u}_n)$ where $\tilde{u}_n$ is a displacement of *n*-th atom from its equilibrium position. The system is described in Fig. 1.4 and it follows the Euler-Lagrange equation of Eq. (1.18).

$$\rho\varepsilon\ddot{\tilde{u}}_n - \frac{E}{\varepsilon}\left(\tilde{u}_{n+1} - 2\tilde{u}_n + \tilde{u}_{n-1}\right) + \varepsilon\left[w'(\tilde{u}_n) - \tilde{\sigma}\right] = 0\,. \tag{1.18}$$

$$w(\tilde{u}_n) = \begin{cases} \dfrac{1}{2}c\tilde{u}_n^2 & (\tilde{u}_n < b_c) \\ \dfrac{1}{2}c\left(\tilde{u}_n - b\right)^2 & (\tilde{u}_n > b_c) \end{cases} \tag{1.19}$$

where ρ is a density of the system, *E* is an elastic stiffness of the spring that connects between atoms, $\tilde{\sigma}_n$ is applied stress, and *b* is a distance between two atoms when $\tilde{\sigma}_n = 0$. Physically, $w(\tilde{u}_n)$ corresponds to the Peierls potential of the dislocation whose stiffness is *c*. Therefore, $\tilde{\sigma}$ makes the dislocation core glide to neighboring Peierls valley, or phase transition. Here, we assume that the atomic bond is broken when $\tilde{u}_n$ exceeds a critical value $b_c(=b/2)$ and atoms interact each other only by harmonic way. Under the plane wave assumption moving with the uniform speed $\tilde{v}$, Eq. (1.18) is transformed to Eq. (1.20) by adopting a moving coordinate $\tilde{x} = \varepsilon n - \tilde{v}t$.

$$\rho\varepsilon\tilde{v}^2\frac{d^2\tilde{u}}{dx^2} - \frac{E}{\varepsilon}\left(\tilde{u}(\tilde{x}+\varepsilon) - 2\tilde{u}(\tilde{x}) + \tilde{u}(\tilde{x}-\varepsilon)\right) + \varepsilon\left[c\tilde{u}(\tilde{x}) - \tilde{\sigma} - bcH(-\tilde{x})\right] = 0\,, \tag{1.20}$$

where *H* is the Heaviside step function. If the parameters in Eq. (1.20) are normalized as

$$x = \tilde{x}/\varepsilon,\ u = \tilde{x}/b,\ v = \tilde{v}\sqrt{\rho/E},\ \sigma = \tilde{\sigma}/bc\,, \tag{1.21}$$

Eq. (1.20) becomes

$$v^2 \frac{d^2u}{dx^2} - \frac{E}{\varepsilon}\left(u(x+1) - 2u(x) + u(x-1)\right) + \Omega^2\left[u(x) - \sigma - H(-x)\right] = 0\,, \tag{1.22}$$

where $\Omega = \varepsilon\sqrt{c/E}$. To satisfy admissibility, the following conditions are required[47].

$$u(x)\begin{cases} > \frac{1}{2} & (x<0) \\ = \frac{1}{2} & (x=0) \\ < \frac{1}{2} & (x>0) \end{cases} \tag{1.23}$$

In addition, since a region passed by the dislocation long before moves by *b* relative to their initial position, we obtain $u(x) \to \sigma + 1$ as $x \to -\infty$. On the contrary, a region where the dislocation does not pass by yet supports only the external stress, we obtain $u(x) \to \sigma$ as $x \to \infty$.

An analytic solution $u(x)$ can be obtained by applying the Fourier transform to Eq. (1.22). The detailed derivation is described in Ref. (47). As a result,

$$u(x) = \sigma - \frac{\Omega^2}{2\pi i}\lim_{\tau\to 0}\int_{-\infty}^{\infty}\frac{e^{iqx}}{L(q)(q+i\tau)}dq\,, \tag{1.24}$$

where

$$L(q) = \Omega^2 + 4\sin^2\left(\frac{q}{2}\right) - q^2v^2 \tag{1.25}$$

is derived. By using an upper indented half-circle centered at the origin[51], Eq. (1.24) can be rewritten as

$$\begin{aligned} u(x) &= \sigma - \frac{\Omega^2}{2\pi i}\lim_{\tau\to 0}\left[\int_{-\infty}^{\tau}\frac{e^{iqx}}{qL(q)}dq + \int_{-\tau}^{\tau}\frac{e^{iqx}}{qL(q)}dq + \int_{\tau}^{\infty}\frac{e^{iqx}}{qL(q)}dq\right] \\ &= \sigma - \frac{\Omega^2}{2\pi i}\left[\int_{-\infty}^{\infty}\frac{e^{iqx}}{qL(q)}dq - \frac{\pi i}{L(0)}\right] \\ &= \sigma + \frac{1}{2} - \frac{\Omega^2}{2\pi i}\int_{-\infty}^{\infty}\frac{e^{iqx}}{qL(q)}dq. \end{aligned} \tag{1.26}$$

In order to calculate the infinite integral in Eq. (1.26), it is necessary to change it to contour integral with the residue theorem. To do this, we should classify zeros of $L(q)$ depending on

their characteristics. Since a dispersion relation of the system is $\omega(q) = (\Omega^2 + 4\sin^2(q/2))^{1/2}$,

$$L(q) = \omega^2(q) - q^2 v^2 . \tag{1.27}$$

Therefore, the zeros of $L(q)$ correspond to the wavenumbers of lattice waves whose phase velocity is equal to the dislocation velocity. In particular, the *real* zeros of $L(q)$ should be carefully handled because some of them induce the dislocation oscillation even as $x \to \pm\infty$ without decaying. Thus, only the real zeros that do not violate the boundary conditions at infinity should be chosen depending on sign of *x*. This can be done by comparing the group velocity v_g of the lattice waves with the dislocation velocity. As the lattice wave is emitted from the dislocation core, it has

$$v_g \equiv \frac{\partial \omega}{\partial q} = v + \frac{L'(q)}{2qv} . \tag{1.28}$$

According to Eq. (1.28), $v_g > v$ if $qL'(q) > 0$ and $v_g < v$ if $qL'(q) < 0$. For $v_g > v$, wakes caused by the lattice waves emission can exist both in front of and behind the dislocation. On the contrary, the wakes can only exist behind of the dislocation when $v_g < v$. As a result, the displacement is derived as

$$u(x) = \begin{cases} \sigma + 1 + \Omega^2 \sum\limits_{q \in M_-} \dfrac{e^{iqx}}{qL'(q)} - \dfrac{\Omega^2}{2} \sum\limits_{q \in R_-} \dfrac{e^{iqx}}{qL'(q)} & (x < 0), \\ \sigma - \Omega^2 \sum\limits_{q \in M_+} \dfrac{e^{iqx}}{qL'(q)} + \dfrac{\Omega^2}{2} \sum\limits_{q \in R_+} \dfrac{e^{iqx}}{qL'(q)} & (x > 0), \end{cases} \tag{1.29}$$

where

$$\begin{aligned} R_+ &= \{q : L(q) = 0;\ \mathrm{Im}\, q = 0, qL'(q) > 0\}, \\ R_- &= \{q : L(q) = 0;\ \mathrm{Im}\, q = 0, qL'(q) < 0\}, \\ M_+ &= \{q : L(q) = 0; \{\mathrm{Im}\, q > 0\} \cup \{\mathrm{Im}\, q = 0, qL'(q) > 0\}\}, \\ M_- &= \{q : L(q) = 0; \{\mathrm{Im}\, q < 0\} \cup \{\mathrm{Im}\, q = 0, qL'(q) < 0\}\}. \end{aligned} \tag{1.30}$$

After then, if we insert $u(0) = 1/2$ into Eq. (1.26) and (1.29),

$$\sigma = \frac{\Omega^2}{2\pi i} \int_{-\infty}^{\infty} \frac{e^{iqx}}{qL(q)} dq = \Omega^2 \sum_{q \in R_\pm} \frac{1}{|qL'(q)|}, \tag{1.31}$$

is derived. To describe the dislocation motion more realistic, we can also add the viscous loss with

a damping coefficient η into Eq. (1.18). Then, the displacement is derived as[52]

$$u(x)=\begin{cases}\sigma+1+\Omega^2\sum\limits_{q\in I_-}\dfrac{e^{iqx}}{qN'(q)} & (x<0),\\ \sigma-\Omega^2\sum\limits_{q\in I_+}\dfrac{e^{iqx}}{qN'(q)} & (x>0),\end{cases} \tag{1.32}$$

where

$$N(q)=\Omega^2+4\sin^2\left(\frac{q}{2}\right)-q^2v^2-i\eta qv, \tag{1.33}$$

$$\begin{aligned} I_+&=\{q:N(q)=0;\mathrm{Im}q>0\},\\ I_-&=\{q:N(q)=0;\mathrm{Im}q<0\}. \end{aligned} \tag{1.34}$$

Since a damping term in Eq. (1.33) makes $N(q)$ do not have zeros in real axis, the stress is directly derived from Eq. (1.32). As a result, the stress is analytically derived as Eq. (1.35)[52] and it is drawn as a function of dislocation velocity in Fig. 1.5.

$$\sigma=\frac{1}{2}+\Omega^2\sum_{q\in I_+}\frac{1}{qN'(q)} \tag{1.35}$$

According to Eq. (1.31) and (1.35), the stress is an implicit function of dislocation velocity rather than the explicit one. When the radiation drag is a dominant drag mechanism during the dislocation motion, the dislocation velocity characterizes the lattice waves emitted from the dislocation core. Therefore, a drag coefficient caused by the radiation drag is derived as

$$B_{dis}(v)=\frac{\partial\tilde{\sigma}}{\partial\tilde{v}}=B_0\Omega^2\sum_{q\in I_+}\frac{4vq+i\eta}{q(N'(q))^2}, \tag{1.36}$$

where $B_0=bc\sqrt{\rho/E}$.

1.4. Objectives and scope

In this dissertation, various drag mechanisms acting on a gliding dislocations are revealed and equations of dislocation motion are systematically developed depending on the drag sources. Since the discrete nature of dislocation is mainly responsible to the interaction between the dislocation core and phonons, the theoretical model is established based on the DLD theory. In addition, the developed theory is validated by molecular dynamics (MD) simulations under

various conditions.

In Chapter 2, the theoretical phonon scattering model is developed for the simplest case of a dislocation motion, i.e. an ideal dislocation that moves without oscillation. As a result, it is proved that the drag effect caused by the scattering is responsible to the *'stress-drop'* behavior around the dislocation core while it is in motion. And this is supported by the MD simulation.

In Chapter 3, the theoretical model developed in Chapter 2 is extended to general cases, i.e. a moving dislocation accompanying its oscillation. By additionally considering the oscillation induced by drags, the model finally enables to derive the general equation of dislocation motion. The equation of motion is tested for various cases where the dislocation oscillation occurs. All these cases are quantitatively supported by the MD simulation. Furthermore, the physical meaning of the developed equation is extracted with defining dimensionless group parameters.

In Chapter 4, the equation of dislocation model is extended to low-angle grain boundary (LAGB) given that it is an array of dislocations. During the motion of LAGB under loading, not only the stress-drop but additional unusual behaviors that is not explainable by the continuum theory are also observed in the MD simulation. These are discussed in terms of the DLD theory and the equation of LAGB motion developed in this work.

In Chapter 5, the drag force is analytically derived in terms of configurational force when a gliding dislocation interacts with phonons. To reveal the influence of interaction between them, a dislocation-phonon coordinate system is adopted in this study. As a result, the *J*-integral around the moving dislocation where the drag effect is considered is derived and it is proved that the drag force breaks a path-independent behavior of the *J*-integral. Then, the drag force is numerically calculated by controlling the parameters that characterize the dislocation core.

Chapter 2
Phonon Scattering Around an Ideal Dislocation

This chapter is written based on the following articles:

1. **Kim, S.**, Ho, D. T., Kang, K. & Kim S. Y., 2016. Phonon scattering during dislocation motion inducing stress-drop in cubic metals. *Acta. Mater.* **115**, 143-154.
2. **Kim, S.**, Kim, H., Kang, K. & Kim, S. Y., 2020. Relativistic effect inducing drag on fast-moving dislocation in discrete system. *Int. J. Plast. (in press)*
3. **Kim, S.**, Kang, K. & Kim, S. Y. Dynamic drags acting on moving defects in discrete dispersive media: from dislocation to low-angle grain boundary. *(submitted)*

2.1 Overview

In discrete lattice, a dislocation translation from one Peierls valley to the neighboring valley consists of three steps. At first, the dislocation locates at the valley, so system's energy is local minimum. As the external shear stress σ_{app} is applied to the system, the stored energy density increases by $\sigma_{app}^2/2\mu$. However, if σ_{app} exceeds the Peierls stress of dislocation, some of the stored energy converts into heat because an atomic bond inside the dislocation core is broken as described in Fig. 2.1. As a result, the energy density around the dislocation core suddenly drops. Then, it moves to the neighboring local minimum state. Here, the bond-breaking mechanism is manifested by *stress-drop* behavior around the dislocation core during its motion.

Among the theoretical methods to describe dislocation motion, the most widely used one is the discrete lattice dynamics (DLD) model[50,53,54]. This assumes that a system consists of uniformly arrayed atoms, and displacements of the atoms are derived by solving dynamic equations of motion. Based on the model, there have been many efforts to derive dislocation mobility in analytic form[43,55], and it allowed one to quantify drag effects induced by phonon scattering in the dislocation core on its mobility[13,56,57]. The explanations of phonon scattering on dislocations based

on a theoretical approach provide us with profound insights to understand its core.

In this Chapter, both theoretical modeling and computer simulations are carried out. We derive an analytical equation to calculate the magnitude of the stress-drop for the simplest case based on the DLD theory and explain the stress-drop phenomenon observed in MD simulations at 0 K. Then, as we control the temperature and size of the system, we observe changes in the magnitude of the stress-drop and in dislocation speed and prove the validity of the equations obtained above.

2.2 Simulation setup

All of the MD simulations presented in this work were performed using Large-scale Atomic/Molecular Massively Parallel Simulator (LAMMPS)[58].

2.2.1 Edge dislocation in two-dimensional (2D) triangular lattice

To describe interaction between two atoms in the triangular lattice, the Lennard-Jones (LJ) potential was used. Here, the atomic mass *M* is set as 55.82 amu. We used cutoff radius $r_c = 3.726$ Å and $\sigma = 2.267$ Å as LJ parameters defined by Filippova et al[63]. And in order to control stiffness of the material, we varied other LJ parameter ε to have values from $0.5\varepsilon_0$ to $3.0\varepsilon_0$ with $\varepsilon_0 = 0.7064$ eV. The stiffness *K* could be calculated by $K = \partial^2 V/\partial r^2|_{r_m} = 57.146\,\varepsilon/\sigma^2$, where $r_m (= 2^{1/6}\sigma = 2.545$ Å) is an equilibrium interatomic distance. The size of the simulation box used in this study was 101.7 nm × 23.3 nm × 2.5 nm along *x*, *y*, and *z* directions, respectively. In the *z*-direction, the cell has only one atomic layer and periodic boundary condition is applied only in the *x*-direction. Thus, the system becomes a single-layer nanosheet that has a free edge in the *y*-direction and has a degree of freedom, *2N* where *N* is the total number of atoms. After relaxation by the conjugate-gradient energy minimization scheme, a single edge dislocation—whose magnitude of Burgers vector **b** is 2.545Å —is introduced at the center of the system by using a conventional method[28]. The dislocation core in the equilibrium state is described in Fig. 2.2a. After the dislocation was embedded, a constant shear force was applied to atoms in the top and bottom free edges along the *x* direction in opposite directions and the atomic positions were updated every 1 fs using Nosé-Hoover thermostat[61,62] at the desired temperature. As a result, the dislocation moved toward the *x* direction.

2.2.2 Edge dislocation in BCC crystals

To simulate an edge dislocation, the iron, molybdenum are used. Due to a structural similarity between molybdenum and iron, the simulation method was almost same. For the iron, the embedded atomic method (EAM) interatomic potential developed by Mendelev et al.[59] was used to describe the interaction between two atoms. And for the molybdenum, the EAM potential developed by Smirnova et al.[60] was used. For both crystals, the principal axes *x*, *y* and *z* directions were oriented along the $[111], [1\bar{1}0]$ and $[11\bar{2}]$ directions, respectively. The size of simulation box used in this study depended on the purpose of the simulation.

First, in order to see the stress-drop behavior in the iron, the box size was 22.5 nm × 18.0 nm × 1.40 nm unless stated otherwise. Periodic boundary conditions were applied along the *x* and *z* directions, but relaxation was allowed in the *y* direction. After relaxation by the conjugate gradient energy minimization scheme, a single edge dislocation, whose Burgers vector is $\mathbf{b} = 1/2\,[111]$, was embedded along the *z* direction in the iron nanoplate by deleting the lower-half plane and applying displacement fields to the atoms. The applied displacement fields are derived in Ref. 28. The final configuration of the dislocation core is shown in Fig. 2.2b. To examine the size effect, additional cells whose sizes are 44.5 nm × 36.2 nm × 1.40 nm, 66.8 nm × 54.3 nm × 1.40 nm, and 89.0 nm × 72.5 nm × 1.40 nm were also used. Although lengths along the *x* direction were changed, the periodic boundary condition in that direction ensured that the size effect affected only the thickness direction. Second, in order to observe the elastic waves emission in both materials, the larger sizes of box along the *x* and *y* directions were used to minimize wave interference. For the iron, the size of simulation box was 66.6 nm × 24.2 nm × 1.40 nm. And for the molybdenum, the size of simulation box was 73.4 nm × 26.8nm × 1.5 nm. The equilibrium configuration of edge dislocation in the molybdenum is shown in Fig. 2.2c.

After the dislocation is inserted, a constant shear force was applied to every atom in the top and bottom free surfaces along the *x* axis in opposite directions. After the dislocation was embedded, a constant shear force was applied to atoms in the top and bottom free surfaces along the *x* direction in opposite directions and the atomic positions were updated every 1 fs using Nosé-Hoover thermostat[61,62] at the desired temperature. As a result, the dislocation moved toward the *x* direction.

2.2.3 Screw dislocation in iron

An iron was chosen to simulate a screw dislocation, and the same interatomic potential used in edge dislocation was employed. For the screw dislocation, the principal axes *x*, *y* and *z* were oriented along the $[11\bar{2}], [\bar{1}10]$ and $[111]$ directions, respectively. The dimension of the simulation cell was 41.8 nm $\times$ 24.0 nm $\times$ 1.48 nm. The periodic boundary condition was only applied along the *z* direction, and the other directions were allowed to be relaxed. The screw dislocation was embedded in the iron nanowire by applying displacement fields, which are derived in Ref. 28, to atoms, and its line was placed parallel to the *z* direction. After relaxation by the conjugate gradient energy minimization scheme, the final configuration of the dislocation core is shown in Fig. 2.2d. After the dislocation was inserted, a constant shear force were applied to the atoms in the top and bottom (110) surfaces along the *z* direction in opposite directions.

2.2.4 Measurement of dislocation velocity

The dislocation velocity was calculated by tracing its core position with simulation time under constant external stress. First of all, the core was defined as a region which consists of atoms whose centro-symmetry parameter falls between 4 $Å^2$ and 7 $Å^2$ and between 3 $Å^2$ and 6 $Å^2$ for an edge dislocation in the iron and molybdenum, respectively. For a screw dislocation in iron, the core was defined as a region where potential energy falls between -4.127 eV and -3.898 eV. The same method was used to track the edge dislocation core in the 2D triangular lattice. However, since the potential energy of atoms depends on the LJ parameters, the energy range to track the dislocation core in the 2D triangular lattice were different for the stiffness values used in this work.

And the position of the core was defined as an average value of positions of atoms which consist the dislocation core. Then, the dislocation velocity was calculated by measuring the slope of the relation between the distance that the core moves and time. Note that the slope is not constant during initial few picoseconds of simulation because the dislocation is in acceleration. Therefore, the slope must be measured when it keeps constant value, or steady state is reached.

2.3 Stress drop

For an edge dislocation in the 2D triangular lattice, when the externally applied stress σ_{app} was smaller than the Peierls stress σ_P, the dislocation did not move and the average stress around the dislocation core was equal to the applied stress, which is shown in Fig. 2.3a. However, when the applied stress exceeds the Peierls stress, which corresponds to Fig. 2.3b, the dislocation started to move and the average stress around the dislocation core reduced by approximately 10 % and became lower than the σ_{app}. Hereafter, the average stress around the core is defined as *actual stress* , σ_{act} , which is the stress resulting from the stress-drop. The σ_{act} was calculated by averaging stresses of all atoms within a circular region that includes the core at its center. Here, we chose a radius of the circular region approximately as $10b$. The same phenomenon was observed while the edge dislocation is moving in iron as shown in Fig. 2.4a and 2.4b. In this case, σ_{act} reduced by approximately 20 % from σ_{app}.

For a screw dislocation in the iron, when σ_{app} was lower than σ_P, the stress-drop did not occur as shown in Fig 2.5a. However, when σ_{app} was larger than σ_P, the stress-drop behavior was still observed while the dislocation was moving although its magnitude is not as much as in the edge dislocation. This is shown in Fig 2.5b. Note that σ_{act} continuously increases from zero although σ_{app} keeps constant value at top and bottom free surfaces because it takes time for the applied stress to be transmitted to inside of the plate from the surfaces.

2.4. Emission of elastic waves

To find the physical origin of the stress drop observed in section 2.3, the DLD theory was employed in this study. From an atomic point of view, the motion of a dislocation consists of repeated breaking and reforming of atomic bonds in its core as described in Fig. 2.1. As the bonds are broken, the elastic waves are radiated from the dislocation core. This phenomenon can be analyzed by a dispersion relation.

2.4.1 Edge dislocation in (two-dimensional) triangular lattice

For 2D triangular lattice described in Fig. 2.6a, a dispersion relation of phonons is

$$w(q_x, q_y) = 2\sqrt{\frac{K}{M}}\left[\sin^2\frac{q_x b}{2} + \sin^2\frac{(q_x + \sqrt{3}q_y)b}{4} + \sin^2\frac{(q_x - \sqrt{3}q_y)b}{4}\right]^{1/2}, \quad (2.1)$$

where w is an angular frequency of the excited waves, $\mathbf{q}$ is a wave vector, M is atomic mass, and K is a spring constant. The derivation of Eq. (2.1) is described in Appendix A. In Fig. 2.6b, Eq. (2.1) is graphically described as a function of q_x when $q_y = 0$. According to the DLD theory, elastic waves are emitted from the dislocation core during its motion and they satisfy a selection rule $w = \mathbf{q} \cdot \mathbf{v}$, where $\mathbf{v}$ is a dislocation velocity vector[31,47,48]. Mathematically, the selected frequencies are isolated poles of lattice Green's function. As a result, the lattice waves are emitted whenever Eq. (2.1) and $w = q_x v$ are intersected as shown in Fig. 2.6b. According to the figure, the number of intersection points decreases as v increases from 0 and there are 2 intersection points except $q_x = 0$ when $v = 0.138C_t$. When $v > 0.138C_t$, the number of intersections reduces to 1. And since the group velocity of emitted waves $\mathbf{v_g}$ is defined as $\mathbf{v_g} \equiv (v_{gx}, v_{gy}) = (\partial w/\partial q_x, \partial w/\partial q_y)$, the direction of the waves can be also analyzed. When $\partial w/\partial q_x > 0$ (or $\partial w/\partial q_x < 0$), the wave is emitted forward (or backward) to the moving dislocation. These are graphically described in Fig. 2.6c and Fig. 2.6d, respectively. For fixed q_x, the solution has $\pm q_y$ that satisfies $w = \mathbf{q} \cdot \mathbf{v}$. Thus the excited waves exist as a couple and they are symmetric about y-axis. Taken together from Fig. 2.6b to 2.6d, when v is much lower than C_t, the excited waves are emitted in all directions. However, as v increases, the forward emission is gradually disappeared and finally only the backward emitted waves are remained.

By using the MD simulations, the emission of lattice waves from a moving dislocation was observed as shown in Fig. 2.7. When $v = 0.135C_t$ as shown in from Fig. 2.7a to 2.7c, the lattice waves were emitted from both front and back sides of the dislocation core. And when the dislocation's speed increased to $0.135C_t < v < 0.180C_t$ as shown in from Fig. 2.7d to 2.7f, the forward emission receded while the backward emission was still well-observed. Finally, when $v \geq 0.180C_t$, only the backward emission was remained. This is shown in from Fig. 2.7g to 2.7i. Therefore, there is a good agreement between the theory and MD simulation in terms of tendency. However, according to the dispersion theory, the forward emission should not observed when $v > 0.150C_t$ but we observed it until $v \approx 0.180C_t$ through the simulation. This discrepancy may occur due to a difference between Eq. (2.1) and an actual dispersion relation of the LJ

material used in the simulation.

2.4.2 Edge dislocation in (three-dimensional) BCC crystals

In addition to the triangular lattice, we observed the emission of lattice waves in the molybdenum and the iron as shown in Fig. 2.8 and Fig. 2.9, respectively. Although a complex structure of three-dimensional dislocation core makes one be difficult to study an exact phonon dispersion, we can infer that similar results will be obtained for the cubic crystal because its *xy* plane is structurally similar to the triangular lattice. For a moving edge dislocation in the molybdenum, the lattice waves were emitted almost equally to all directions when $v < 0.049C_t$. This is described in Fig. 2.8a. And as the dislocation's speed increased, the number of excited waves decreased and, especially, a gradual annihilation of the forward emission was observed in Fig. 2.8b and Fig.2.8c. As *v* increased more and it became finally beyond $0.246C_t$, the lattice waves were only emitted backwards from the dislocation core and the wave pattern left a cone behind the core.

For an edge dislocation in the iron, the similar tendency that was observed in the molybdenum appeared as the dislocation's speed increased. As the dislocation's speed increased, the number of excited waves decreased. This is described in from Fig. 2.9a to 2.9c. And when *v* was finally beyond $0.450C_t$ as shown in Fig. 2.9d, the emitted waves only existed behind the dislocation core. However, note that the curvature of emitted waves in Fig. 2.9d was reversed because the dislocation's speed was fast enough to overtake the forward emitted waves. For both cubic crystals, the number of excited waves were larger than it for the 2D triangular lattice at same v/C_t. There are two main reasons. First, since the cubic crystal has larger degree of freedom than the triangular lattice, the number of phonon bands increases. And since Peierls barrier is much lower in the cubic crystals than the LJ triangular lattice used in this study, the dislocation in the cubic crystals begins its motion at much lower speed. These two effects lead to the larger number of intersections between the dispersion curve and $w = \mathbf{q} \cdot \mathbf{v}$ for the cubic crystals.

2.5 Theoretical model

The radiated phonons from the moving dislocation core, which was observed in from Fig. 2.7 to 2.9, are scattered owing to the anharmonic strain field around it. This scattering process shifts frequencies of the radiated waves and dissipates energy around the dislocation core supplied by σ_{app}. As a result, the average stress around the moving dislocation decreases to σ_{act}. This is the dominant drag mechanism affecting dislocation motion when thermal fluctuation is ignorable[48,64].

For simplicity, let us first consider a 2D square lattice and assume that the lattice consists of atoms—each with a mass of *M*—connected by springs of stiffness *K*. Our lattice system is graphically described in Fig. 2.10a. Assume that the core moves forward at a constant speed *v* under σ_{app}. During its motion, the phonon scattering occurs around the core, which drags it backward. Thus, the core advances a distance less than expected. This is described in Fig. 2.10b, and 2.10c. This is also observed through the MD simulation of the edge dislocation motion in the triangular lattice as shown in Fig. 2.11. If we define the distance that the core actually advances as x_{act}, the expected distance that the core advances due to σ_{app} as x_{app}, and the receded distance by the scattering due to the anharmonic strain field as x_{bond}, they are mathematically related by Eq. (2.2). Physically, x_{bond} represents a pullback distance because of the energy loss by the phonon scattering.

$$x_{act} = x_{app} - x_{bond},$$

or

$$\frac{x_{act}}{x_{app}} = \frac{\sigma_{act}}{\sigma_{app}} = 1 - \frac{x_{bond}}{x_{app}}. \tag{2.2}$$

We can validate Eq. (2.2) by giving two examples. First, when the core does not move, the atomic bonds in the core are not broken, and thus no waves are emitted. This leads x_{bond} to be 0 and $\sigma_{act} = \sigma_{app}$. On the other hand, when the core moves, the atomic bonds are broken, and the resulting emitted waves are scattered by the anharmonic strain field. Therefore, x_{bond} is positive and σ_{act} becomes smaller than σ_{app}. These results coincide with the stress-drop phenomenon described in from Fig. 2.3 to 2.5.

By using the (retarded) lattice Green's function $G(\mathbf{r} - \mathbf{r_0}, w)$, a relationship between x_{bond} and x_{app} can be obtained. The Green's function is defined by Eq. (2.3) and it is derived in detail

in Appendix B.

$$G(\mathbf{r}-\mathbf{r_0},w)=\frac{b^2}{4\pi^2 M}\int_{1st\,BZ} d\mathbf{k}\,\frac{e^{i\mathbf{k}\cdot\mathbf{r}}}{w^2(\mathbf{k})-w^2\pm i\varepsilon}\quad(\varepsilon\to+0). \tag{2.3}$$

Here, $w(\mathbf{k})=w_0[\sin^2(k_x b/2)+\sin^2(k_x b/2)]^{1/2}$, where $w_0=2(K/M)^{1/2}$ is a dispersion relation of phonons in the 2D square lattice system, and **r** is the position of an atom in the discrete lattice corresponding to (*mb, nb*), where both *m* and *n* are integer multiples of 1/2. The sign of $i\varepsilon$ in Eq. (2.3) is determined to satisfy causality conditions. That is, if $\mathrm{Re}(w)<0$, $+i\varepsilon$ is chosen, but if $\mathrm{Re}(w)>0$, $-i\varepsilon$ is chosen.

The elastic wave emitted by atomic-bond breaking at *t=0* from the dislocation core accompanies elastic force *f(t)* that is described by using a Heaviside step function. By applying a Fourier transformation, the elastic force can be expressed as

$$\begin{aligned} f(t)&=\begin{cases}0 & (t<0)\\ Kx_{app}=\dfrac{1}{4}Mw_0^2x_{app} & (t>0)\end{cases}\\ &=\frac{1}{2\pi}\int_{-\infty}^{\infty}F(w)e^{-iwt}dw=-\frac{Mw_0^2x_{app}}{8\pi i}\int_{-\infty}^{\infty}\frac{e^{-iwt}}{w+i\varepsilon}dw\quad(\varepsilon\to+0), \end{aligned} \tag{2.4}$$

where $F(w)=-Mw_0^2x_{app}/(4i(w+i\varepsilon))$. If we assume that $\mathbf{r_0}=\mathbf{0}$ is the position where the wave is emitted, the displacement of the atom induced by the scattering of the wave is derived as

$$\begin{aligned} u(\mathbf{r},t)&=\frac{1}{2\pi}\int_{-\infty}^{\infty}G(\mathbf{r},w)F(w)e^{-iwt}dw\\ &=-\frac{w_0^2b^2x_{app}}{32\pi^3 i}\int_{1st\,BZ}e^{i\mathbf{k}\cdot\mathbf{r}}d\vec{\mathbf{k}}\int_{-\infty}^{\infty}\frac{e^{-iwt}}{[w^2(\mathbf{k})-w^2\pm i\varepsilon](w+i\varepsilon)}dw. \end{aligned} \tag{2.5}$$

By using residue theorem, Eq. (2.5) is transformed to Eq. (2.6).

$$\begin{aligned} u(\mathbf{r},t)&=\frac{w_0^2b^2x_{app}}{32\pi^3 i}\int_{1st\,BZ}e^{i\mathbf{k}\cdot\mathbf{r}}d\mathbf{k}\left[\oint_{C_1}\frac{e^{-iwt}}{[w-(w(\mathbf{k})+i\varepsilon)][w+(w(\mathbf{k})+i\varepsilon)](w+i\varepsilon)}dw\right.\\ &\qquad\left.+\oint_{C_2}\frac{e^{-iwt}}{[w-(w(\mathbf{k})-i\varepsilon)][w+(w(\mathbf{k})-i\varepsilon)](w+i\varepsilon)}dw\right]\\ &=\frac{w_0^2b^2x_{app}}{32\pi^3 i}\int_{1st\,BZ}e^{i\mathbf{k}\cdot\mathbf{r}}d\mathbf{k}\left[\oint_{C_1}A_1(w)dw+\oint_{C_2}A_2(w)dw\right]\\ &=\frac{w_0^2b^2x_{app}}{32\pi^3 i}\int_{1st\,BZ}e^{i\mathbf{k}\cdot\mathbf{r}}d\mathbf{k}\cdot 2\pi i\left[\operatorname*{Res}_{w=-w(\mathbf{k})-i\varepsilon}A_1(w)+\operatorname*{Res}_{w=-i\varepsilon}A_1(w)+\operatorname*{Res}_{w=w(\mathbf{k})-i\varepsilon}A_2(w)\right], \end{aligned} \tag{2.6}$$

where C_1 and C_2 are contours defined in Fig. 2.12. Then, Eq. (2.6) can be simplified to Eq. (2.7).

$$\begin{aligned} u(\mathbf{r},t) &= \frac{w_0^2 b^2 x_{app}}{16\pi^2} \int_{1st\,BZ} \frac{1-\cos(w(\mathbf{k})t)}{w^2(\mathbf{k})} e^{i\mathbf{k}\cdot\mathbf{r}} d\mathbf{k} \\ &= \frac{w_0^2 b^2 x_{app}}{4\pi^2} \int_0^{\pi/b} \int_0^{\pi/b} \frac{\cos(mk_x b)\cos(nk_y b)}{w^2(k_x,k_y)} [1-\cos(w(k_x,k_y)t)] dk_x dk_y . \end{aligned} \tag{2.7}$$

As shown in Fig. 2.10b, the receded distance of the core caused by phonon scattering is derived as the difference between atoms that are located above and below the slip plane when the core reaches the neighboring Peierls valley, or $t = b/2v$. Therefore,

$$x_{bond} = u\left(\left(\frac{b}{2},\frac{b}{2}\right),\frac{b}{2v}\right) - u\left(\left(\frac{b}{2},-\frac{b}{2}\right),\frac{b}{2v}\right). \tag{2.8}$$

The existence of a dislocation imposes the boundary condition $u\big((mb,-nb),t\big) = -u((mb,nb),t)$. As a result, Eq. (2.8) becomes

$$\begin{aligned} x_{bond} &= 2u\left(\left(\frac{b}{2},\frac{b}{2}\right),\frac{b}{2v}\right) \\ &= \frac{w_0^2 b^2 x_{app}}{2\pi^2} \int_0^{\pi/b} \int_0^{\pi/b} \frac{\cos(k_x b/2)\cos(k_y b/2)}{w^2(k_x,k_y)} \left[1-\cos\left(\frac{w(k_x,k_y)b}{2v}\right)\right] dk_x dk_y \\ &\approx \frac{w_0^2 b^2 x_{app}}{16\pi^2} \frac{1}{v^2}\left(\frac{2}{b}\right)^2 \int_0^{\pi/2} \int_0^{\pi/2} \cos x \cos y\, dx dy = \frac{w_0^2 b^2 x_{app}}{4\pi^2 v^2}. \end{aligned} \tag{2.9}$$

If Eq. (2.9) is inserted into Eq. (2.2), σ_{act} and σ_{app} can be simply related by Eq. (2.10). Therefore, as long as the dislocation is in motion, σ_{act} is always lower than σ_{app} as the MD simulation results from Fig. 2.3 to Fig. 2.5.

$$\sigma_{act} = \left(1-\frac{w_0^2 b^2}{4\pi^2 v^2}\right)\sigma_{app}. \tag{2.10}$$

Furthermore, we can extract physical meaning from Eq. (2.10). The difference between σ_{act} and σ_{app} is caused by the second term on the right-hand side of Eq. (2.10). This term is directly proportional to the square of t_P, where $t_P = b/2v$, which is the time required for the core to arrive at a neighboring Peierls valley. Physically, as the dislocation speed increases, less time is required to reach to the neighboring valley, and thus the system does not have enough time for

scattering to occur. Therefore, σ_{act} converges to σ_{app}.

2.6 Discussion

2.6.1 Thermal effect

In addition to the 0 K case, we also investigated the validity of our theoretical approach for dislocation motion under finite temperature condition. We plotted the relation between σ_{act} and σ_{app} for an edge dislocation in the iron nanoplate with changing temperature, and this is shown in Fig. 2.13a. The simulation results show that σ_{act} approaches σ_{app} as the temperature increases, which means that the magnitude of the stress-drop decreases with increasing temperature. This tendency can be explained by the change in dislocation velocity under temperature control. When the temperature is increased from 0 K to 0.05 K, although the increase rate of the temperature is very small, the velocity of dislocation increases by approximately 50%, as shown in Fig. 2.13b. Based on Eq. (2.10), this magnitude of velocity increase induces a 10% less reduction of the applied stress from the 0 K case. Thus, the temperature dependence of the stress-drop can be also explained by Eq. (2.10).

However, our theoretical model has a limitation in that it can be applied to only very low temperature conditions for an edge dislocation. This is due to extremely low Peierls barrier of the edge dislocation. By atomistic simulation, we observed that the dislocation core oscillates with an amplitude that is much larger than the distance between two neighboring Peierls valley during relaxation, and these kind of vibrations are in violation to the basic assumption used in our theoretical derivation. This is because if the amplitude is too large, x_{bond} becomes larger than x_{app}, which induces a negative effective stress inside of the system, which is physically impossible.

2.6.2 Size effect

We started to investigate the size-dependent behavior of the stress-drop with a simple question: If the size of the system is large so it becomes *a bulk plate* rather than a nanoplate, then is it possible that only the existence of the single dislocation induces the stress-drop and is it observable despite its extremely small presence compared to the size of the plate? To answer this question, we simulated the motion of edge dislocation in an iron nanoplate at 0 K by changing its

thickness. Fig. 2.14a shows that the magnitude of the stress-drop decreases as the thickness increases. Not only the change is in the stress-drop, but dislocation speed also increases with increasing thickness, which is shown in Fig. 2.14b. This tendency between the dislocation speed and thickness of the plate is identical to previous simulation study[65]. Therefore, our model proves that the stress-drop behavior is conspicuous on a nanoscale due to the low dislocation speed in this scale; however, as the thickness of the nanoplate increases, it is harder to observe the stress-drop due to the increase in the dislocation speed. Finally, in the bulk plate, we can conclude that although the presence of a single dislocation induces the stress-drop, its effect is negligible.

2.7 Summary

We developed a theoretical model for phonon scattering during dislocation motion based on the DLD theory, and the model is underpinned by the stress-drop behavior observed through atomistic simulations of the dislocation motion. Our model suggests that the phonon scattering in the dislocation core results in dropping of the applied stress around the dislocation core. While the dislocation is gliding in the discrete system, the scattering of an elastic wave generated by breaking the bond between two atoms in the core induces the stress-drop. The stress-drop can be predicted by Eq. (2.10) that was derived from our model. In addition to the 0 K case, the MD simulations at finite temperature could be explained using the dependence of dislocation speed on the temperature. As temperature increases, the magnitude of the stress-drop decreases and converges to zero when the temperature is higher than 0.2 K. The application scope of our model to explain the thermal dependence of the stress-drop, however, is confined to a very small temperature range due to an extremely small Peierls barrier of the edge dislocation. Finally, our model proved that the stress-drop is a mechanical behavior that is prominent on the nanoscale due to the low dislocation speed at that scale.

Chapter 3
Dynamic Drag on General Dislocations

This chapter is written based on the following articles:

1. **Kim, S.**, Kim, H., Kang, K. & Kim, S. Y., 2020. Relativistic effect inducing drag on fast-moving dislocation in discrete system. *Int. J. Plast. (in press)*
2. **Kim, S.**, Kang, K. & Kim, S. Y. Dynamic drags acting on moving defects in discrete dispersive media: from dislocation to low-angle grain boundary. *(submitted)*

3.1 Overview

In Chapter 2, we explained the stress-drop behavior in terms of the scattering of the waves emitted by repetitive atomic bond-breakings while the dislocation glides over the Peierls potential. However, the derived model is confined to describe the ideal dislocation that rarely exists. This is because in practice the dislocation line does not move rigidly but moves with oscillation in the field of waves. Therefore, it must be required to consider the dislocation oscillation to fully describe the dislocation motion.

In general, the oscillation occurs when the dislocation motion is disturbed by the external sources. For example, when the dislocation glides over the forest of other defects (such as point defects or other dislocations) under applied load, they disturb the dislocation motion. According to Koehler[66] and Granato and Lücke[67], they assumed the dislocation line as an elastic string and develop a partial differential equation that the external force is balanced by inertial force, viscous damping force, and line tension of the string. This approach could explain that the dislocation prominently contributes to the internal friction of metals. Their theory has been further developed by successive studies[68,69], and it was proved that the magnitude of drag depends on the frequency of the applied load. As another example, the dislocation can oscillate by the incidence of thermal phonons. The oscillation scatters the phonons and this gives thermal resistivity of a crystal[13].

Further, it decelerates the dislocation velocity[40].

Not only by the external sources, but the dislocation also *spontaneously* oscillates and its inducing drag on the dislocation motion becomes larger as the external stress increases. This type of drag is called *relativistic drag*[70]. As a result, the dislocation mobility is not a constant but decreases as the dislocation velocity increases.

In this chapter, we extend the theoretical phonon scattering model developed in the previous chapter to apply to general dislocations that move with accompanying oscillation. Although the drag sources depend on the dislocation types and external conditions, the resulting behaviors are in concordance with the dislocation oscillation. This implies that the equation of dislocation motion can be generalized.

3.2 Simulation setup

3.2.1 Edge dislocation in 2D triangular lattice

The simulation setup is identical to one used in Chapter 2.In summary, we used same LJ potential introduced in section 2.2.2 to calculate the interaction between atoms. And we control the bond stiffness by changing ε from $0.5\varepsilon_0$ to $3.0\varepsilon_0$ with $\varepsilon_0 = 0.7064$ eV. As a result, a single edge dislocation—whose magnitude of Burgers vector $\mathbf{b}$ is 2.545Å —is introduced at the center of the system. And the dislocation core in the equilibrium state is described in Fig. 2.2a. After the dislocation is inserted, we applied constant shear stress by using the same method introduced in section 2.2.1.

3.2.2 Edge dislocation in BCC crystals

Iron and molybdenum were chosen as media to describe the motion of a single perfect dislocation. For iron, the embedded atomic method (EAM) interatomic potential developed by Mendelev et al.[59] was used to calculate interactions between atoms. For molybdenum, the EAM potential developed by Smirnova et al.[60] was used. For both cases, the principal axes *x*, *y*, and *z* were oriented along $[111], [1\bar{1}0]$ and $[11\bar{2}]$ respectively. The dimensions of the simulation cells were 22.3 nm × 18.0 nm × 1.40 nm and 24.7 nm × 19.7 nm × 1.55 nm for iron and molybdenum, respectively. For both materials, we allowed the *y* direction to be relaxed, whereas periodic conditions were applied along both the *x* and *z* directions, making the systems nanoplate.

The potential energy of the system was minimized using the conjugate gradient method. Then, a single edge dislocation with its line along the *z* axis was inserted by deleting the lower-half plane and applying displacement fields derived by linear elasticity theory[28] to every atom. The corresponding Burgers vector was $\mathbf{b} = 1/2\,[111]$. Then, we minimized the energy of the system again to determine the equilibrium dislocation structure. The equilibrium core structures of the edge dislocations in both materials are described in Fig. 2.2b and 2.2c. Next, we generated an ensemble of velocities following a Gaussian distribution to produce the desired temperature. We equilibrated the system at the desired temperature using the Nosé–Hoover thermostat[61,62] for 200 ps. After then, a constant shear force is applied by using a method described in section 2.2.1.

3.2.3 Extended edge dislocation in FCC crystals

In FCC crystals, a perfect dislocation dissociates into two partial dislocations to lower the system energy[28]. In this work, we chose aluminum, copper, nickel, and gold as media to insert partial dislocations. The EAM interatomic potentials developed by Mishin et al.[87,88], Angelo et al.[89], and Ackland et al.[90] were used to calculate atomic interactions for aluminum, copper, nickel, and gold, respectively. For all materials, the *x*, *y*, and *z* directions were oriented along $[\bar{1}10]$, $[111]$, and $[11\bar{2}]$ respectively. The dimensions of the simulation cells were 25.8 nm × 20.8 nm × 1.49 nm, 23.0 nm × 18.6 nm × 1.33 nm, 22.4 nm × 18.1 nm × 1.29 nm, and 26.0 nm × 20.9 nm × 1.50 nm for aluminum, copper, nickel, and gold, respectively. For all cases, periodic boundary conditions were applied along the *x* and *z* directions, and relaxation was allowed in the *y* direction, making the systems nanoplates. The potential energy of the systems was minimized using the conjugate gradient method. Then, a single edge dislocation with its line along the *z* axis was inserted by deleting the lower-half plane and applying displacement fields derived by linear elasticity theory[28] to every atom. The corresponding Burgers vector was $\mathbf{b} = 1/2\,[\bar{1}10]$. During relaxation, in contrast to the BCC case, the dislocation was divided into two partial dislocations with Burgers vectors of $\mathbf{b_1} = 1/6\,[\bar{2}11]$ and $\mathbf{b_2} = 1/6\,[\bar{1}2\bar{1}]$ and a stacking fault between them. The equilibrium core structures for the FCC crystals are described in Fig. 3.1. Next, we generated an ensemble of velocities following a Gaussian distribution to produce the desired temperature. We equilibrated the system at the desired temperature using the Nosé–Hoover thermostat[61,62] for 200 ps. After then, a constant shear force is applied by using a method described in section 2.2.1.

3.3 Relativistic effect

Although the dissipation processes, caused by the oscillation of dislocation controlled by external conditions, have been widely studied, research is lacking on the relativistic effect. This is because it is difficult to extract its exclusive influence on the dislocation motion when it is mixed with other dissipation effects, which dominate the dynamics of the dislocation in the conventional velocity regime. However, as the dislocation speed *v* approaches the transverse shear wave speed C_t, the relativistic effect becomes significant. The relativistic effect is manifested by a *spontaneous* oscillation of dislocation without excitations in a lattice system. And this effect decreases the increasing rate of steady state velocity of dislocation, or mobility, as stress increases and finally makes the dislocation speed approach to the speed that is much lower than C_t. This is called *level-off* behavior and has been observed through atomistic simulations in previous studies[65,71,72] .

With an allowance of energy dissipation in the system, the Euler-Lagrangian equation for a moving dislocation follows[70,73]

$$\frac{d}{dt}\frac{\partial L}{\partial v}-\frac{\partial L}{\partial x}=-\frac{\partial \theta_D}{\partial v}, \tag{3.1}$$

where *x* is a position of dislocation and θ_D is a dissipative function. Based on continuum theory, Krasnikov and Mayer[70] derived the Lagrangian of a moving edge dislocation *L* in elastic stress field with considering the relativistic effect. This is shown in Eq. (3.2).

$$L=m_0C_t^2\left(1-\sqrt{1-(v/C_t)^2}\right)-U_\sigma . \tag{3.2}$$

Here, $m_0=(\rho b^2/(4\pi(1-\upsilon))\ln(\alpha R/b)$—where ρ and υ are density and Poisson's ratio of the system and *R* is a characteristic length of the dislocation and b/α is the size of dislocation core—is an effective mass of the edge dislocation. And U_σ is a potential energy caused by the elastic stress field and it causes a configuration force $F(=-\partial U_\sigma/\partial x)$ to the dislocation. Since an increase in potential energy due to the relativistic effect is converted into kinetic energy E_K, it follows

$$E_K=m_0C_t^2\left(\frac{1}{\sqrt{1-(v/C_t)^2}}-1\right), \tag{3.3}$$

and causes drag through the oscillation of dislocation. The relativistic effect makes a dissipative

function follow

$$\theta_{D,R} = E_K / t_c , \tag{3.4}$$

where t_c is characteristic time period of the oscillation[73]. In addition to energy dissipation caused by the relativistic effect, Peierls barrier also disturbs the dislocation's motion and corresponding dissipative function $\theta_{D,P}$ satisfies

$$\theta_{D,P} = b\sigma_{th}|v| , \tag{3.5}$$

where σ_{th} is a threshold stress to move the dislocation. And total dissipative function θ_D can be obtained by $\theta_D = \theta_{D,R} + \theta_{D,P}$. By inserting Eq. (3.2) ~ (3.5) to Eq. (3.1), following equation is derived based on continuum theory[70].

$$\frac{m_0}{\left(1-(v/C_t)^2\right)^{3/2}}\frac{dv}{dt} = F - b\sigma_{th}sign(v) - \frac{B_0 v}{\left(1-(v/C_t)^2\right)^{3/2}} , \tag{3.6}$$

where $B_0 = m_0/t_c$.

To date, the relativistic effect has been simply regarded as a result of using alternative mobility law to avoid solving the nonlinear differential equation[74] and the alternative law has been widely applied to DD simulations under shock loading[75,76]. According to Eq. (3.6), the speed of dislocation theoretically diverges at C_t and thus it cannot overcome the sound barrier. There was another approach to derive a drag coefficient at high velocity as a function of the velocity based on phonon wind mechanism[42]. According to Blaschke[77], the drag coefficient quadratically depends on the dislocation displacement gradient derived by the continuum method. As a result, singularities of the drag coefficient were inherited from the poles of the displacement gradient. However, a lot of studies with using MD simulations have shown that the dislocation's speed in cubic crystals and alloys is reachable above C_t[33,34,78]. This deviation is attributed to limitations of continuum theory, where the small-strain assumption is used and dislocation core structure is rarely considered[79,80]. Thus, an approach solely based on the continuum theory is not preferred to study the fast-moving dislocation.

On the other hand, the DLD theory can consider a discreteness nature of the dislocation core. According to the previous studies using the DLD method[47,50,53], it has been proved that the dislocation can overcome the sound barrier so supersonic motion is allowable. In addition, an existence of resonance speed far below C_t was derived when the group and phase velocities of

the wave emitted from the dislocation core are equal to the dislocation speed[38,47]. Especially, Kim et al.[48] and Verschueren et al.[38] recently proved that the atomistic simulations and the DLD theory could be connected to explain a motion of dislocation within subsonic regime. Therefore, the DLD theory can overcome the weaknesses of continuum approach and enable us to seek physical implications of the relativistic effect.

3.4 A general equation of dislocation motion

In previous section, we introduced that the dislocation glides with accompanying oscillation (whether it is forced or spontaneous) in general. Especially, since the spontaneous oscillation caused by the relativistic effect always exists, the dislocation oscillations exist not as separated, single units but instead as multiple sources coexisting. Here, we generalize the theoretical model derived in Chapter 2 by considering an additional scattering caused by the dislocation oscillation.

3.4.1 Theoretical derivation

Although the sources of oscillations are different, they have the same effect of dissipating energy from the core to its surroundings and causing drag effect on the motion of the dislocation. Therefore, in this work, we simply describe a displacement of the oscillating core atom with frequency Ω as $x(t) = x_{app}\sin(\Omega t)$. If the oscillation effect is considered in addition to the breaking of atomics bonds, Eq. (2.2) becomes Eq. (3.7).

$$x_{act} = x_{app} - x_{bond} - x_{osc},$$

or

$$\frac{x_{act}}{x_{app}} = \frac{\sigma_{act}}{\sigma_{app}} = 1 - \frac{x_{bond}}{x_{app}} - \frac{x_{osc}}{x_{app}}. \tag{3.7}$$

To relate x_{osc} and x_{app}, the force originating from the oscillation f_{osc} is first described. Since our goal is to simply capture the effect of the oscillation rather than its cause, we use the relationship $f_{osc} = D\dot{x}(t)$, where D is the drag coefficient of the oscillation. Via a Fourier transform, f_{osc} can be alternatively described by Eq. (3.8).

$$\begin{aligned} f_{osc}(t) &= \frac{1}{2\pi}\int_{-\infty}^{\infty} F_{osc}(w)e^{-iwt}dw \\ &= \frac{D\Omega x_{app}}{2}\int_{-\infty}^{\infty}\left[\delta(-w-\Omega)+\delta(-w+\Omega)\right]e^{-iwt}dw\,, \end{aligned} \tag{3.8}$$

where $F_{osc}(w) = \pi D\Omega_{osc}x_{app}[\delta(-w-\Omega)+\delta(-w+\Omega)]$.

As the dislocation oscillates, elastic waves are emitted and they are scattered around the dislocation core by anharmonic strain field. The scattered displacement of the core atom induced by the oscillation, $u_{osc}(\mathbf{r},t)$, can be derived as

$$\begin{aligned} u_{osc}(\mathbf{r},t) &= \frac{1}{2\pi}\int_{-\infty}^{\infty} G(\mathbf{r},w)F_{osc}(w)e^{-iwt}dw \\ &= \frac{D\Omega b^2 x_{app}}{8\pi^2 M}\int_{1st\,BZ} e^{i\mathbf{k}\cdot\mathbf{r}}d\vec{\mathbf{k}}\int_{-\infty}^{\infty}\frac{\delta(-w-\Omega)+\delta(-w-\Omega)}{w^2(\mathbf{k})-w^2}e^{-iwt}dw. \end{aligned} \tag{3.9}$$

Eq. (3.9) can be simplified to Eq. (3.10) as

$$u_{osc}(\mathbf{r},t) = \frac{Dx_{app}}{\pi^2 M\Omega}\Phi(\mathbf{r})\cos(\Omega t)\,, \tag{3.10}$$

where

$$\Phi(\mathbf{r}) = \int_0^{\pi}\int_0^{\pi}\frac{\cos(mx)\cos(ny)}{\frac{w^2(x,y)}{\Omega^2}-1}dxdy\,. \tag{3.11}$$

The receded distance of the core caused by the oscillation x_{osc} can now be derived as Eq. (3.12). Here, we assume that the core speed is much higher than that of the oscillation given that the externally applied stress is larger than the drag force.

$$\begin{aligned} x_{osc} &= u_{osc}\left(\left(\frac{b}{2},\frac{b}{2}\right),\frac{b}{2v}\right) - u_{osc}\left(\left(\frac{b}{2},-\frac{b}{2}\right),\frac{b}{2v}\right) \\ &= 2u_{osc}\left(\left(\frac{b}{2},\frac{b}{2}\right),\frac{b}{2v}\right) \\ &= \frac{2D\Phi_{dis}x_{app}}{\pi^2 M\Omega}\cos\left(\frac{\Omega b}{2v}\right) \approx \frac{2D\Phi_{dis}x_{app}}{\pi^2 M\Omega}\left(1-\frac{\Omega^2 b^2}{8v^2}\right). \end{aligned} \tag{3.12}$$

In Eq. (3.12), Φ_{dis} is defined as

$$\Phi_{dis} \equiv \int_0^{\pi}\int_0^{\pi} \frac{\cos\left(\frac{x}{2}\right)\cos\left(\frac{y}{2}\right)}{\left(\frac{w_0}{\Omega}\right)^2\left(\sin^2\left(\frac{x}{2}\right)+\sin^2\left(\frac{y}{2}\right)\right)-1}\,dxdy\,. \tag{3.13}$$

By inserting Eq. (2.9) and (3.12) into Eq. (3.7), σ_{act} and σ_{drag} can be simply related by Eq. (3.14).

$$\sigma_{act} = \left(1 - C_1^{dis} + \frac{w_0^2 b^2}{4\pi^2 v^2}(C_2^{dis} - 1)\right)\sigma_{app}\,. \tag{3.14}$$

Here, C_1^{dis} and C_2^{dis} are dimensionless parameters that are defined as

$$\begin{aligned} C_1^{dis} &= \frac{2D\Phi_{dis}}{\pi^2 M\Omega}\,, \\ C_2^{dis} &= \frac{D\Phi_{dis}\Omega}{Mw_0^2}\,. \end{aligned} \tag{3.15}$$

If we insert Eq. (3.14) into the relationship $v = M_{dis}\sigma_{act}$, Eq. (3.16) is derived as

$$v^3 - M_{dis}\sigma_{app}(1 - C_1^{dis})v^2 - M_{dis}\sigma_{app}\frac{w_0^2 b^2}{4\pi^2}(C_2^{dis} - 1) = 0\,. \tag{3.16}$$

3.4.2 Physical meanings of the theoretical model

We proved that oscillating dislocations generally follow Eq. (3.16) although the exact values of C_1^{dis} and C_2^{dis} depend on the source of oscillations. In this section, we discuss the significance of both parameters to understand the drag effect acting on gliding dislocations. To determine C_1^{dis} and C_2^{dis} from Eq. (3.15), it is required to first calculate Φ_{dis}. Thus, we begin our discussion by extracting the physical meaning of Φ_{dis} through the lattice dynamics analysis.

Here, we adopt a method suggested by Lifshitz and Kosevich[81] in which we assume that the dislocation core is an isolated perturbation[82,83]. In general, a system including this perturbation follows Eq. (3.17).

$$\frac{\partial^2 \mathbf{u}}{\partial t^2} + \mathbf{L}\mathbf{u} + \mathbf{\Lambda}(\mathbf{r_p})\mathbf{u} = \mathbf{0}\,, \tag{3.17}$$

where **L** is a diagonal operator that represents the square of the frequency band of the system,

$\mathbf{\Lambda}(\mathbf{r_p})$ is a local perturbation matrix, and $\mathbf{r_p}$ is the position of the perturbation. Here, we assume that $\mathbf{\Lambda}(\mathbf{r_p})$ only affects the immediate neighbors of the perturbation point. Under the plane wave assumption, we insert $\mathbf{u}(\mathbf{r},\mathrm{t}) = \mathbf{x}(\mathbf{r})\exp(i\Omega t)$ into Eq. (3.17). If we define $f(\mathbf{r})$ to be decreasing rate of the local perturbation away from its center, Eq. (28) can be derived[81].

$$\Omega^2 x(\mathbf{r}) - \sum_{\mathbf{r'}} L(\mathbf{r}-\mathbf{r'})x(\mathbf{r'}) = \Lambda(\Omega^2) f(\mathbf{r}) \sum_{r'} f(\mathbf{r'})x(\mathbf{r'}) . \tag{3.18}$$

Here, we assume that $\mathbf{r_p} = \mathbf{0}$ and $f(\mathbf{r})$ should satisfy the normalization condition $\sum_{\mathbf{r}} f(\mathbf{r}) = 1$. To solve Eq. (3.18), we use the Green's function method. The Green' function is determined by the following equation.

$$\sum_{\mathbf{r'}} L(\mathbf{r}-\mathbf{r'})G(\Omega;\mathbf{r'}) - \Omega^2 G(\Omega;\mathbf{r}) = \delta(\mathbf{r}) , \tag{3.19}$$

where $\delta(\mathbf{r})$ is a Dirac delta function. Applying a Fourier transform to both sides of Eq. (3.19) yields

$$G(\Omega;r) = \sum_{\mathbf{k}} G(\Omega;\mathbf{k}) e^{i\mathbf{k}\cdot\mathbf{r}} = \sum_{\mathbf{k}} \frac{1}{w_0^2(\mathbf{k}) - \Omega^2} e^{i\mathbf{k}\cdot\mathbf{r}} , \tag{3.20}$$

where $w_0^2(\mathbf{k}) = \sum_{\mathbf{r}} L(\mathbf{r}) e^{-i\mathbf{k}\cdot\mathbf{r}}$. Now, we apply a Fourier transform to both sides of Eq. (3.18) to give

$$\{w_0^2(\mathbf{k}) - \Omega^2\} x_{\mathbf{k}} = -\Lambda(\Omega^2) \sum_{\mathbf{r}} \sum_{\mathbf{r'}} f(\mathbf{r}) f(\mathbf{r'}) x(\mathbf{r'}) e^{-i\mathbf{k}\cdot\mathbf{r}} . \tag{3.21}$$

Eq. (3.21) can be transformed into

$$\begin{aligned} x(\mathbf{r}) &= -\Lambda(\Omega^2) \left[\sum_{\mathbf{r'}} f(\mathbf{r'}) \right] \left[\sum_{\mathbf{k}} G(\Omega;\mathbf{k}) e^{i\mathbf{k}\cdot(\mathbf{r}-\mathbf{r'})} \right] \left[\sum_{\mathbf{r_0}} f(\mathbf{r_0}) x(\mathbf{r_0}) \right], \\ &= -\Lambda(\Omega^2) \sum_{\mathbf{r'}} G(\Omega;\mathbf{r}-\mathbf{r'}) f(\mathbf{r'}) \tilde{x} \end{aligned} \tag{3.22}$$

where $\tilde{x} = \sum_{\mathbf{r}} f(\mathbf{r}) x(\mathbf{r})$. We multiply both sides of Eq. (3.22) by $\sum_{\mathbf{r}} f(\mathbf{r})$ to give

$$1 + \Lambda(\Omega^2) \sum_{\mathbf{k}} \frac{|a(\mathbf{k})|^2}{w_0^2(\mathbf{k}) - \Omega^2} = 0 , \tag{3.23}$$

where $a(\mathbf{k}) = \sum_{\mathbf{r}} f(\mathbf{r}) e^{-i\mathbf{k}\cdot\mathbf{r}}$. If we define $D(\Omega^2)$ as

$$D(\Omega^2) \equiv \sum_{\mathbf{k}} \frac{|a(\mathbf{k})|^2}{w_0^2(\mathbf{k}) - \Omega^2} = \frac{1}{(2\pi)^2} \int \frac{|a(\mathbf{k})|^2}{w_0^2(\mathbf{k}) - \Omega^2} d\mathbf{k}\,, \tag{3.24}$$

then Eq. (3.23) can be rewritten as $\Lambda(\Omega^2)D(\Omega^2) = -1$. As a result, this relationship determines the permissible vibrational frequencies near the local perturbation[81]. From Eq. (3.24), when $|a(\mathbf{k})|^2 = cos(k_x b)\, cos(k_y b)$, $D(\Omega^2)$ and Φ_{dis} can be related by

$$\Phi_{dis} = (2\pi\Omega)^2 D(\Omega^2)\,. \tag{3.25}$$

Since $|a(\mathbf{k})|^2$ is proportional to the decreasing rate of the perturbation, Φ_{dis} quantifies the localization of local vibrations around the dislocation frequency, Ω, in reciprocal space. Now, we extract the physical meaning of Φ_{dis} in *real* space through a further mathematical process. Since $\Lambda(\Omega^2) = -(2\pi\Omega)^2/\Phi_{dis}$, Eq. (3.22) becomes

$$x(\mathbf{r}) = \frac{(2\pi\Omega)^2}{\Phi_{dis}} \tilde{x} \sum_{\mathbf{k}} \frac{a(\mathbf{k}) e^{i\mathbf{k}\cdot\mathbf{r}}}{w_0^2(\mathbf{k}) - \Omega^2}\,. \tag{3.26}$$

At a large distance from the perturbation source, $a(\mathbf{k}) \approx 1$ because $f(\mathbf{r}) \approx \delta(\mathbf{r})$, and thus small wavenumbers become important. For small wavenumbers, it can be assumed that $w_0^2(\mathbf{k}) \approx w_{0,\min}^2 + \beta^2 k^2$ for an isotropic model where β^2 is a constant with a magnitude on the order of $(w_{0,\max}^2 - w_{0,\min}^2)$. Therefore, at a large distance from the defect,

$$\begin{aligned} \frac{x(\mathbf{r})}{\tilde{x}} &= \frac{\Omega^2}{\Phi_{dis}} \int \frac{e^{i\mathbf{k}\cdot\mathbf{r}}}{w_0^2(\mathbf{k}) - \Omega^2} d\mathbf{k} \\ &\approx \frac{\Omega^2}{\beta^2 \Phi_{dis}} \int \frac{e^{i\mathbf{k}\cdot\mathbf{r}}}{k^2 + (w_{0,\min}^2 - \Omega^2)/\beta^2} d\mathbf{k} = \frac{\pi l \Omega^2}{\beta^2 \Phi_{dis}} e^{-r/l}\,, \end{aligned} \tag{3.27}$$

where $l = \sqrt{\beta^2/(w_{0,min}^2 - \Omega^2)}$. According to Eq. (3.27), $x(r)$ decreases as Φ_{dis} increases. In other words, as the frequencies become more localized around the frequency of dislocation, the atomic amplitude far from the dislocation core decreases. This implies that Φ_{dis} also represents the *structural compactness* of the dislocation core in real space. As a result, a large Φ_{dis} of the dislocation core indicates a condensed structure, whereas a small Φ_{dis} indicates a widely extended core.

From the meaning of Φ_{dis}, we can investigate the influence of group parameters C_1^{dis} and C_2^{dis} on the dislocation motion. According to Eqs. (3.7) and (3.14), the magnitude of the

oscillation drag force relative to the externally applied force can be simply determined by C_1^{dis} and C_2^{dis} as shown in Eq. (3.28).

$$\frac{F_{osc}}{F_{app}} = \frac{x_{osc}}{x_{app}} = C_1^{dis} - \left(\frac{w_0 b}{2\pi v}\right)^2 C_2^{dis}. \tag{3.28}$$

Since both C_1^{dis} and C_2^{dis} are proportional to Φ_{dis} per Eq. (3.15), it is expected that a more compact core structure will lead to an increased oscillation drag force. This may lead to the fact that a compact dislocation requires a higher Peierls stress and is less mobile than an extended dislocation under the same external conditions if other conditions are the same[84,85]. According to Eq. (3.28), the oscillation drag force increases as C_1^{dis} increases and C_2^{dis} decreases. As a result, the parameters have opposite influences on the drag effect. From Eq. (3.15), C_1^{dis} solely depends on the oscillation frequency of the dislocation core, whereas C_2^{dis} heavily depends on that of the atoms in the perfect system rather than that of the core. This relationship implies that the dislocation core directly causes drag to its motion, which manifests as C_1^{dis}, but the remainder of the system aside from the core region tries to resist the drag, which is represented by positive C_2^{dis}. Interestingly, we observed that increasing C_1^{dis} not only leads to decreasing dislocation speed but also increases the nonlinearity of the relationship between speed and applied stress. This is shown in Fig. 3.2. Given that it has been reported that the nonlinear behavior of defect speed is closely related to the energy dispersion of the moving defect[27], our work draws a cogent conclusion.

3.5 Applications

In this section, we solve Eq. (3.16) derived in the preceding section to obtain the speeds of dislocations. To solve this, the two group parameters C_1^{dis} and C_2^{dis} should first be calculated. However, it is difficult to calculate all the parameters required to obtain both group parameters for 3D crystals in particular since the dislocation core structures are complex and the lattice structure is not as simple as we assumed in modeling. Instead, we avoid this difficulty by directly obtaining both group parameters without calculating their component parameters by fitting the results of molecular dynamics simulations.

3.5.1 Edge dislocation in 2D triangular lattice at 0 K

In the 2D triangular lattice with LJ potential used in this study, the dislocation moves as a straight line without dissociation. In this case, the spontaneous oscillation of the dislocation core caused by the relativistic effect dissipates the core energy during its translation in addition to the scattering of radiated phonons from the core. As the dislocation velocity increases, the kinetic energy of dislocation increases and the increasing energy is converted into heat through the spontaneous oscillation of the core[70]. As a result, the dislocation speed gradually approaches the transverse shear wave speed, and the oscillation effect becomes more significant. Based on this oscillation mechanism, we solve Eq. (3.16) by inserting the material properties.

Compared to the 3D crystals, C_1^{dis} and C_2^{dis} can be more analytically calculated for the 2D lattice because of its simple dislocation structure. For an oscillating dislocation, its frequency Ω is larger than w_0 in general because the atoms around the dislocation core more easily oscillate than the atoms in the perfect region. However, since the dislocation core region consists of same atoms as in perfect region and is only a small perturbation whose width is within few atomic diameters, we may assume that a difference between Ω and w_0 is not large so that they have the same order. More specifically, we can relate both frequencies through a simple scheme described in Fig. 3.3. Initially, the system has no defect (Fig. 3.3a). This state is defined as A_0. To nucleate the dislocation core, however, external energy is supplied to the system so that it breaks the atomic bonds in the region of dislocation core. As a result, a new subsystem, A_Ω, is generated. This is described in Fig. 3.3b. If we assume that subsystems in Fig. 3.3b are ideally isolated, Eq. (3.29) should be satisfied between the initial and final states.

$$\frac{1}{2}NMw_0^2x_0^2 + N_\Omega E_c \approx \frac{1}{2}N_\Omega M\Omega^2 x_\Omega^2 + \frac{1}{2}(N - N_\Omega)Mw_0^2x_0^2 \tag{3.29}$$

where N is the total number of atomic bonds, N_Ω is the number of broken atomic bonds, E_c is a cohesive energy, and x_0 and x_Ω are vibration amplitudes of perfect and core regions, respectively. Here, we assume that $x_\Omega \approx x_0$. Therefore, the frequency of dislocation core approximately becomes

$$\Omega \approx \sqrt{w_0^2 + \frac{2E_c}{Mx_0^2}}\,. \tag{3.30}$$

By measuring a shear modulus μ and a density of the system ρ, we calculated a transverse shear wave speed C_t based on the fact that $C_t = \sqrt{\mu/\rho}$. As we transformed a force-displacement

equation, $F = Ku_x$, to a stress-strain equation, $\sigma = 2\mu\varepsilon_{xy}$ by $F/(L_xL_z) = K(L_y/(L_xL_z))(u_x/L_y)$, we could derive $\mu = K(L_y/(2L_xL_z)$ where L_x, L_y and L_z are box sizes along *x*, *y*, and *z* directions, respectively. And a density was simply derived from its definition by $\rho = NM/(L_xL_yL_z)$. As a result, we obtained that C_t is equal to $(L_y/\sqrt{2})\sqrt{K/NM}$. The sound wave velocity of each ε value is calculated in Table 3.1. And the speeds of edge dislocation were measured with changing external stress under different stiffness values.

To apply our theoretical model to the simulation results, we calculated parameters to solve Eq. (3.16). First, we obtained M_{dis} by measuring a slope, $dv/d\sigma_{app}$, at very low stress regime where the dislocation began to move so that the relativistic effect was negligible. Then, we calculated a natural frequency of the perfect atom by $w_0 = 2\sqrt{K/M}$ and of the core by Eq. (3.30). For the core, we additionally calculated E_c and x_0 for each ε. We observed that E_c was directly proportional to ε but x_0 did not depend on ε, atomic positions, and external stress. As a result, x_0 was around 0.1 Å. Compared to $|\mathbf{b}|$, the relative ratio of oscillation amplitude was around 4 %. As a result, we obtained $\Omega \approx 3.7w_0$ and $\Phi_{dis} = 4.21$. Then we calculated $B = \eta B_c = 2\eta\sqrt{KM}$ by assuming the system as a harmonic oscillator. Here, η is a damping ratio used as a fitting parameter to describe the simulation results well. From these parameters, C_1^{dis} and C_2^{dis} were calculated. All the input parameters are summarized in Table 3.1. After the inserting these values into Eq. (3.16), we obtained solutions, which are dislocation speeds. Furthermore, we computed the solution of Eq. (3.6), which was derived by the continuum theory. According to Krasnikov and Mayer[70], a terminal speed of dislocation, which is the solution of Eq. (3.6) when $t \to \infty$, can be analytically derived as

$$v_\infty = \frac{C_t\varsigma}{6\sqrt{6}}\left(\frac{\left(108\varsigma + 12\sqrt{3}\sqrt{4+27\varsigma}\right)^{2/3} - 12}{\varsigma\left(108\varsigma + 12\sqrt{3}\sqrt{4+27\varsigma}\right)^{1/3}}\right)^{3/2}, \tag{3.31}$$

where $\zeta = b(\sigma_{app} - \sigma_P)/C_tB_0$ and B_0 is a drag coefficient defined as $d(\sigma_{app}b)/dv$ when v/C_t is extremely small. The input parameters to calculate Eq. (3.31) are included in Table 3.1.

The comparison among the simulation result, the solution of Eq. (3.16), and Eq. (3.31) are described in Fig. 3.4. According to the figures from 3.4a to 3.4d, there were large differences between Eq. (3.31) and the simulation result. Meanwhile, the solution of Eq. (3.16), or our solution, described the simulation result with an excellent accuracy when proper parameters were

used. Especially, the solution of Eq. (3.16) was fitted better in high speed regime than in low speed regime. This is because the relativistic effect is prominent when the speed of dislocation is fast enough as we assumed in our theoretical approach. More specifically, when $v/C_t \leq 0.2$, since the forward phonon scattering , which was not considered in our assumption, is significant to determine the dislocation's speed in addition to the backward scattering, our model showed the deviation from the simulation result. Also, from the fitted value, η, we found that the oscillation was underdamped and this coincides to previously reported results[86]. In addition, we could investigate influences of C_1^{dis} and C_2^{dis} on the drag force caused by relativistic effect by using Eq. (3.28). Although we assumed $\Omega b/2\pi v \ll 1$ and it led to $w_0 b/2\pi v \ll 1$, not only the oscillation but a resistance of atoms in perfect region to the oscillation was also not negligible since C_2^{dis} was much larger than C_1^{dis} listed in Table 3.1.

3.5.2 Edge dislocation in BCC crystals at 0 K

To validate our theoretical model to real materials, the motion of a single edge dislocation in both molybdenum and iron was investigated. The dislocation speed in both materials is described as a function of applied stress in Fig. 3.5a and 3.5b, respectively. As the dislocation motion in the 2D triangular lattice, the dislocation in both materials also spontaneously oscillates due to the relativistic effect during its motion. As the applied stress increases, the dislocation speed gradually approaches the transverse shear wave speed, and the oscillation effect becomes more significant. Based on this oscillation mechanism, we solve Eq. (3.16) by inserting the material properties.

First, we calculated the atomic frequency w_0 and the dislocation mobility M_{dis} by using same method introduced in section 3.5.1. Then, we inserted proper values of C_1^{dis} and C_2^{dis} into Eq. (3.16) and obtained the dislocation speed as a function of applied stress. All the parameters are summarized in Table 3.2. Based on Fig. 3.5a, when $C_1^{dis} = 0.910$ and $C_2^{dis} = 1.004$, our theoretical model described the simulation results with a high accuracy for iron. Furthermore, from Fig.3.5b, there is excellent agreement between the model and simulation results when $C_1^{dis} = 0.920$ and $C_2^{dis} = 1.002$ for molybdenum. Interestingly, both group parameters have almost the same values in both materials despite the difference in interatomic potential.

3.5.3 Edge dislocation in FCC crystals at 0 K

In this work, we simulated extended dislocation in aluminum, copper, nickel, and gold. In addition to the edge dislocation in the 2D triangular lattice and BCC crystals, the stress-drop behavior was also observed while it glides in FCC crystals. When σ_{app} that is larger than σ_P was applied to the system, the dislocation glides and σ_{act} was always smaller than σ_{app}, as shown in Fig. 3.6.

Since the extended dislocation consists of two partial dislocations, they interact with each other, which causes a forced oscillation during gliding motion. Thus, even in the low-speed regime, they are expected to oscillate. As the applied stress increases, the dislocation speed increases, and therefore an additional relativistic effect is included. Thus, two types of oscillations are mixed. By employing the same method discussed in section 3.5.2, we calculated and measured the relevant parameters and inserted them with proper C_1^{dis} and C_2^{dis} to solve Eq. (3.16). The parameters are summarized in Table 3.1. Then, the solutions were compared with the simulation results in Fig. 3.7. For aluminum, as shown in Fig. 3.7a, when $C_1^{dis} = 0.96$ and $C_2^{dis} = 1.04$, an excellent agreement between the model and simulation results was observed. In addition to aluminum, as shown in Fig. 3.7b, 3.7c, and 3.7d, there was remarkable agreement between the simulation results and theory for copper, nickel, and gold. Interestingly, as in BCC crystals, we found that all the extended dislocations in FCC crystals have almost the same C_1^{dis} and C_2^{dis} which are within 0.96-0.97 and 1.02-1.04, respectively.

3.5.4 Edge dislocation in BCC and FCC crystals under the elevated temperature

In addition to 0 K, we increased the temperature to 300 K and observed the motion of the dislocations at the elevated temperature. As shown in Fig. 3.8, the speeds of the dislocations at 300 K are much higher than those at 0 K for all crystals under the same stress. The parameters were recalculated and summarized in Table 3.3. At a finite temperature, a forced oscillation is added that causes both C_1^{dis} and C_2^{dis} to increase, as shown in Table 3.3 and Fig. 3.8. As a result, according to Eq. (3.28) with $w_0 b \ll 2v$, increasing temperature causes the oscillation drag force to increase. During the motion of dislocations at this elevated temperature, we also observed that the cores contracted into more compact structures. This is described in Fig. 3.9. Therefore, we proved that Φ_{dis} increases at a high temperature, which causes both group parameters to

increase. From Fig. 3.8, our theoretical model fitted the simulation results with a high accuracy for all cases. Especially, much larger C_1^{dis} and C_2^{dis} are required for nickel at 300 K than for the other crystals. This is because the extended dislocation shrank more rapidly in nickel than in the others as shown in Fig. 3.9g and 3.9h.

The contraction of dislocation cores as speed increases has been observed in previous simulation studies[33,91] and theoretically derived to account for relativistic effects and radiation drag during the motion of dislocations[30,92] . According to Pellegrini[92], the dependence of core width, $a(v)$, on dislocation speed is given by $a(v) = 2d|L(v + i0^+)/2e_0 + i\alpha(v/C_t)|$, where d is the interatomic plane separation, $L(v)$ is a stationary Lagrangian, $e_0(=\mu b^2/4\pi)$ is the characteristic energy per unit length of the dislocation line, and α is the drag coefficient. Here, the Lagrangian is derived as $L_s(v) = -e_0\beta_t$ and $L_e(v) = -4e_0(C_t/v)^2(\beta_l - \beta_t^{-1}\beta_{t_2}^4)$, where $\beta_t = \sqrt{1-(v/C_t)^2}$, $\beta_l = \sqrt{1-(v/C_l)^2}$, and $\beta_t = \sqrt{1-v^2/2C_t^2}$, for screw and edge dislocations, respectively[93]. Additionally, as $v \to 0$, $L_s(0) = -e_0$ and $L_s(0) = -e_0/(1-\upsilon)$, where υ is Poisson's ratio, are satisfied. Since both edge and screw dislocations show the same tendency in the core width within the subsonic regime[92], hereafter, we discuss only screw dislocations for an intuitive grasp. Hirth[93] showed that the total (self) energy of a uniformly moving screw dislocation, $E_s(v)$, satisfies $E_s(v) = e_0\beta_t^{-1}$. Thus, as the dislocation speed increases, the total energy of the dislocation increases, and the magnitude of the Lagrangian decreases. Finally, this leads to a decrease in core width. Therefore, we conclude that the contraction of the dislocation core at a high temperature observed in this study is a result of increasing dislocation self-energy.

3.6 Summary

While the dislocation moves in a discrete medium, the stress-drop behavior that is not explainable by linear elasticity theory was observed through atomistic simulations. We proved that a dynamic drag effect is responsible for this behavior. During dislocation motion, the stress-drop phenomenon was observed owing to phonon scattering around the core. As the speed of the dislocation gradually increases or as it interacts with other dislocations, the dislocation core oscillates. These oscillations induce additional phonon drag to the motion of the dislocation.

The phonon drag effect not only explains the stress-drop but also generally governs the dynamics of dislocation in a discrete system. In this work, we developed a general equation of motion for

dislocations where the drag effect is considered. The equation was derived based on the DLD theory by assuming that dislocations oscillate by various sources. There was excellent agreement between our theoretical model and the results of atomistic simulations when proper group parameters were used. Interestingly, even if the materials were different, the group parameters were almost the same as long as the lattice system did not change. Given that the group parameters quantify the magnitude of the drag force, this proves that the drag effect depends on the *geometric structure* of the dislocation core rather than the material properties. Furthermore, the simulations showed that a contraction of the dislocation cores occurs in cubic crystals as temperature increases, leading to an increase in the drag effect via an increase in the group parameters.

Our theoretical model has academic significance in that it can be *generally* applied to moving dislocations despite the diversity of the drag sources. This is possible because the drag effect manifests as an oscillation of the cores as a common result. This can be simply quantified in terms of the two grouping parameters that are defined in this chapter with a thorough analysis.

Chapter 4

Dynamic Drag on the Low-Angle Grain Boundaries (LAGBs)

This chapter is written based on the following article:

1. **Kim, S.**, Kang, K. & Kim, S. Y. Dynamic drags acting on moving defects in discrete dispersive media: from dislocation to low-angle grain boundary. *(submitted)*

4.1 Overview

In addition to dislocations, there have also been studies toward understanding the dynamics of grain boundaries (GBs). Since GBs impede the motion of dislocations[94,95] or themselves act as a source to emit dislocations by accommodating external loads[96,97,98], GBs have strong influences on the plastic deformation and recovery and recrystallization processes of polycrystalline materials. Thus, studying the atomic structure and dynamics of GBs has been emphasized for several decades[97,99,100]. Especially, since low-angle GBs (LAGBs) can alternatively be described as an array of dislocations[101,102,103], the theories that have been developed to describe dislocation dynamics can be extended to LAGBs. However, the superposition of strain fields caused by the dislocations that comprise GBs causes the nonlinear behavior of the GB to become more prominent. This makes analyses of GBs more difficult and reveals the limits of linear elasticity theory for analyzing static and dynamic GB behaviors. The structural nonlinearity of GBs governs their phonon transport, which is mainly responsible for the thermal efficiency of materials[104,105]. According to a recent work by Yasaei et al.[105], the misorientation angle of GBs is an important factor in determining the thermal resistance of graphene, which was captured through phonon scattering from GBs.

In the previous chapter, we developed the general equation of dislocation motion given that the dislocation core commonly oscillates despite the difference in the drag sources. In this chapter,

we apply the equation to the LAGBs and explain the unusual behaviors observed during the LAGB's motion that are not fully explainable by the linear elasticity theory.

4.2 Simulation setup

In order to simulate LAGBs with various misorientation angles, θ, we chose a 2D triangular lattice structure as a medium rather than a 3D complex structure. Here, we used cutoff radius $r_c = 3.726$ Å, $\varepsilon_0 = 0.7064$ eV and $\sigma = 2.267$ Å as LJ parameters defined by Filippova et al.[63] and used to simulate the dislocation in Chapter 2 and Chapter 3.

We inserted the LAGB via two steps. First, we constructed two opposite-edge dislocations separated by half of the horizontal box length in a small slab to satisfy periodic boundary conditions along the *x* direction. Second, given that an LAGB can be described as an array of dislocations, we stacked the edge dislocations along the *y* direction to form an LAGB. By artificially controlling the distance, *D*, between two neighboring dislocations based on the relationship $\theta = b/D$, we determined θ values for each LAGB. Although each GB has a different θ value, they are structurally identical because they consist of the same type of dislocation. After relaxation of the system using the same method described in the above sections, the equilibrium structures of LAGBs with four θ values (5.09°, 6.01°, 7.34°, and 9.42°) were obtained. To avoid difficulties arising from the system size influencing the speed of the LAGBs, we fixed the size of the systems to approximately 102 nm × 25 nm × 2.545 nm. Although there were differences in the size due to different θ values, the differences were negligible compared to the whole system. The LAGBs with four θ values are described in Fig. 4.1. Furthermore, since the lattice has only one atomic layer in the *z* direction, and the LAGBs consist of only a single type of dislocation, the gliding of dislocations within an LAGB plane does not need to be considered. Thus, under external shear stress, σ_{xy}, the motion of the LAGBs is confined to glide along the *x* direction on the *xz* plane. The constant shear stress was applied to every atom in the top and bottom free edges along the *x* axis in opposite directions. Each atomic position was updated every 1 fs using the Nosé–Hoover thermostat[61,62] at the desired temperature. As a result, both the LAGBs moved toward the *x* direction.

4.3 Simulation results

In order to move LAGB, a much higher stress than σ_P of a single dislocation should be applied to the free edges of the system. This is because additional energy is required for each dislocation that comprises the LAGB to overcome the energy barrier originating from interactions with other dislocations. The required energy increases as θ increases because of the decreased distances between adjacent dislocations.

While the LAGBs were in motion, as in the motion of dislocations, the stress-drop phenomenon was also observed as described in from Fig. 4.2 to 4.5 for various θ. Fig. 4.2a, 4.3a, 4.4a, and 4.5a show σ_{act} when σ_{app} was lower than the critical stress to migrate the corresponding LAGB, and Fig. 4.2b, 4.3b, 4.4b, and 4.5b show σ_{act} when σ_{app} was higher than the critical stress. During the LAGB motion, σ_{act} was lower than σ_{app} and remained steady for a while in a quasi-equilibrium state. It finally converged to σ_{app} when two opposite LAGBs approached and annihilated each other under a continuously applied load.

In addition to stress-drop, two additional unusual behaviors were observed during the motion of the LAGBs. First, the speed of the LAGBs v_{LAGB} decreased as θ increased under the same applied stress as described in Fig. 4.6. This is opposite of the result obtained by continuum dislocation theory. According to the previous continuum theory[106,107], the stress-driven LAGB motion follows

$$v_{LAGB} = M_{LAGB}\sigma\theta, \tag{4.1}$$

where M_{LAGB} is the mobility of the LAGB. In Fig. 4.6, we did not record the speed of LAGBs with misorientation angles lower than 7.34° moving under $\sigma_{app} > 6.5$ GPa because failures within the LAGB structures occurred during their motion. Since a decreased θ means an increase in distance between neighboring dislocations that comprise the LAGB, these failures might occur because the applied stress was enough to overcome interactions among them. Second, although the structure of an LAGB should be a straight line once it reaches an equilibrium state, as proved in Appendix C based on the linear elasticity theory, the simulations showed that the LAGB was rather curved for all θ values as shown in Fig. 4.7. Furthermore, the magnitude of curvature decreased as θ increased under the same load.

4.4 A general equation of the LAGB motion

For $\theta \leq 10°$, an LAGB can be regarded as an array of dislocations[108,109]. For a LAGB, unlike a single dislocation, interactions among dislocations must also be considered to analyze its dynamics. The motion of the LAGB consists of two steps, before and after the dynamic equilibrium states.

Initially, the LAGB begins to move via the motion of dislocations closest to the free edge of the system. Internal dislocations move in turn, and finally, the dislocation located at the center of the system moves as described in Fig. 4.8b. This is because the stress applied to the edge propagates in the form of a wave toward the inside of the system. Thus, the different start times of the motion of each dislocation induce the curvature of the LAGB. This leads the horizontal distance, x_h, between two neighboring dislocations to be equal to $vb/C_t\theta$. From Fig. 4.6, v decreases as θ increases. As a result, the increasing misorientation angle causes x_h to decrease such that the curvature of the LAGB decreases. This is identical to the simulation results described in Fig. 4.7.

Once the LAGB is in steady motion, however, it maintains the curved shape despite its high potential energy as described in Fig. 4.8c. If an imaginary stress, σ_{img}, acts on the system to cause it to be in equilibrium with the curved LAGB, the force equilibrium equation should satisfy Eq. (4.2) for each constituent dislocation. The forces that satisfy Eq. (4.2) are denoted by arrows in Fig. 4.9. Based on the figure, σ_{img} always points toward the direction opposite the motion of the LAGB. Therefore, it is expected that σ_{img} drags the LAGB motion.

$$\sigma_{\text{int}}^{j} + \sigma_{app} + \sigma_{img} = 0 \quad (\text{for } j = 1, 2, \cdots N), \tag{4.2}$$

where

$$\sigma_{\text{int}}^{j} = \frac{\mu b}{2\pi(1-\nu)} \sum_{\substack{i=1 \\ (i \neq j)}}^{N} \frac{(x_j - x_i)[(x_j - x_i)^2 - (y_j - y_i)^2]}{[(x_j - x_i)^2 + (y_j - y_i)^2]^2}.$$

When the LAGB is in motion, it does not rigidly translate but is instead accompanied by transverse oscillations because its constituent dislocations are interacting with each other. Although the exact calculation of the oscillation amplitude of each dislocation is quite difficult, we roughly describe it in the frame of the discrete lattice model by simply assuming that each dislocation is connected by a spring that is elongated by the external stress. Then, the oscillation amplitude, x_{osc}, can be expressed as $x_{osc} = \alpha x_h = \alpha vb/C_t\theta$, where $0 < \alpha < 1$. Since the

speed of the dislocation is roughly proportional to the applied stress, we can alternatively express the oscillation amplitude here as $x_{osc} = \Psi x_{app}/\theta$, where Ψ is a function of applied stress. As a result, the elongation as a function of time becomes $x(t) = \left(\Psi x_{app}/\theta\right)\sin(\Omega_{LAGB} t)$, where Ω_{LAGB} is the LAGB oscillation frequency. This elongation induces the oscillation of each dislocation, which becomes a source of drag. This drag causes the LAGB to maintain its curved structure. Since our goal is not an exact derivation of the force acting on the LAGB but a simple description of its resultant behavior, and so further mathematical derivation is identical to that used in Section 3.4. As a result, the actual internal stress is related to the external stress by

$$\sigma_{act} = \left(1 - \frac{C_1^{LAGB}}{\theta} + \frac{w_0^2 b^2}{4\pi^2 v^2}\left(\frac{C_2^{LAGB}}{\theta} - 1\right)\right)\sigma_{app}, \tag{4.3}$$

where

$$\begin{aligned} C_1^{LAGB} &= \frac{2D\Psi\Phi_{LAGB}}{\pi^2 M\Omega_{LAGB}}, \\ C_2^{LAGB} &= \frac{D\Psi\Phi_{LAGB}\Omega_{LAGB}}{Mw_0^2}. \end{aligned} \tag{4.4}$$

In Eq. (4.4), Φ_{LAGB} is defined as

$$\Phi_{LAGB} \equiv \int_0^{\pi}\int_0^{\pi} \frac{\cos\left(\frac{x}{2}\right)\cos\left(\frac{y}{2}\right)}{\left(\frac{w_0}{\Omega_{LAGB}}\right)^2\left(\sin^2\left(\frac{x}{2}\right) + \sin^2\left(\frac{y}{2}\right)\right) - 1} dxdy. \tag{4.5}$$

Therefore, the constitutive equation of motion of the LAGB becomes

$$v^3 - M_{dis}\sigma_{app}\left(1 - \frac{C_1^{LAGB}}{\theta}\right)v^2 - M_{dis}\sigma_{app}\frac{w_0^2 b^2}{4\pi^2}\left(\frac{C_2^{LAGB}}{\theta} - 1\right) = 0. \tag{4.6}$$

4.5 Applications

Considering that the dislocations comprising LAGBs interact with each other and thereby cause drag to the LAGB motion, the LAGB motion can be regarded as an extension of the motion of extended dislocations introduced in the previous section. However, each dislocation interacts with all other dislocations, not just with a single one, and thus the motion of LAGBs is more

complicated than that of extended dislocations. It is also expected that the interactions within the LAGB become a stronger drag source than in the single dislocation case.

The oscillation of a curved LAGB can be regarded as an oscillating string, whose length is L_{string}, effective line density is ρ^*_{LAGB}, and line tension per thickness is T^*_{LAGB}, as shown in Fig. 4.10a. The fundamental frequency of the string, Ω_{LAGB}, is expressed as $\Omega_{LAGB} = (2L_{string})^{-1}\sqrt{T^*_{LAGB}/\rho^*_{LAGB}}$. Here, since the effective line density is directly proportional to the effective mass of the LAGB, m^*_{LAGB}, we roughly estimate the frequency of the LAGB by deriving its effective mass. Note that this is not a real mass but a quantity that is 'physically' similar to the mass. Effective mass has been defined in various forms depending on its derivation[93,111,112]. In this study, we mainly follow the method developed by Brailsford[110,111] given that the discreteness of the lattice is considered. However, since his method can be applied only to single dislocations, we extended it to apply to LAGBs with some modifications. We assumed that the LAGB consists of $2N+1$ dislocations embedded in a medium of density ρ. As a result, the effective mass of the LAGB is derived as

$$m^*_{LAGB} = (2N^2 + 4N + 1)m^*_{dis} + \frac{\rho b^2}{4\pi^2}\sum_{k=1}^{2N}\sum_{n=1}^{\infty}(2N+1-k)\frac{(-1)^n(q_D kd)^{2n}}{n(2n)!}\int_0^{2\pi}(f(\theta))^{2n}g(\theta)d\theta, \tag{4.7}$$

where

$$m^*_{dis} = (\rho b^2/4\pi)(1+r)\ln(q_D/\sigma), \tag{4.8.1}$$

$$f(\theta) = \sin\theta + (v/C_t)\cos\theta, \tag{4.8.2}$$

$$g(\theta) = 1-(1-r)\sin^2 2\theta. \tag{4.8.3}$$

Here, m^*_{dis} is the effective mass of a single edge dislocation, d is the distance between neighboring dislocations, and q_D is the Debye cutoff, which is equal to $(6\pi^2/\Gamma)^{1/3}$, where Γ is the atomic volume in real space. A detailed derivation of Eq. (4.7) is introduced in Appendix D. According to Eq. (4.7), the effective mass of the LAGB is not just a simple sum of that of its dislocations, or $(2N+1)m^*_{dis}$. Rather, the LAGB has a much larger effective mass that is proportional to the square of the number of dislocations with an extra term. This is because each dislocation interacts not only with its nearest neighbors but also with all other dislocations that comprise the LAGB. This complicates interactions between dislocations, slowing the LAGB and

leading to a significant decrease in its oscillation frequency, Ω_{LAGB}.

Since the relationship $C_2^{LAGB}/C_1^{LAGB} = (\pi\Omega_{LAGB}/\sqrt{2}w_0)^2$ is satisfied for the LAGB, we expect that C_2^{LAGB}/C_1^{LAGB} is much smaller than for a single dislocation. All the parameters to solve Eq. (4.6) are summarized in Table 4.1. Here, M_{dis} and w_0 were computed from an atomistic simulation of a single dislocation and perfect lattice using the same sized simulation box and LJ potential parameters, respectively. C_1^{LAGB} and C_2^{LAGB} were used as phenomenological parameters that depend on applied stress to compare with the simulation results. Strictly speaking, C_2^{LAGB}/C_1^{LAGB} depends on both misorientation angle and applied stress, but we assume that the ratio changes mainly as a result of changes in applied stress because the difference between the minimum and maximum misorientation angles used in this work is less than 5°, which is an extremely small value. Thus, we expect that this simplification does not influence the main result of our work. According to Wei and Peng[32], they used the frequency of transverse phonons—which is the main source of radiation drag during dislocation motion in the subsonic regime—as a phenomenological parameter to fit dislocation travel distance over time. In their work, they used a larger frequency as the applied strain rate increases. With reference to their results, we assumed that Ω_{LAGB} increases with increasing applied stress in this study, which causes C_1^{LAGB} to decrease and C_2^{LAGB} to increase according to Eq. (4.4). This is reflected in Table 4.1. As a result, we inversely calculated Ω_{LAGB} by the relationship $\Omega_{LAGB} = (w_0/\pi)\sqrt{2C_2^{LAGB}/C_1^{LAGB}}$ using the values listed in Table 4.1 to be within the range of 1.51~1.60 THz. Given that this range of frequencies is similar to the frequency spectrum in which a dislocation array acts as an effective phonon scattering source for lattice heat conduction[104,114], our estimate of C_1^{LAGB} and C_2^{LAGB} is reasonable. A comparison between the solution of Eq. (4.6) and simulation results is shown in Fig. 4.11. As a result, for the valid C_1^{LAGB} and C_2^{LAGB}, our theoretical model describes an inverse relationship between the speed and misorientation angle of LAGBs, which cannot be explained in terms of linear elasticity theory, with high accuracy. Therefore, it proves that the phonon drag effect occurring due to elastic interactions among dislocations comprising the LAGB is responsible for this relationship. This effect should be considered when the LAGB moves in a dispersive medium.

4.6 Summary

In addition to stress-drop that was also observed during the dislocation motion, two unusual phenomena were observed during the motion of LAGBs. First, the speed was inversely proportional to the misorientation angle. Second, the LAGB maintained a curved form, even in an equilibrium state. Both results cannot be explained solely by the linear elasticity theory. However, by introducing the drag effect originating from interactions among constituent dislocations of the LAGB, both unusual behaviors could be explained. Furthermore, our proposed model could explain the mobility of LAGBs given that they oscillate in a manner similar to dislocations. Especially, since LAGBs consist of a number of dislocations with more complicated interactions than that of an extended dislocation, the drag effect on the LAGB motion is characterized by a significant decrease in its oscillation frequency. Based on this analysis, we solved the equation by inserting the roughly estimated group parameters and fitted the solutions to the simulation results. As a result, the inverse relationship between the speed and misorientation angle of LAGBs could be explained with high accuracy.

Chapter 5
Configurational Drag Force on a Dislocation

This chapter is written based on the following article:

1. **Kim, S.,** Kim, H. & Kim, S. Y. Configurational force on a dynamic dislocation with localized osicllation. *(submitted)*

5.1 Overview

A motion of dislocation is determined by solving an equation of its motion. Unlike the Newtonian force, however, a mass is not defined for defects (including the dislocation). Instead, the net translational force on the defect can be quantified by defining *configurational force*, or *J*-integral, which is given by an integral form[115,116]. Without defining the defect mass, the *J*-integral is directly obtained by the derivative of Lagrangian of the system with respect to the defect's translation coordinate. Or, it can be obtained by surface integral of energy-momentum tensor[117]. The *J*-integral physically means energy release rate for the defect translation and it was proved that it is independent to the integration path around a stationary defect by using the conservation theorems[118]. As a result, the *J*-integral is equal to Peach-Koehler force for the stationary dislocation[117]. Starting from the simplest case of stationary dislocation, the *J*-integral has been widely applied to characterize the state of dislocation with considering complex cases[119,120,121]. Recently, Baxevanakis and Giannakopoulos[122] calculated material force on the edge dislocation by using the *J*-integral with including thermo-elastic deformation. And Ballarini and Royer-Carfagni[123] reinterpreted the configurational force on the dislocation in terms of the resultant of the Newtonian contact forces by assuming the dislocation as an inclusion that has perturbed configuration.

In addition to the stationary defects, the *J*-integral has been applied to the dynamic ones[124,125,126]. Compared to the stationary *J*-integral, the pseudo-momentum term additionally contributes to the

dynamic *J*-integral but the path-independency is still maintained as long as the defect moves with uniform velocity[126]. As a result, the dynamic *J*-integral is still equal to Peach-Koehler force when the dislocation is in steady motion[127]. According to continuum elastodynamics, the resolved shear stress required for the steadily moving dislocation must be zero. Given that driving force always acts on the moving dislocation, the drag force that acts opposite to the driving force must exist to satisfy the force balance. Since the drag force $\mathbf{F}^{drag}$ is attributed to rate of energy dissipation $\dot{Q}$ from the dislocation core, they can be related by $\dot{Q} = -\mathbf{F}^{drag} \cdot \mathbf{v}$ where $\mathbf{v}$ is dislocation velocity. Moreover, since the drag force has influence on the dislocation inertia through the equation of dislocation motion, the dislocation core width and its self-force are changed over time when the dislocation moves non-uniformly[92]. However, the existence of energy dissipation sources breaks the path-independency of the *J* integral and thus it is difficult to exactly trace the energy release rate in this case[128].

In this Chapter, we theoretically derive the *J*-integral around a uniformly moving dislocation where the drag effect is considered. We characterize the drag effect by assuming that the dislocation oscillates based on the lattice dynamics theory. Unlike the continuum theory, the lattice dynamics theory expects that the frequency spectrum of the system is bounded. Therefore, divergence problems that appear in the field theory can be avoided[82]. Depending on whether newly generated frequencies by the dislocation deviate the frequency band of the perfect lattice or not, the oscillation types are classified into two cases. First, if the dislocation frequency is above the maximum frequency of perfect lattice, the oscillation amplitude is localized around the dislocation core so it exponentially decays as the distance moves away from the core. Thus, the dislocation core can be treated as an isolated defect[81]. This type of oscillation can be applied to the dynamic dislocation when the fluttering drag predominates its motion. On the contrary, if the dislocation frequency exists within the frequency band of perfect lattice, the waves are elastically scattered rather than be localized. Thus, this type of oscillation can be applied to when the phonon scattering becomes the dominant drag mechanism. Here, we only deal with the former type of oscillation, or the localized oscillation. And we express the drag force by using the dislocation-phonon coordinates rather than conventional atomic displacements coordinates. Then, the dislocation oscillation is examined by solving matrix eigenvalue problems and finally the contribution of each eigenmode to the drag force is revealed with considering a discrete nature of the dislocation core.

5.2 Continuum approach

Before we discuss main results of our work in next section, we briefly introduce a derivation of the configurational force acting on uniformly moving dislocation based on continuum theory. This was carried out by Stroh[127] and we reproduce it here to show that *J*-integral calculated for a static dislocation is still identically applied to it for a moving one unless it accelerates.

5.2.1 Lagrangian

Imagine a system that consists of two separated regions I and II as in Fig. 5.1. In region I, a dislocation loop, which is denoted as *D*, is inserted and it is surrounded by a surface Σ_i. Thus, Σ_i has a tube shape whose radius is a. And assume that there is other singularities or stress sources, which is denoted as *S*, in region II, which is surrounded by inner and outer surfaces, Σ_i and Σ_o, respectively. As a result, we can express total Lagrangian of the system L, as

$$L = L^D + L^S + L^{DS}, \tag{5.1}$$

where L^D and L^S are Lagrangians of *D* and *S*, respectively and L^{DS} is Lagrangian occurred by interaction between them. As the dislocation moves, a distance between *D* and *S* changes and this will cause a change in L^{DS}. If ξ specifies a position of the dislocation, the configurational force acting on the dislocation along ξ direction, F_ξ, is defined as

$$\int_{t_1}^{t_2} F_\xi \delta\xi \, dt = \delta \int_{t_1}^{t_2} L^{DS} \, dt. \tag{5.2}$$

If we define stresses and displacements occurred by *D* and *S* as σ^D and σ^S, and u^D andu^S, respectively, the interaction potential energy, U^{DS}, becomes

$$U^{DS} = \int_{\mathrm{I+II}} (\sigma_{ij}^D u_{i,j}^S + \sigma_{ij}^S u_{i,j}^D) d^3x, \tag{5.3}$$

Since an elastic displacement is not defined at an singularity, u^D andu^S are not defined at *D* and *S*, respectively. As a result, Eq. (5.3) is divided into

$$U^{DS} = \int_{\mathrm{I}} \sigma_{ij}^D u_{i,j}^S \, d^3x + \int_{\mathrm{II}} \sigma_{ij}^S u_{i,j}^D \, d^3x. \tag{5.4}$$

Using an integration by parts on second term in right-hand side (RHS) of Eq. (5.4) leads to Eq. (5.5).

$$U^{DS} = \int_{\Sigma_o} \sigma_{ij}^S u_i^D \, dS_j - \int_{\Sigma_i} \sigma_{ij}^S u_i^D \, dS_j - \int_{\mathrm{II}} \sigma_{ij,j}^S u_i^D \, d^3x + \int_{\mathrm{I}} \sigma_{ij}^D u_{i,j}^S \, d^3x. \tag{5.5}$$

The first integral in Eq. (5.5) represents a supplied energy from the external mechanism to the system and thus it means a decrease in potential energy of the external mechanism. Therefore, if we extend the system's body to include the external mechanism, the first integral in Eq. (5.5) is cancelled out. According to Fig. 5.1b, since the surface integral on Σ_i in Eq. (5.5) cross a cut surface, *C*, a displacement jump occurs as much as b, which is Burgers vector of the dislocation loop. And the elastic self-displacement field of dislocation whose length is l, u^D, has an order $O(\ln a)$ so the second term in Eq. (5.5) satisfies

$$\int_{\Sigma_i} \sigma_{ij}^S u_i^D \, dS_j \sim -b_i \int_C \sigma_{ij}^S \, dS_j + \int_0^l \sigma_{ij}^S (\ln a)(2\pi a) dl = -b_i \int_C \sigma_{ij}^S \, dS_j + O(a \ln a). \tag{5.6}$$

And since $\sigma^S \sim 1/r$ within volume I, the last term in RHS of Eq. (5.5) becomes

$$\int_{I_i} \sigma_{ij}^D u_{i,j}^S \, dS_j \sim \int_0^a \int_0^l \frac{1}{r} u_{i,j}^D (2\pi r) \, dl \, dr = O(a). \tag{5.7}$$

As a result, as $a \to 0$, Eq. (5.5) becomes

$$U^{DS} = b_i \int_C \sigma_{ij}^S \, dS_j - \int_{\mathrm{I+II}} \sigma_{ij,j}^S u_i^D \, d^3x. \tag{5.8}$$

If material velocities caused by *D* and *S* is be defined as v^D and v^S, respectively, Eq. (5.8) is changed to Eq. (5.9) by force equilibrium equation.

$$U^{DS} = b_i \int_C \sigma_{ij}^S \, dS_j - \int_{\mathrm{I+II}} \rho u_i^D \dot{v}_i^S \, d^3x, \tag{5.9}$$

where ρ is the density of system. The kinetic energy caused by interaction between *D* and *S* is expressed by

$$T^{DS} = \int_{\mathrm{I}} \rho v_i^D v_i^S \, d^3x + \int_{\mathrm{II}} \rho v_i^D v_i^S \, d^3x. \tag{5.10}$$

Within region I, since $u^D \sim \ln r$,

$$T^{DS} \sim \int_{\mathrm{II}} \rho v_i^D v_i^S \, d^3x + \int_0^l \int_0^a \rho \frac{1}{r} (2\pi r) \, dr \, dl = \int_{\mathrm{II}} \rho v_i^D v_i^S \, d^3x + O(a). \tag{5.11}$$

Here, notice that v_i^D is well defined in region II because *D* lies wholly in region I. From Eq. (5.9) and (5.11) with $a \to 0$, L^{DS} is derived as Eq. (5.12).

$$\begin{aligned} L^{DS} &= T^{DS} - U^{DS} \\ &= -b_i \int_C \sigma_{ij}^S \, dS_j + \int_{\mathrm{I+II}} \rho (u_i^D \dot{v}_i^S + \dot{u}_i^D v_i^S) \, d^3x \\ &= -b_i \int_C \sigma_{ij}^S \, dS_j + \int_{\mathrm{I+II}} \rho \frac{d}{dt} (u_i^D v_i^S) \, d^3x. \end{aligned} \tag{5.12}$$

5.2.2 Configurational force

By using Eq. (5.2), the configuration force was derived from Eq. (5.12) by Stroh[127]. Assume that the dislocation loop, *D*, moves infinitesimal distance, $\delta\xi$, as shown in Fig. 5.2. Then, a variation of Eq. (5.12) becomes

$$\begin{aligned} \delta L^{DS} &= -\delta\left(b_i \int_C \sigma_{ij}^S \, dS_j \right) + \delta\left(\int_{\mathrm{I+II}} \rho \frac{d}{dt} (u_i^D v_i^S) \, d^3x \right) \\ &= -b_i \int_{\delta V} \sigma_{ij,j}^S \, d^3x + b_i \oint \sigma_{ij}^S \varepsilon_{jkl} ds_k \delta\xi_l + \delta \int_{\mathrm{I+II}} \rho \frac{d}{dt} (u_i^D v_i^S) \, d^3x, \end{aligned} \tag{5.13}$$

where δV is infinitesimal volume change due to the dislocation motion, S_k is unit vector along the dislocation line and ε_{jkl} is a permutation tensor. By force equilibrium equation without body force, $\sigma_{ij,j}^S = \rho \dot{v}_i^S$ is satisfied so the first term in RHS of Eq. (5.13) becomes Eq. (5.14).

$$b_i \int_{\delta V} \sigma_{ij,j}^S \, d^3x = \rho b_i \int_{\delta V} \dot{v}_i^S \, d^3x. \tag{5.14}$$

Since the dislocation, *D*, is only moving one, not *S*, so the variation of last term in Eq. (5.13) is applied only to u^D with the volume change, δV. As a result, the last term in Eq. (5.13) becomes Eq. (5.15).

$$\delta \int_{\mathrm{I+II}} \rho \frac{d}{dt} (u_i^D v_i^S) \, d^3x = \int_{\mathrm{I+II}} \rho \frac{d}{dt} (\delta u_i^D v_i^S) \, d^3x + \int_{\delta V} \rho \frac{d}{dt} (u_i^D v_i^S) \, d^3x \tag{5.15}$$

Since $u_i^D = b_i$ is satisfied within δV, Eq. (5.15) becomes

$$\delta \int_{\mathrm{I+II}} \rho \frac{d}{dt} (u_i^D v_i^S) \, d^3x = \int_{\mathrm{I+II}} \rho \frac{d}{dt} (\delta u_i^D v_i^S) \, d^3x + \rho b_i \int_{\delta V} \dot{v}_i^S \, d^3x. \tag{5.16}$$

As a result, as we insert Eq. (5.14) and (5.16) into Eq. (5.13), Eq. (5.17) is derived.

$$\delta L^{DS} = b_i \oint \sigma_{ij}^S \varepsilon_{jkl} ds_k \delta\xi_l + \int_{\mathrm{I+II}} \rho \frac{d}{dt} (\delta u_i^D v_i^S) \, d^3x = L_1^{DS} + \delta L_2^{DS}. \tag{5.17}$$

If we define the first and second integrals in Eq. (5.17) are defined as δL_1^{DS} and δL_2^{DS}, respectively, the force acting on *D* that δL_1^{DS} contributes to is derived as Eq. (5.18) according to Eq. (5.2).

$$F_{\xi}^{1} = b_i \sigma_{ij}^{S} \varepsilon_{jkl} t_k \,, \tag{5.18}$$

where t_k is unit dislocation line vector. And the integration of δL_2^{DS} in Eq. (5.17) can be divided as

$$\begin{aligned} \delta L_2^{DS} &= \int_{\mathrm{I}} \rho \frac{d}{dt}(\delta u_i^D v_i^S)\, d^3x + \int_{\mathrm{II}} \rho \frac{d}{dt}(\delta u_i^D v_i^S)\, d^3x \\ &= \int_{\mathrm{I}} \rho \frac{d}{dt}(\delta u_i^D v_i^S)\, d^3x + \frac{d}{dt}\int_{\mathrm{II}} \rho \delta u_i^D v_i^S \, d^3x - \int_{\mathrm{II}} \rho \delta u_i^D v_i^S \frac{d}{dt}(d^3x). \end{aligned} \tag{5.19}$$

Since ξ is defined as the position of dislocation relative to stationary observer, or a point at region II, $d(d^3x)/dt = -\dot{\xi}_j dS_j$ is satisfied at region II. And since $\delta\xi$ is zero at $t = t_1$ and $t = t_2$, $(d/dt)\int_{\mathrm{II}} d^3x$ term does not contribute to force on the dislocation. As a result,

$$\begin{aligned} \delta L_2^{DS} &= \int_{\mathrm{I}} \rho \frac{d}{dt}(\delta u_i^D v_i^S)\, d^3x + \int_{\Sigma_i} \rho \delta u_i^D v_i^S \dot{\xi}_j dS_j \\ &= \int_{\Sigma_i} \rho \delta u_i^D v_i^S \dot{\xi}_j dS_j + \int_{\mathrm{I}} \rho v_i^S \frac{d}{dt}(\delta u_i^D)\, d^3x + \int_{\mathrm{I}} \rho \dot{v}_i^S \delta u_i^D \, d^3x. \end{aligned} \tag{5.20}$$

Here, since $u_i^D \sim \ln r$ in region I, $\delta u_i^D \sim 1/r$ so that

$$\int_{\mathrm{I}} \rho \dot{v}_i^S \delta u_i^D d^3x \sim \int_0^l \int_0^a \rho \dot{v}_i^S \frac{1}{r}(2\pi r)\, dr\, dl = O(a). \tag{5.21}$$

As $a \to 0$, thus δL_2^{DS} results in

$$\delta L_2^{DS} = \int_{\Sigma_i} \rho \delta u_i^D v_i^S \dot{\xi}_j dS_j + \int_{\mathrm{I}} \rho v_i^S \frac{d}{dt}(\delta u_i^D)\, d^3x. \tag{5.22}$$

Here, δL_2^{DS} depends on material velocity v^S, or velocity of the observer. For our case, the observer's frame does not move so that $v^S = 0$. Therefore, the configurational force acting on the dynamic dislocation is calculated by using Eq. (5.18), which is equal to Peach-Koehler (PK) force defined for stationary dislocation. However, even if the observer's frame moves, the equivalence is still satisfied unless it accelerates. This is because we can make δu^D arbitrary small inside region I according to the continuity assumption by suitably restricting $\delta\xi$. As a result,

it is possible to make the contribution of δL_2^{DS} be arbitrary small compared to it of δL_1^{DS} to the configurational force. In fact, Eq. (5.22) is responsible to the force called *Lorentz force*, but it was proved that it does not have influence on the dislocation glide[127,129,130] .

5.3 Definition of the coordinate system in a discrete lattice

In mechanics, Lagrangian of the system is generally described in terms of displacements of consisting atoms. However, since our interest is to directly describe interaction between strain field around the dislocation and phonons, we change the conventional displacement coordinate system to dislocation-phonon coordinate system by adopting *dislocation coordinate* that was firstly suggested by Ninomiya[131]. First, we introduce the coordinate transformation based on Ninomiya[131]'s work. Then, we define *J*-integral around dynamic dislocation in the transformed coordinate system.

We simplify the system as an one-dimensional chain that consists of N atoms. Thus, the system has N degrees of freedom (DOFs). However, as a single dislocation is inserted inside of the system, the DOFs of the system are reduced to $N-1$ since 1 DOF is assigned to describe strain field of the dislocation. If we plot the system's energy as a function of N -dimensional abscissas, $\{u_1, u_2, \cdots, u_N\}$ where u_n corresponds to a displacement of n-th atom, the energy surface will be described as shown in Fig. 3. In the figure, there are two valleys. The global minimum state (state G) corresponds to the system where no defect exists. And the local minimum state (state L) corresponds to the system where the dislocation is inserted. As the dislocation glides, the system's state will move along the local minimum valley on the N -dimentional energy surface with changing displacement of each atom over time. From this, we can define the *dislocation coordinate*, ξ, as a collective variable that is expressed in terms of $\{u_1^{dis}, u_2^{dis}, \cdots, u_N^{dis}\}$, where u_n^{dis} is a displacement of n-th atom that is required to accommodate the dislocation. Physically, ξ represents a position of the dislocation. If 1 DOF is assigned to ξ, then $N-1$ DOFs are remained. The remaining DOFs are orthogonal to ξ, so they induce the climbing the sides of the local minimum valley in Fig. 5.3. Physically, these $N-1$ variables correspond to phonons that disturb the dislocation glide along the local energy minimum valley and hereafter we define them as *phonon coordinates*.

If the dislocation is in static equilibrium state, the displacement field around it, $w^S(x-\xi)$, can be described as shown in Fig. 5.4a. And if it is defined by using $\lambda^{(1)}(x-\xi)$,

$$w^s(x-\xi) = \int_{-\infty}^{\xi} \lambda^{(1)}(x-\xi')\,d\xi', \tag{5.23}$$

then $\lambda^{(1)}(x-\xi) = dw^S/d\xi$ is satisfied and it becomes a localized function around ξ as described in Fig. 5.4b. Here, $\lambda^{(1)}(x-\xi)$ is normalized as Eq. (5.24).

$$\sum_n (\lambda^{(1)}(nb-\xi))^2 = 1. \tag{5.24}$$

Also, $w^S(x-\xi)$ should satisfy Eq. (5.25) as a boundary condition.

$$\lim_{\xi\to\infty} w^s(x-\xi) = b, \tag{5.25}$$

where b is Burgers vector. Hereafter, we are going to use alternate expression as $\lambda_n^{(1)}(\xi) \equiv \lambda^{(1)}(x-\xi)$ for the convenience. From the shape of $\lambda_n^{(1)}(\xi)$ in Fig. 5.4b, it can be inferred that $\lambda_n^{(1)}(\xi)$ physically implies the compactness of dislocation core.

And if we define additional variables, $\lambda_n^{(j)}(\xi)$ for $j = 2, 3, \cdots, N$ and express atomic displacement u_n by using $\{\lambda_n^{(1)}, \lambda_n^{(2)}, \cdots, \lambda_n^{(N)}\}$ as a basis, Eq. (5.26) is derived.

$$u_n = w^s(\xi) + \sum_{v=2}^{N} \tau_v \lambda_n^{(v)}(\xi). \tag{5.26}$$

Here, since $\lambda_n^{(1)}, \lambda_n^{(2)}, \cdots, \lambda_n^{(N)}$ should be orthogonal to each other, Eq. (5.27) is followed.

$$\sum_n \lambda_n^{(\mu)}(\xi)\lambda_n^{(v)}(\xi) = \delta_{\mu v} \qquad (\mu, v = 1, 2, \cdots, N), \tag{5.27}$$

where $\delta_{\mu v}$ is a Kronecker delta. While the dislocation glides, phonons occur and they cause additional atomic displacement, which makes the system deviated from the static equilibrium state. The contribution of phonons to the displacement is reflected by the second term in RHS of Eq. (5.26). By using Eq. (5.26), the Lagrangian can be expressed in terms of new coordinates $\{\xi, \tau_2, \tau_3, \cdots, \tau_N\}$. However, it is not practical because $\lambda_n^{(2)}, \cdots, \lambda_n^{(N)}$ are not known and the constraint, Eq. (5.27), makes the calculation complicated.

To avoid these difficulties, Ninomiya[131] suggested a method by changing a basis set with adding a single redundant variable, τ_1, to the system. As a result, the total number of variables becomes $N+1$ and system's DOF becomes N. Physically, the addition of variable corresponds to the process of addition of isolated free oscillator to the dislocated system, L^{sys}. The Lagrangian of

added oscillator is defined as

$$L_{add} = \frac{1}{2} m \dot{\tau}_1^2 - \frac{1}{2} m \omega_1^2 \tau_1^2 , \tag{5.28}$$

where m is an atomic mass and ω_1 is a frequency of the added oscillator. And if we define new variables as

$$\begin{aligned} \upsilon_n &= \sum_{v=1}^{N} \tau_v \lambda_n^{(v)}(\xi), \\ \tau_v &= \sum_{n=1}^{N} \upsilon_n \lambda_n^{(v)}(\xi), \end{aligned} \tag{5.29}$$

we can express u_n and τ_1 in terms of these new variables by Eq. (5.30).

$$\begin{aligned} u_n &= w^s(\xi) + \sum_{v=2}^{N} \tau_v \lambda_n^{(v)}(\xi) \\ &= w^s(\xi) + \upsilon_n - \tau_1 \lambda_n^{(1)}(\xi) = w^s(\xi) + \upsilon_n - \left(\sum_{m=1}^{N} \upsilon_m \lambda_m^{(1)}(\xi) \right) \lambda_n^{(1)}(\xi), \end{aligned} \tag{5.30-1}$$

$$\tau_1 = \sum_{n=1}^{N} \upsilon_n \lambda_n^{(1)}(\xi). \tag{5.30-2}$$

In Eq. (5.30), since $\lambda_n^{(2)}, \cdots, \lambda_n^{(N)}$ are not required but $\lambda_n^{(1)}(\xi)$ that is explicitly known is only used, coordinate transformation from $\{u_1, u_2, \cdots, u_N, \tau_1\}$ to $\{\xi, \upsilon_1, \upsilon_2, \cdots, \upsilon_N\}$ can be conveniently carried out. Furthermore, the orthogonality constraint is automatically reflected to relate υ_n and τ_v in Eq. (5.29), no constraint is necessary. In consequence, the transformed coordinate system consists of the dislocation coordinate ξ and N phonon coordinates, $\upsilon_1, \upsilon_2, \cdots, \upsilon_N$.

5.4 *J*-integral in dislocation-phonon coordinate system

By using the transformed coordinate system $\{\xi, \upsilon_1, \upsilon_2, \cdots, \upsilon_N\}$, *J*-integral can be derived. Since *J*-integral physically means a translational configurational force per unit length of dislocation, it can be defined by using the dislocation coordinate as

$$J = -\frac{1}{l} \frac{\partial L^{sys}}{\partial \xi} = -\frac{1}{l} \left(\frac{\partial T^{sys}}{\partial \xi} + \frac{1}{l} \frac{\partial U^{sys}}{\partial \xi} \right), \tag{5.31}$$

where l is a length of dislocation, T^{sys} and U^{sys} are kinetic and potential energies of the system, respectively. Here, T^{sys} and U^{sys} are expressed as

$$T^{sys} = \frac{1}{2} m \sum_{n=1}^{N} \dot{u}_n^2 , \tag{5.32-1}$$

$$U^{sys} = \frac{1}{2} \gamma \sum_{n=2}^{N} (u_n - u_{n-1})^2 + \sum_{n=1}^{N} V(u_n), \tag{5.32-2}$$

where γ is a spring constant and V is a substrate potential. The kinetic term in Eq. (5.31) can be dissociated by a chain rule as

$$\frac{\partial T^{sys}}{\partial \xi} = \sum_{n=1}^{N} \frac{\partial T^{sys}}{\partial u_n} \frac{\partial u_n}{\partial \xi} + \frac{\partial T^{sys}}{\partial \tau_1} \frac{\partial \tau_1}{\partial \xi} . \tag{5.33}$$

Since $\partial T^{sys}/\partial u_n = 0$ and $\partial T^{sys}/\partial \tau_1 = 0, \partial T^{sys}/\partial \xi = 0$ finally becomes zero. In similar way, the potential term in Eq. (5.31) follows

$$\frac{\partial U^{sys}}{\partial \xi} = \sum_{n=1}^{N} \frac{\partial U^{sys}}{\partial u_n} \frac{\partial u_n}{\partial \xi} + \frac{\partial U^{sys}}{\partial \tau_1} \frac{\partial \tau_1}{\partial \xi} . \tag{5.34}$$

And by Eq. (5.30),

$$\frac{\partial u_n}{\partial \xi} = \frac{dw^s}{d\xi} - \left[\frac{d\lambda_n^{(1)}}{d\xi} \sum_{m=1}^{N} \lambda_m^{(1)} \upsilon_m + \lambda_n^{(1)} \sum_{m=1}^{N} \frac{d\lambda_m^{(1)}}{d\xi} \upsilon_m \right] \tag{5.35}$$

is derived. With using that $\partial U^{sys}/\partial \tau_1 = 0$, as Eq. (5.33), (5.34), and (5.35) are inserted to Eq. (5.31), then *J*-integral is derived as

$$J = \frac{1}{l} \sum_{n=1}^{N} \frac{\partial U^{sys}}{\partial u_n} \frac{dw_n}{d\xi} - \frac{1}{l} \sum_{n=1}^{N} \frac{\partial U^{sys}}{\partial u_n} \left(\frac{d\lambda_n}{d\xi} \sum_{m=1}^{N} \lambda_m \upsilon_m + \lambda_n \sum_{m=1}^{N} \frac{d\lambda_m}{d\xi} \upsilon_m \right). \tag{5.36}$$

Here, $\lambda_n^{(1)}$ was replaced by λ_n for convenience.

Given that $\lambda_n(\xi)$ is a localized function around ξ, we assume that it is a gaussian distribution function as defined in Eq. (5.37).

$$\lambda_n(\xi) = \lambda(r;\xi) = \frac{b}{\sigma_D \sqrt{2\pi}} e^{\frac{(r-\xi)^2}{2\sigma_D^2}} , \tag{5.37}$$

where $r = nb$ and σ_D is a standard deviation of the distribution function and is used as a parameter that characterizes the size of dislocation core. In other words, we describe the dislocation core as a diffusive zone, whose width is around $2\sigma_D$. Note that Eq. (5.37) also satisfies the boundary condition, Eq. (5.25). Since $\partial U^{sys}/\partial u_n = (\tau_{app} + \tau_{dis})l\mathrm{b}$ where τ_{dis} is the dislocation stress field and $dw_n/d\xi = \lambda_n$, the first term in RHS of Eq. (5.36) in continuum limit becomes

$$J_1 = \frac{1}{l}\sum_n \frac{\partial U^{sys}}{\partial u_n}\frac{dw_n}{d\xi} \approx \frac{1}{lb}\int_{-\infty}^{\infty}\frac{\partial U^{sys}}{\partial u}\frac{dw}{d\xi}dr = \int_{-\infty}^{\infty}(\tau_{app}+\tau_{dis})\lambda(r;\xi)\,dr\,. \tag{5.38}$$

According to the linear elasticity theory, since $\tau_{dis} \sim 1/r, \tau_{dis} = C/r$ where C is a constant is inserted into Eq. (5.38) and we assume that the dislocation is at origin, so $\xi = 0$. Then, Eq. (5.38) results in Eq. (5.39). Here, τ_{dis} term is disappeared because it is an odd function.

$$J_1 \approx \frac{b}{\sigma_D\sqrt{2\pi}}\int_{-\infty}^{\infty}\left(\tau_{app}+\frac{C}{r}\right)e^{-\frac{r^2}{2\sigma_D^2}}dr = \tau_{app}b\,. \tag{5.39}$$

Therefore, the first term of Eq. (5.36) is equal to PK force, F_{PK}, defined in the continuum theory. Unlike the first term, the second term of Eq. (5.36) includes phonon coordinates, v_n. From this, it can be inferred that the second term in Eq. (5.36) is generated because of interaction between the dislocation and phonons. That term is the main interest of this study and we defined it as F_{drag}. As a result, the *J*-integral around dynamic dislocation that interacts with phonons consists of two separated terms as

$$J = F_{PK} + F_{drag}\,, \tag{5.40}$$

where

$$F_{PK} = \tau_{app}b, \tag{5.41-1}$$

$$F_{drag} = -\frac{1}{l}\sum_{n=1}^{N}\frac{\partial U^{sys}}{\partial u_n}\left(\frac{d\lambda_n}{d\xi}\sum_{m=1}^{N}\lambda_m v_m + \lambda_n\sum_{m=1}^{N}\frac{d\lambda_m}{d\xi}v_m\right). \tag{5.41-2}$$

As an extreme example, if the dislocation does not move, the phonons are not generated from the dislocation core. As a result, v_n will be zero for every atom so the *J*-integral will be equal to F_{PK} as in the continuum theory. Thus, Eq. (5.40) reconfirms that the phonons are responsible to drag the moving defect[47,48,132].

In order to simplify Eq. (5.41-2), C in τ_{dis} needs to be analytically obtained by following process at first. Since it was proved that Eq. (5.38) is equal to PK force in continuum limit, *M*-integral can be defined in the discrete lattice in the same way. Based on the definition of *M* -integral in the continuum theory[133,134], M_1 with no drag effect can be simply derived in the continuum limit as

$$M_1 \approx \int_{-\infty}^{\infty} r(\tau_{app}+\tau_{dis})\lambda(r;\xi)\,dr = \int_{-\infty}^{\infty} r\left(\tau_{app}+\frac{C}{r}\right)\lambda(r;\xi)\,dr = Cb\,. \tag{5.42}$$

Here, τ_{app} term is disappeared since $r\lambda(r)$ is an odd function. According to the continuum theory, $M_1 = Gb^2/4\pi$, where G is shear modulus, in two-dimensional system. Therefore, $C = Gb/4\pi$ is obtained. Then, as we replace the discrete sums to integrals from $r=-R$ to $r=R$ in Eq. (5.41-2), F_{drag} becomes

$$\begin{aligned} -F_{drag} &= \frac{1}{l}\sum_{n=1}^{N}\frac{\partial U^{sys}}{\partial u_n}\left(\frac{d\lambda_n}{d\xi}\sum_{m=1}^{N}\lambda_m\upsilon_m + \lambda_n\sum_{m=1}^{N}\frac{d\lambda_m}{d\xi}\upsilon_m\right) \\ &= \frac{1}{l}\left[\left(\sum_n\frac{\partial U^{sys}}{\partial u_n}\frac{d\lambda_n}{d\xi}\right)\left(\sum_{m=1}^{N}\lambda_m\upsilon_m\right)+\left(\sum_n\frac{\partial U^{sys}}{\partial u_n}\lambda_n\right)\left(\sum_{m=1}^{N}\frac{d\lambda_m}{d\xi}\upsilon_m\right)\right] \\ &= \left[\int_{-R}^{R}\left(\tau_{app}+\frac{Gb}{4\pi r}\right)\frac{d\lambda}{d\xi}dr\cdot\frac{1}{b}\int_{-R}^{R}\lambda(r)\upsilon(r)\,dr\right]+\left[\int_{-R}^{R}\left(\tau_{app}+\frac{Gb}{4\pi r}\right)\lambda(r)\,dr\cdot\frac{1}{b}\int_{-R}^{R}\frac{d\lambda}{d\xi}\upsilon(r)\,dr\right]. \end{aligned} \tag{5.43}$$

If we insert $d\lambda/d\xi = \left(b/\sigma_D^3\sqrt{2\pi}\right)(r-\xi)\exp(-(r-\xi)^2/2\sigma_D^2)$ with $\xi=0$ into Eq. (5.43) and delete the odd terms, Eq. (5.43) is simplified to

$$F_{drag} = -\frac{b}{\sigma_D^3\sqrt{2\pi}}\left[\frac{Gb}{4\pi}\int_{-R}^{R}\upsilon(r)e^{-\frac{r^2}{2\sigma_D^2}}dr+\tau_{app}\int_{-R}^{R}r\upsilon(r)e^{-\frac{r^2}{2\sigma_D^2}}dr\right]. \tag{5.44}$$

If we restore the discreteness, then the drag force can be also represented as

$$F_{drag} = -\frac{b}{\sigma_D^3\sqrt{2\pi}}\left[\frac{Gb^2}{4\pi}\sum_{j=-R/b}^{R/b}\upsilon(j)e^{-\frac{(jb)^2}{2\sigma_D^2}}+\tau_{app}b^2\sum_{j=-R/b}^{R/b}j\upsilon(j)e^{-\frac{(jb)^2}{2\sigma_D^2}}\right]. \tag{5.45}$$

This is going to be used for numerical calculation of the drag force in Section 5.7. From the closed form of Eq. (5.44), we can infer two things. First, the phonons contribute to the drag force in two

ways by interacting with strain fields caused by the dislocation and external stress. Among them, the interactions near the dislocation core is mainly responsible to the drag force because the exponential terms in Eq. (5.44) decay rapidly as a distance deviates from the center of the core. Second, the drag force depends on the integration size, R. In other words, the existence of drag force makes *J*-integral be *path-dependent*.

5.5 Phonon coordinates

According to Eq. (5.44) (or Eq. (5.45)), the drag force can be calculated only after the phonon coordinates, $v(r)$ (or $v(j)$), are known. In general, a wave can be analyzed by decomposing it into elementary normal modes (called *eigenmodes*) depending on DOF of the system. In the same way, the phonon coordinate, or the oscillation displacement, can be decomposed into the finite number of eigenmodes, where all atoms oscillate with same frequency. Given that the phonon coordinate is expressed by a linear combination of the eigenmodes, understanding the contribution of each eigenmode to the drag force is our primary goal. In this section, we derive the phonon coordinate of each eigenmode by simplifying the dislocation as a localized defect based on method developed by Montroll and Potts[82] and investigate its influence on the drag force. They analyzed the oscillation of point defect by solving an eigenvalue problem. However, since the dislocation core width is an important factor to decide the drag force in this study, we extended their method to apply to the defect whose core has finite width.

In one-dimensional atomic chain where a defect is included, a displacement of *j*-th atom can be obtained by solving Eq. (5.46).

$$m\ddot{x}_j + \gamma\left[x_{j+1} - 2x_j + x_{j-1}\right] = Dx_j\,, \tag{5.46}$$

where m is an atomic mass, γ is a spring constant and D is an operator that characterized the defect, or dislocation. Under a plane wave assumption, $x_j = v(j)\exp(-i\omega t)$, Eq. (5.46) is changed to

$$Lv(j) = m\omega^2 v(j) + \gamma\left[v(j+1) - 2v(j) + v(j-1)\right]. \tag{5.47}$$

where $L = -D$. And we can express the RHS of Eq. (5.47) in matrix form with defining $w^{(i)}(j)$ as

$$L\upsilon(j) = m\omega^2\upsilon(j) + \gamma\left[\upsilon(j+1) - 2\upsilon(j) + \upsilon(j-1)\right] \equiv \sum_k w^{(k)}(k+j)\upsilon(k+j). \tag{5.48}$$

Prior to solve Eq. (5.48), it is convenient to define a function $g(j)$ that satisfies

$$Lg(x-s) = \gamma\delta(x-s) \tag{5.49}$$

Here, $g(j)$ is (lattice) Green's function. For arbitrary function, $f(s)$, if we multiply it to both sides of Eq. (5.49) and integrate over S, then Eq. (5.50) is derived.

$$f(x) = \frac{1}{\gamma}\int Lg(x-s)f(s)ds. \tag{5.50}$$

Therefore, if we want to solve the equation, $L\upsilon(j) = f(j)$, it can be alternatively expressed by

$$L\upsilon(j) = \frac{1}{\gamma}\int Lg(j-s)f(j)ds = L\left(\frac{1}{\gamma}\int g(j-s)f(j)ds\right). \tag{5.51}$$

As a result, we can obtain $\upsilon(j)$ as

$$\upsilon(j) = \frac{1}{\gamma}\int g(j-s)f(j)ds. \tag{5.52}$$

From Eq. (5.48) and Eq. (5.52),

$$\upsilon(j) = \gamma^{-1}\sum_m\sum_k g(j-m)w^{(k)}(k+m)\upsilon(k+m). \tag{5.53}$$

If $k+m$ is replaced by *l*, then $\upsilon(j)$ is derived as

$$\upsilon(j) = \gamma^{-1}\sum_m\sum_l g(j+k-l)w^{(k)}(l)\upsilon(l). \tag{5.54}$$

In order to define $g(j)$, let's express it in terms of Fourier transform as

$$g(j) = \frac{1}{2\pi}\int_{-\infty}^{\infty} G(\varphi)e^{-i\varphi j}\,d\varphi. \tag{5.55}$$

By inserting Eq. (5.55) into Eq. (5.47) and using Eq. (5.49), Eq. (5.56) is derived.

$$\gamma\delta(j) = \frac{1}{2\pi}\int_{-\infty}^{\infty} G(\varphi)\left[m\omega^2 + 2\gamma(\cos\varphi - 1)\right]e^{-i\varphi j}\,d\varphi. \tag{5.56}$$

Since $\delta(j) = (2\pi)^{-1}\int_{-\infty}^{\infty}\exp(-i\varphi j)\,d\varphi$,

$$G(\varphi) = \frac{\gamma}{m\omega^2 + 2\gamma(\cos\varphi - 1)}. \tag{5.57}$$

If we insert Eq. (5.57) into Eq. (5.55) and confine an integration range to the first Brillouin zone, the Green's function is derived as

$$g(j) = \frac{\gamma}{\pi}\int_0^{\pi} \frac{\cos\varphi j}{m\omega^2 + 2\gamma(\cos\varphi - 1)} d\varphi. \tag{5.58}$$

Depending on the frequency, ω, the integrand of Eq. (5.58) has either poles or not. In perfect lattice system without any defects, the maximum reachable frequency, ω_L, is $2\sqrt{\gamma/m}$. If $\omega \leq \omega_L$, the integrand has poles but if $\omega > \omega_L$, it does not have poles. In this work, we only consider the latter. In this case, the newly generated frequency bands by embedding the dislocation are localized around the dislocation core atoms. Therefore, $v(j) \to 0$ as $j \to \pm\infty$. In general, this occurs when the drag force is governed by the fluttering mechanism due to thermal oscillation[56] or the inertial oscillation coming from the extremely fast speed of dislocation[33,76]. If we define $f \equiv \omega/\omega_L \equiv \cosh(z/2)$ and assume that $f > 1$, then Eq. (5.58) is changed to

$$g(j) = \frac{1}{2\pi}\int_0^{\pi} \frac{\cos\varphi j}{\cos\varphi + \cosh z} d\varphi. \tag{5.59}$$

Since $\cosh z > 1$, the integrand does not have poles. According to Montroll and Potts[82], the Eq. (5.59) is finally derived as

$$g(j) = \frac{(-1)^j}{2\sinh z} e^{-|j|z}. \tag{5.60}$$

Since the dislocation core is localized, it is reasonable to assume that index l in Eq. (5.54) only includes atoms in the core rather than in whole system. Then, Eq. (5.54) can be expressed by matrix form as

$$\mathbf{v} = \mathbf{G}\mathbf{v}. \tag{5.61}$$

If we define an eigenvectors and eigenvalue of $\mathbf{G}$ in mode μ as $\mathbf{\Psi}^{\mu}$ and β^{μ}, respectively, then

$$\mathbf{G}\psi^{\mu} = \beta^{\mu}\psi^{\mu} \tag{5.62}$$

is satisfied. And if we express $\mathbf{v}$ in terms of basis $\mathbf{\Psi}^{\mu}$ as $\mathbf{v} = \sum_{\mu} v^{\mu}\mathbf{\Psi}^{\mu}$, then Eq. (5.61) is changed to $\sum_{\mu} v^{\mu}(1 - \beta^{\mu})\mathbf{\Psi}^{\mu} = 0$. For Eq. (5.61) to have solutions, $\beta^{\mu} = 1$ must be satisfied

for all eigenmodes, μ.

As shown in Fig. 5.5, we assume that the center of the core is at the origin and $2\sigma_G + 1$ atoms are *geometrically* defined as the dislocation core. The core atoms have mass m' and are connected by a spring whose constant is γ', but others have mass m and are connected by γ. Then, the equations of motion follows

$$\begin{aligned}
&\text{(i)}\ \ L\upsilon(j) = (m-m')\omega^2 u(j) + (\gamma-\gamma')\left[\upsilon(j+1) - 2\upsilon(j) + \upsilon(j-1)\right] \quad (-\sigma_G \le j \le \sigma_G) \\
&\text{(ii)}\ \ L\upsilon(\sigma_G+1) = (\gamma'-\gamma)\left[\upsilon(\sigma_G+1) - \upsilon(\sigma_G)\right] \\
&\text{(iii)}\ \ L\upsilon(-\sigma_G-1) = (\gamma-\gamma')\left[\upsilon(-\sigma_G) - \upsilon(-\sigma_G-1)\right]
\end{aligned} \tag{5.63}$$

By comparing Eq. (5.63) with Eq. (5.48), following relations are obtained that

$$\begin{aligned}
&\text{(i)}\ \ w^{(-1)}(j-1) = w^{(1)}(j+1) = \gamma-\gamma',\ w^{(0)}(j) = (m-m')\omega^2 - 2(\gamma-\gamma') \quad (-\sigma_G \le j \le -\sigma_G) \\
&\text{(ii)}\ \ w^{(-1)}(\sigma_G) = \gamma-\gamma',\ w^{(0)}(\sigma_G+1) = \gamma'-\gamma \\
&\text{(iii)}\ \ w^{(-1)}(-\sigma_G-1) = \gamma'-\gamma,\ w^{(0)}(-\sigma_G) = \gamma-\gamma'
\end{aligned} \tag{5.64}$$

As the relations (5.64) are inserted into Eq. (5.54), Eq. (5.65) is derived.

$$\begin{aligned}
\upsilon(j) = \gamma^{-1}\sum_k \Big[& g(j+k+\sigma_G+1)w^{(k)}(-\sigma_G-1)\upsilon(-\sigma_G-1) + g(j+k+\sigma_G)w^{(k)}(-\sigma_G)\upsilon(-\sigma_G) \\
& + \cdots + g(j+k-\sigma_G)w^{(k)}(\sigma_G)\upsilon(\sigma_G) + g(j+k-\sigma_G-1)w^{(k)}(\sigma_G+1)\upsilon(\sigma_G+1)\Big] \\
= \gamma^{-1}\big[& (\gamma-\gamma')g(j+\sigma_G) + (\gamma-\gamma')g(j+\sigma_G+1)\big]\upsilon(-\sigma_G-1) \\
& + \gamma^{-1}\Big[(\gamma-\gamma')g(j+\sigma_G-1) + \big\{(m-m')\omega^2 - 2(\gamma-\gamma')\big\}g(j+\sigma_G) + (\gamma-\gamma')g(j+\sigma_G+1)\Big]\upsilon(-\sigma_G) \\
& + \cdots\gamma^{-1}\Big[(\gamma-\gamma')g(j-\sigma_G-1) + \big\{(m-m')\omega^2 - 2(\gamma-\gamma')\big\}g(j-\sigma_G) + (\gamma-\gamma')g(j-\sigma_G+1)\Big]\upsilon(\sigma_G) \\
& + \gamma^{-1}\big[(\gamma'-\gamma)g(j-\sigma_G-1) + (\gamma-\gamma')g(j-\sigma_G)\big]\upsilon(\sigma_G+1).
\end{aligned} \tag{5.65}$$

If we define $P \equiv \gamma'/\gamma$ and $Q \equiv m'/m$, then Eq. (5.66) is obtained.

$$\gamma^{-1}\left[(m-m')\omega^2 - 2(\gamma-\gamma')\right] = 4f^2(1-Q) - 2(1-P). \tag{5.66}$$

Then, Eq. (5.65) is simplified to

$$\begin{aligned}\upsilon(j) &= (1-P)\left[g(j+\sigma_G)-g(j+\sigma_G+1)\right]\upsilon(-\sigma_G-1)\\ &\quad+(1-P)\left[g(j-\sigma_G)-g(j-\sigma_G-1)\right]\upsilon(\sigma_G+1)\\ &\quad+\sum_{n=-\sigma_G}^{\sigma_G}\left[(1-P)\left\{g(j-n-1)+g(j-n+1)\right\}+\left\{4f^2(1-Q)-2(1-P)\right\}g(j-n)\right]\upsilon(n)\end{aligned} \tag{5.67}$$

Here, the Σ term that represents a displacement inside the core should be carefully considered because of the characteristic of Green's function. As Green's function is inserted to Eq. (5.47),

$$\begin{aligned}Lg(j) &= m\omega^2 g(j)+\gamma\left[g(j+1)-2g(j)+g(j-1)\right]\\ &= \gamma\left[4f^2 g(j)+\left\{g(j+1)-2g(j)+g(j-1)\right\}\right].\end{aligned} \tag{5.68}$$

is derived. And by using Eq. (5.49),

$$g(j+1)-2g(j)+g(j-1)=-4f^2 g(j) \tag{5.69}$$

for $j \neq 0$ is satisfied and

$$4f^2 g(0)+g(1)-2g(0)+g(-1)=1 \tag{5.70}$$

is satisfied for $j = 0$. Then, the Σ term in Eq. (5.67) follows

$$\begin{aligned}&(1-P)\left\{g(j-n-1)+g(j-n+1)\right\}+\left\{4f^2(1-Q)-2(1-P)\right\}g(j-n)\\ &=(1-P)\left[g(j-n-1)-2g(j-n)+g(j-n+1)\right]+4f^2(1-Q)g(j-n)\\ &=-4f^2(1-P)g(j-n)+4f^2(1-Q)g(j-n)\\ &=4f^2(P-Q)g(j-n)\end{aligned} \tag{5.71-1}$$

when $j \neq n$ and

$$\begin{aligned}&(1-P)\left\{g(j-n-1)+g(j-n+1)\right\}+\left\{4f^2(1-Q)-2(1-P)\right\}g(j-n)\\ &=(1-P)\left[g(j-n-1)-2g(j-n)+g(j-n+1)\right]+4f^2(1-Q)g(j-n)\\ &=(1-P)\left[g(-1)-2g(0)+g(1)\right]+4f^2(1-Q)g(0)\\ &=4f^2(P-Q)g(0)+(1-P)\end{aligned} \tag{5.71-2}$$

when $j = n$. As a result, Eq. (5.67) becomes

$$\begin{aligned}\upsilon(j) &= (1-P)\left[g(j+\sigma_G)-g(j+\sigma_G+1)\right]\upsilon(-\sigma_G-1)\\ &\quad+(1-P)\left[g(j-\sigma_G)-g(j-\sigma_G-1)\right]\upsilon(\sigma_G+1)+4f^2(P-Q)\sum_{m=-\sigma_G}^{\sigma_G}g(j-m)\upsilon(m)\end{aligned} \tag{5.72-1}$$

when $j < -\sigma_G$ or $j > \sigma_G$ and it represents the phonon coordinate *outside* of the core. And Eq. (5.67) becomes

$$\begin{aligned}\upsilon(j) &= (1-P)\left[g(j+\sigma_G) - g(j+\sigma_G+1)\right]\upsilon(-\sigma_G-1) \\ &+ (1-P)\left[g(j-\sigma_G) - g(j-\sigma_G-1)\right]\upsilon(\sigma_G+1) + 4f^2(P-Q)\sum_{\substack{m=-\sigma_G \\ (m\neq j)}}^{\sigma_G} g(j-m)\upsilon(m) \\ &+ \left[4f^2(P-Q)g(0) + (1-P)\right]\upsilon(j)\end{aligned}$$

(5.72-2)

when $-\sigma_G \le j \le \sigma_G$ and thus it is the phonon coordinate *inside* the core. Now, Eq. (5.72-1) and Eq. (5.72-2) can be expressed by a matrix equation in the form of Eq. (5.61) with using the relation $g(-j) = g(j)$. Then, Eq. (5.73) is derived. Here, we assume that the atoms in dislocation core still have same mass with them in perfect region so we set $Q = 1$.

$$\begin{bmatrix}\upsilon(-\sigma_G-1)\\ \upsilon(-\sigma_G)\\ \vdots\\ \upsilon(\sigma_G)\\ \upsilon(\sigma_G+1)\end{bmatrix} = \begin{bmatrix}(1-P)\left[g(1)-g(0)\right] & 4f^2(P-1)g(1) & \cdots\\ (1-P)\left[g(0)-g(1)\right] & 4f^2(P-1)g(0)+(1-P) & \\ \vdots & \vdots & \ddots\\ (1-P)\left[g(2\sigma_G)-g(2\sigma_G+1)\right] & 4f^2(P-1)g(2\sigma_G) & \\ (1-P)\left[g(2\sigma_G+1)-g(2\sigma_G+2)\right] & 4f^2(P-1)g(2\sigma_G+1) & \cdots\end{bmatrix}$$

$$\begin{bmatrix}4f^2(P-1)g(2\sigma_G+1) & (1-P)\left[g(2\sigma_G+1)-g(2\sigma_G+2)\right]\\ 4f^2(P-1)g(2\sigma_G) & (1-P)\left[g(2\sigma_G)-g(2\sigma_G+1)\right]\\ \vdots & \vdots\\ 4f^2(P-1)g(0)+(1-P) & (1-P)\left[g(0)-g(1)\right]\\ 4f^2(P-1)g(1) & (1-P)\left[g(1)-g(0)\right]\end{bmatrix}\begin{bmatrix}\upsilon(-\sigma_G-1)\\ \upsilon(-\sigma_G)\\ \vdots\\ \upsilon(\sigma_G)\\ \upsilon(\sigma_G+1)\end{bmatrix}$$

(5.73)

In Eq. (5.73), the size of $\mathbf{G}$ matrix is $(2\sigma_G+3)\times(2\sigma_G+3)$ so it has $(2\sigma_G+3)$ eigenmodes. Thus, the number of oscillation eigenmodes depends on the size of dislocation core. In other words, as the size of dislocation core increases, the system can have more various oscillation modes although the size of system does not change.

The eigenvalues and eigvenvectors of $\mathbf{G}$ are numerically obtained in following section. However, without solving the exact eigenvalue problems, Eq. (5.72-1) and (5.72-2) can be further simplified due to the symmetric and anti-symmetric properties of the eigenmodes. According to

the proof introduced in Appendix E, $(2\sigma_G + 3)$ eigenmodes are classified to two types except a single rigid mode. As a result, $(\sigma_G + 1)$ modes correspond to symmetric mode and remaining $(\sigma_G + 1)$ modes correspond to anti-symmetric mode. The one rigid mode has zero eigenvalue and it does not contribute to the oscillation. This is proved in Appendix F. Thus, it is ignored in this study. For the anti-symmetric and symmetric modes, their eigenvectors can be described by

$$\psi^{\mu,a} = \left[-a_{\sigma_G+1} - a_{\sigma_G} \cdots 0 \cdots a_{\sigma_G}\ a_{\sigma_G+1}\right]^T, \tag{5.74}$$

$$\psi^{\mu,s} = \left[s_{\sigma_G+1}\ s_{\sigma_G} \cdots s_0 \cdots s_{\sigma_G}\ s_{\sigma_G+1}\right]^T, \tag{5.75}$$

respectively. And both Eq. (5.74) and Eq. (5.75) are normalized, or $|\Psi^{\mu,a}| = |\Psi^{\mu,s}| = 1$. Physically, the eigenvector in mode μ means an array of normalized phonon coordinates of the core atoms in $[-\sigma_G - 1, \sigma_G + 1]$ in the corresponding mode because Eq. (5.61) has a solution only when an eigenvalue of $\mathbf{G}$ is equal to 1. Thus, $\boldsymbol{\upsilon^{\mu}} = \mathbf{G}\boldsymbol{\Psi^{\mu}} = \boldsymbol{\Psi^{\mu}}$ for the core atoms in $[-\sigma_G - 1, \sigma_G + 1]$. And according to Eq. (72-1), a phonon coordinate of atom outside the dislocation core can be described as a linear combination of phonon coordinates of the core atoms. As a result, the phonon coordinates in mode μ for $j > \sigma_G + 1$ can be derived by inserting Eq. (5.74) and Eq. (5.75) into Eq. (5.72-1) depending on the characteristic of each eigenmode. As a result,

$$\begin{aligned}\frac{\upsilon^{\mu,a}(j)}{\upsilon_0^{\mu,a}} &= (1-P)\frac{(-1)^{j+\sigma_G}}{2\sinh z}\left(1+e^{-z}\right)\left(-e^{-(j+\sigma_G)z} + e^{-(j-\sigma_G-1)z}\right)a_{\sigma_G+1} \\ &\quad - 4f^2(1-P)\left[\sum_{n=1}^{\sigma_G}\frac{(-1)^{j-n}}{2\sinh z}e^{-(j-n)z}a_n + \sum_{n=-\sigma_G}^{-1}\frac{(-1)^{j-n}}{2\sinh z}e^{-(j-n)z}a_n\right],\end{aligned} \tag{5.76}$$

where $\upsilon_0^{\mu,a}$ is a magnitude coefficient of anti-symmetric mode μ, is derived for anti-symmetric mode and

$$\begin{aligned}\frac{\upsilon^{\mu,s}(j)}{\upsilon_0^{\mu,s}} &= (1-P)\frac{(-1)^{j+\sigma_G}}{2\sinh z}\left(1+e^{-z}\right)\left(e^{-(j+\sigma_G)z} + e^{-(j-\sigma_G-1)z}\right)s_{\sigma_G+1} \\ &\quad - 4f^2(1-P)\frac{(-1)^{j}}{2\sinh z}\left[\sum_{n=1}^{\sigma_G}(-1)^n\left(e^{-(j-n)z} + e^{-(j+n)z}\right)s_n + e^{-jz}s_0\right]\end{aligned} \tag{5.77}$$

where $\upsilon_0^{\mu,s}$ is a magnitude coefficient of symmetric mode μ, is derived for symmetric mode. Both Eq. (5.76) and Eq. (5.77) are further simplified to

$$\frac{\upsilon^{\mu,a}(j)}{\upsilon_0^{\mu,a}} = \frac{2f(P-1)}{\sinh z}(-1)^j e^{-jz}\left[2f\sum_{n=1}^{\sigma_G}(-1)^n \sinh(nz)\,a_n - (-1)^{\sigma_G}\sinh\left(\sigma_G+\frac{1}{2}\right)z\,a_{\sigma_G+1}\right], \tag{5.78}$$

$$\frac{\upsilon^{\mu,s}(j)}{\upsilon_0^{\mu,s}} = \frac{2f(P-1)}{\sinh z}(-1)^j e^{-jz}\left[2f\sum_{n=1}^{\sigma_G}(-1)^n \cosh(nz)\,s_n + fs_0 - (-1)^{\sigma_G}\cosh\left(\sigma_G+\frac{1}{2}\right)z\,s_{\sigma_G+1}\right], \tag{5.79}$$

respectively. And through the same procedure used to derive Eq. (5.78) to Eq. (5.79), we obtain $\upsilon_0^{\mu,a}(j) = -\upsilon_0^{\mu,a}(-j)$ and $\upsilon_0^{\mu,s}(j) = \upsilon_0^{\mu,s}(-j)$ for $j < -\sigma_G - 1$.

5.6 Drag force

Since we derived phonon coordinates for both anti-symmetric and symmetric modes in the preceding section, now we can derive a phonon drag force. Both Eq. (5.78) and Eq. (5.79) can be described as a function of distance $r = jb$ like

$$\upsilon^{\mu,a}(r) = V_0^{\mu,a}(\sigma_G, z)e^{-\frac{z}{b}r},\ \upsilon^{\mu,a}(-r) = -\upsilon^{\mu,a}(r), \tag{5.80}$$

$$\upsilon^{\mu,s}(r) = V_0^{\mu,s}(\sigma_G, z)e^{-\frac{z}{b}r},\ \upsilon^{\mu,s}(-r) = \upsilon^{\mu,s}(r) \tag{5.81}$$

for anti-symmetric and symmetric modes, respectively. And their coefficients depend on geometric parameters of the dislocation core. By inserting Eq. (5.80) and Eq. (5.81) into Eq. (5.44), the drag forces in mode μ are derived as Eq. (5.82) and Eq. (5.83) for anti-symmetric and symmetric modes, respectively

$$F_{drag}^{\mu,a} = -\frac{b\tau_{app}}{\sigma_D^3\sqrt{2\pi}}\int_{-R}^{R} r\,\upsilon(r)e^{-\frac{r^2}{2\sigma_D^2}}dr, \tag{5.82}$$

$$F_{drag}^{\mu,s} = -\frac{Gb^2}{\sigma_D^3 4\pi\sqrt{2\pi}}\int_{-R}^{R} \upsilon(r)e^{-\frac{r^2}{2\sigma_D^2}}dr. \tag{5.83}$$

By using integration by parts, an integral term in Eq. (5.82) becomes

$$
\begin{aligned}
&\int_{-R}^{R} r\,\upsilon(r)\, e^{-\frac{r^2}{2\sigma_D^2}}\, dr \\
&= 2V_0^{\mu,a}\int_{0}^{R} r\, e^{-\frac{r^2}{2\sigma_D^2}}\cdot e^{-\frac{zr}{b}}\, dr \\
&= 2V_0^{\mu,a}\left[\sigma_D^2\left(1-e^{-\left(\frac{R^2}{2\sigma_D^2}+\frac{zR}{b}\right)}\right)-\frac{\sigma_D^2 z}{b}\int_{0}^{R} e^{-\left(\frac{r^2}{2\sigma_D^2}+\frac{zr}{b}\right)}\, dr\right] \\
&= 2V_0^{\mu,a}\left[\sigma_D^2\left(1-e^{-\left(\frac{R^2}{2\sigma_D^2}+\frac{zR}{b}\right)}\right)-\frac{\sigma_D^2 z}{b}e^{\frac{\sigma_D^2 z^2}{2b^2}}\int_{0}^{R} e^{-\left[\frac{1}{\sqrt{\sigma_D}}\left(r+\frac{\sigma_D^2 z}{b}\right)\right]^2}\, dr\right] \\
&= 2V_0^{\mu,a}\left[\sigma_D^2\left(1-e^{-\left(\frac{R^2}{2\sigma_D^2}+\frac{zR}{b}\right)}\right)-\sqrt{\frac{\pi}{2}}\frac{\sigma_D^3 z}{b}e^{\frac{\sigma_D^2 z^2}{2b^2}}\left[erf\left(t_R\right)-erf\left(t_0\right)\right]\right]
\end{aligned}
\tag{5.84}
$$

where

$$t_0=\frac{\sigma_D z}{\sqrt{2}b}, \tag{5.85-1}$$

$$t_R=\frac{1}{\sqrt{2}\sigma_D}\left(R+\frac{\sigma_D^2 z}{b}\right). \tag{5.85-2}$$

Thus, by inserting Eq. (5.84) into Eq. (5.82), then the drag force for anti-symmetric mode is finally derived as Eq. (5.86).

$$F_{drag}^{\mu,a}=-\tau_{app}V_0^{\mu,a}(\sigma_G,z)\left[\sqrt{\frac{2}{\pi}}\frac{b}{\sigma_D}\left(1-e^{-\left(\frac{R^2}{2\sigma_D^2}+\frac{zR}{b}\right)}\right)-ze^{\frac{\sigma_D^2 z^2}{2b^2}}\left(erf\left(t_R\right)-erf\left(t_0\right)\right)\right]. \tag{5.86}$$

And the integral term in Eq. (5.83) follows

$$
\begin{aligned}
&\int_{-R}^{R}\upsilon(r)\, e^{-\frac{r^2}{2\sigma_D^2}}\, dr \\
&= 2V_0^{\mu,s}\int_{0}^{R} e^{-\frac{r^2}{2\sigma_D^2}}\cdot e^{-\frac{zr}{b}}\, dr=\sqrt{2\pi}V_0^{\mu,s}\sigma_D e^{\frac{\sigma_D^2 z^2}{2b^2}}\left(erf\left(t_R\right)-erf\left(t_0\right)\right)
\end{aligned}
\tag{5.87}
$$

If we insert Eq. (5.87) into Eq. (5.83), then the drag force for symmetric mode is finally derived as

$$F_{drag}^{\mu,s} = -\frac{GV_0^{\mu,s}(\sigma_G, z)}{4\pi}\left(\frac{b}{\sigma_D}\right)^2 e^{\frac{\sigma_D^2 z^2}{2b^2}}\left(erf(t_R) - erf(t_0)\right). \tag{5.88}$$

From Eq. (5.86) and Eq. (5.88), we can conclude that the anti-symmetric phonon modes only interact with external strain field and but the symmetric modes only interact with self-strain field caused by a dislocation. Furthermore, both equations show that the drag force is a function of integration radius and therefore it makes *J*-integral *path-dependent* unless the radius is large enough.

According to Eq. (5.86) and Eq. (5.88), the drag force for both eigenmodes depends on geometric and mechanical properties of the dislocation core. For example, as $P \to 1$, which means that the core atoms are replaced by perfect atoms, both $V_0^{\mu,a}(\sigma_G, z)$ and $V_0^{\mu,s}(\sigma_G, z)$ become zero so that the drag force disappears. Meanwhile, the drag force of mode μ, which is integrated along a large enough path, will increase with increasing *P* because $V_0^{\mu,a}$ (or $V_0^{\mu,s}$) increases. This means that the more energy dissipates from the dislocation core as it becomes stiffer because the stiffer core makes its oscillation frequency be higher.

5.7 Numerical results

In preceding section, we analytically derived the drag force for anti-symmetric and symmetric eigenmodes. In this section, we numerically solve Eq. (5.73) to obtain eigenvectors and use them to calculate the drag force through Eq. (5.45).

5.7.1 Eigenmode analysis

Among $2\sigma_G + 2$ eigenvalues of $\mathbf{G}$ except $\beta = 0$ that corresponds to the rigid mode, $\sigma_G + 1$ eigenvalues are for the anti-symmetric modes and $\sigma_G + 1$ eigenvalues are for the symmetric modes. However, in order for Eq. (5.73) to have solutions, it is necessary to find f^μ and P^μ that make $\beta^\mu = 1$ at first. This constraint makes both f^μ and P^μ are uniquely related. After finding the f^μ and P^μ, then corresponding eigenvector, Ψ^μ, is obtained. The algorithm to find f^μ, P^μ and Ψ^μ is summarized in Fig. 5.6. And a validity of numerical solution obtained by the algorithm is proved by comparing it with an analytic solution derived for $\sigma_G = 0$ by Montroll and Potts[82]. According to their work, the relation between f^μ and P^μ for an anti-symmetric mode is analytically derived as

$$f = \frac{P}{\sqrt{4(P-1)}}. \tag{5.89}$$

And the relation for a symmetric mode follows

$$\sqrt{\frac{f^2}{f^2-1}} = 1 + \frac{P}{2(P-1)f^2}. \tag{5.90-1}$$

Here, Eq. (5.90) is simplified to Eq. (5.91).

$$f = \sqrt{\frac{P(3P-4) + P\sqrt{P(9P-8)}}{8(P-1)}}. \tag{5.90-2}$$

The comparisons between our numerical solutions and analytic solutions for $\sigma_G = 0$ are graphically shown in Fig. 5.7. According to the Fig. 5.7, our numerical algorithm exactly reproduced the analytic solutions for both eigenmodes.

Now we applied the numerical method to solve Eq. (73) for $\sigma_G > 0$ cases, or when the dislocation core has finite width, and find relations between f^μ and P^μ. The relations between f^μ and P^μ for $\sigma_G = 1, 2$ and 3 are graphically described in Fig. 5.8a, 5.8b and 5.8c, respectively. And their normalized eigenvectors are drawn in Figs 5.9, 5.10 and 5.11, respectively.

According to Figs. 5.8a, 5.8b and 5.8c, the number of *activated* eigenmodes depends on P^μ. As an example, for $\sigma_G = 1$, only single symmetric mode is activated when $1.0 < P^\mu < 1.3$, and one symmetric and one anti-symmetric modes are activated when $1.3 \leq P^\mu < 2.2$. After then, two symmetric and one anti-symmetric modes are activated when $1.3 \leq P^\mu < 7.3$. Finally, all possible eigenmodes are activated only when $P^\mu \geq 7.3$. This is equally applied to for $\sigma_G = 2, 3$ and even larger values. This difference in eigenmode activation is due to a difference of P^μ that satisfies $\beta^\mu = 1$ for each mode. In Fig. 5.8a, 5.8b, and 5.8c, P^μ required to activate the next eigenmode drastically increases as the number of currently-activated modes increases and the newly generated mode occupies lowest frequency, or the lowest energy level. And notice that the symmetric and anti-symmetric modes are alternatively activated. However, since the symmetric mode is always generated at first, the number of symmetric modes is always greater than or equal to it of anti-symmetric modes.

From the eigenvectors of each mode described in from Fig.9 to Fig. 11, additional information can be obtained. For $\sigma_G = 1$, when the symmetric eigenvectors in Fig. 5.9a and 5.9c are

compared, the latter has smaller frequency but larger absolute value at edge elements than the former. The same tendency is found when anti-symmetric eigenvectors in Fig. 5.9b and 5.9d are compared. For $\sigma_G = 2$, when the symmetric eigenvectors in Figs. 5.10a, 5.10c and 5.10e are compared, the distribution of Fig. 5.10a is the most centralized but it of Fig. 5.10e is largely localized at edge atoms, or at atoms whose numbers are ± 3. And as the anti-symmetric eigenvector changes from Fig. 5.10b to Fig. 5.10f, its distribution becomes more localized at edge atoms as the symmetric mode does. The same tendency is found for both symmetric and anti-symmetric modes in Fig. 5.11. This proves that the frequency of eigenmode increases as the element distribution of its eigenvector within the core be more concentrated at its center.

5.7.2 Drag force analysis

A contribution of each eigenmode to the drag force was investigated with changing the core properties. First, phonon coordinates were separately calculated for core atoms and atoms outside the core. The phonon coordinates of core atoms, or atom j for $j \in [-\sigma_G - 1, \sigma_G + 1]$, correspond to the elements of eigenvector in mode μ. And phonon coordinates of atoms outside the core in the same mode were obtained by using Eq. (5.78) and Eq. (5.79). After then, the drag force was numerically calculated by inserting the obtained phonon coordinates into Eq. (5.45). To calculate the drag force, $G = 71.5$ GPa and $b = 2.473$ Å are used as input parameters. These parameters are of bulk α-iron calculated at absolute zero. Additionally, we assumed $\sigma_D = \sigma_G b$ for simplicity. In this work, the resulting drag force was normalized by $\tau_{app} v_0^{\mu}$, where $v_0^{\mu} = v_0^{\mu,a}$ for anti-symmetric modes and $v_0^{\mu} = v_0^{\mu,s}$ for symmetric modes. The normalized drag forces as a function of P for $\sigma_G = 1, 2$ and 3 are shown in Figs. 5.12, 5.13 and 5.14, respectively. Since the drag force depends on R, it was calculated with changing R. As a result, according to Fig. 5.12, the magnitude of drag force increases with increasing P and finally converges to a certain value for every mode. In particular, the subsequently-activated (SA) symmetric and anti-symmetric modes cause much larger drag force than formerly-activated (FA) symmetric and anti-symmetric modes, respectively. The same tendency was observed in Figs 5.13b and 5.14b when R is large enough. This can be intuitively explained by investigating a dependency of the analytically-derived drag force on eigenmode frequency. According to Eq. (5.86) and Eq. (5.88), if $R = N_R b$ is large enough to surround all core atoms with extra space, or $N_R \gg \sigma_G$, the drag forces for anti-symmetric and symmetric modes approximately become

$$\left|F_{drag}^{\mu,a}\right| \approx \tau_{app} V_0^{\mu,a} \left[\sqrt{\frac{2}{\pi}} \frac{b}{\sigma_D} - ze^{\frac{\sigma_D^2 z^2}{2b^2}} \left(1 - erf\left(t_0\right)\right) \right], \tag{5.91}$$

$$\left|F_{drag}^{\mu,s}\right| \approx \frac{G}{4\pi} V_0^{\mu,s} \left(\frac{b}{\sigma_D} \right)^2 e^{\frac{\sigma_D^2 z^2}{2b^2}} \left(1 - erf\left(t_0\right)\right). \tag{5.92}$$

Since SA mode has much lower frequency than FA mode at fixed P, it has much smaller z.

For anti-symmetric modes, since Eq. (5.91) decreases with increasing z, the drag force is larger for the FA mode than for the SA mode. In particular, if z is so large that $t_0 > 2$, the second term in Eq. (5.91) is extremely small compared to the first term. Therefore, the drag force follows

$$\left|F_{drag}^{\mu,a}\right| \approx \tau_{app} V_0^{\mu,a}(\sigma_G, z) \sqrt{\frac{2}{\pi}} \frac{b}{\sigma_D} \tag{5.93}$$

and its dependence on frequency is determined by $V_0^{\mu,a}(\sigma_G, z)$. By inserting Eq. (5.78) into Eq. (5.93),

$$\left| \frac{F_{drag}^{\mu,a}}{\tau_{app} \upsilon_0^{\mu,a}} \right| \sim \frac{2f}{\sinh z} \left[2f \sum_n \sinh(nz)\, a_n \right] \sim \frac{2f}{2f\sqrt{f^2 - 1}} \left[2f \sum_n \sinh(nz)\, a_n \right] \sim \sum_n \sinh(nz)\, a_n \tag{5.94}$$

is derived. Since edge atoms of the dislocation core in SA mode has larger eigenvector elements than them in FA mode, the drag force is much larger for the SA mode than the FA mode. For symmetric mode, since $\exp(\sigma_D^2 z^2 / 2b^2)(1 - \mathrm{erf}(t_0))$ in Eq. (5.92) is a decreasing function of z and the same edge-localized effect occurs as in the anti-symmetric method , the drag force is much larger for the SA mode than the FA mode.

Interestingly, when R is so small that it includes only the core atoms with few extra atoms, a decrease of the drag force was observed in Figs. 5.13a and 5.14a with increasing P at small P. Since R is so small, the drag force for both anti-symmetric and symmetric modes is mainly determined by eigenvectors of the core. According to Fig. 15, it was observed that a distribution of eigenvector elements becomes centralized as P increases at fixed eigenmode. This leads $V_0^{\mu,a}(\sigma_G, z)$ and $V_0^{\mu,s}(\sigma_G, z)$ to decrease as P increases and finally results in decrease of the drag force. As a result, a distribution of eigenvector elements within the dislocation core is a crucial to explain the contribution of each mode to drag force. At large P, however, the variation of eigenvector distribution is not large with changing P. Rather, $V_0^{\mu,a}(\sigma_G, z)$ and $V_0^{\mu,s}(\sigma_G, z)$

increase with increasing P because they are proportional to $P-1$ by Eq. (5.78) and Eq. (5.79).

In addition, we investigated a dependency of the drag force on the core width for both anti-symmetric and symmetric modes. By using Eq. (5.91) and Eq. (5.92) with $z=1.0$, the relationship between the drag force and the core width can be computed. This is shown in Fig. 5.16. As a result, the magnitude of drag force decreased as the core width increased. In other words, larger drag force is induced during the dislocation motion as it has more compact structure. Furthermore, our result is qualitatively supported by Chapter 3 and can be connected with them in the limit of high dislocation frequency. According to the Chapter 3, we proved that the dislocation oscillation during its gliding motion dissipates energy around its core and the dissipation lowers the average stress around the moving dislocation. This is the source of drag force and it is quantified by Eq. (5.95) based on discrete lattice dynamics.

$$\left|\frac{F_{drag}}{F_{app}}\right| = C_1^{dis} - \left(\frac{\omega_L b}{2\pi v}\right)^2 C_2^{dis}, \tag{5.95}$$

where F_{app} is externally applied force and v is the dislocation velocity. Here, C_1^{dis} and C_2^{dis} are defined by

$$C_1^{dis} = \frac{2B\Phi_{dis}}{\pi^2 m\omega}, \tag{5.96-1}$$

$$C_2^{dis} = \frac{B\Phi_{dis}\omega}{m\omega_L^2}, \tag{5.96-2}$$

where B is a drag coefficient. And it was proved that Φ_{dis} is a dimensionless constant that is proportional to the compactness of dislocation core.

In the limit of high dislocation frequency, the dislocation velocity becomes high enough to satisfy $w_L b \ll 2\pi v$. As a result, Eq. (5.95) is simplified to $\left|F_{drag}/F_{app}\right| \approx C_1^{dis}$. Therefore, increasing Φ_{dis} leads F_{drag} to increase, which is the same result of this work. And in our model, the anti-symmetric mode mainly contributes to the drag force in the limit of high frequency because $\mathrm{erf}(t_0) \to 1$ by Eq. (5.91). As a result, Eq. (5.97) is satisfied.

$$\left|\frac{F_{drag}}{F_{app}}\right| = \left|\frac{F_{drag}}{\tau_{app} b}\right| \approx \sqrt{\frac{2}{\pi}}\frac{V_0^{\mu,a}}{\sigma_D}. \tag{5.97}$$

Since $\left|F_{drag}/F_{app}\right| \approx C_1^{dis}$, we can derive C_1^{dis} as

$$C_1^{dis} = \sqrt{\frac{2}{\pi}} \frac{V_0^{\mu,a}(\sigma_G, z)}{\sigma_D}$$
$$\sim \sqrt{\frac{2}{\pi}} \left(\frac{b}{\sigma_D} \right) \frac{2f(P-1)}{\sinh z} \left[2f \sum_{n=1}^{\sigma_G} (-1)^n \sinh(nz) a_n - (-1)^{\sigma_G} \sinh\left(\sigma_G + \frac{1}{2} \right) z a_{\sigma_G+1} \right]. \quad (5.98)$$

Therefore, we can conclude that the drag force occurs mainly by the anti-symmetric oscillation mode when the dislocation velocity is high enough to be comparable to the sound wave velocity. And the drag force is quantified by Eq. (5.98) where structural and mechanical properties of the dislocation core are well reflected.

5.8 Summary

Based on discrete lattice dynamics theory, we analytically derived configurational drag force for each eigenmode by adopting dislocation-phonon coordinates. The drag force was responsible to path-dependency of *J*-integral around moving dislocation and it was generated by localized oscillation of the dislocation. By assuming the dislocation core as an isolated defect that has finite core width, the oscillation was simply classified into symmetric and anti-symmetric modes. The symmetric modes only interacted with the dislocation's self-stress field but the anti-symmetric modes only interacted with the externally applied stress. As a result, the number of allowable eigenmodes increased as the core width became wider. And more eigenmodes were activated as the core became stiffer. In particular, the SA mode had lower frequency than FA mode and its displacement distribution was more localized at edge atoms of the dislocation core than the FA mode. These characteristics made the SA mode produce larger drag force than the FA mode. In addition, there was an inverse relationship between the drag force and the dislocation core width. This tendency was equally observed in Chapter 3. Interestingly, our model could be connected to the Chapter 3 when the dislocation moves very fast with high frequency. In general, the dislocation core width depends on the dislocation velocity. Therefore, we expect that this work can be further applied to derive an *analytic* equation of dislocation motion, where the discrete nature of the core is well considered, as a future study.

Chapter 6
Concluding Remarks

Unlike the linear elastic theory that assumes a system as a continuous medium, the dislocation actually glides in a discrete system that consists of atoms. This results in energy dissipation through the emission of elastic waves whenever atomic bonds are broken by the external stress. And the emitted waves are scattered by anharmonic strain field around the dislocation core. As a result, the average stress around the moving dislocation core becomes lower than the external stress, which is called stress-drop behavior. In Chapter 2, it was proved that the phonon scattering around the dislocation core induces the stress-drop. Therefore, the phonon scattering model was the beginning of my journey to develop an equation of dislocation (and LAGB) motion.

However, in general, the moving dislocation does not lose its energy only by the bond-breaking process but it also lose by its oscillation due to various reasons. The dislocation oscillation is classified into two types whether it is forced or not. The former occurs when the dislocation interacts with external sources such as other dislocations or phonons. However, the dislocation can also spontaneously oscillate by the relativistic effect without the external sources and the oscillation becomes stronger as the dislocation velocity increases. From this, we could conclude that the moving dislocation always accompanies its oscillation. In Chapter 3, the oscillation effect was added to the phonon scattering model and finally the general equation of dislocation motion was derived. The developed equation required two phenomenological group parameters, C_1^{dis} and C_2^{dis}, and they quantified the drag force acting on the dislocation. Interestingly, the both parameters were closely related to structural properties of the dislocation core. All these theoretical results were supported by the MD simulations.

In addition to the dislocation, the equation of motion could be applied to the LAGBs in Chapter 4 given that they also oscillate because their consisting dislocations interact with each other. Since the dislocations comprising the LAGB do not only interact with neighboring ones but also with other ones by long-rang elastic strain field, the oscillation frequency of LAGB was much lower than it of dislocation. As a result, the dynamic drag effect slowed down the LAGB. Furthermore,

the proposed model could explain the unusual behaviors that were observed in the MD simulation but not explainable by the linear elasticity theory, i.e. the stress drop, a curved structure of the LAGBs, and the inverse relationship between the LAGB velocity and misorientation angle. Therefore, these results prove that the drag effect must be considered to analyze the dynamics of LAGBs.

In Chapter 5, the drag force was analytically investigated from a different angle. To directly extract an influence of phonons on the drag force as a mathematical form, the dislocation-phonon coordinate system was adopted rather than the commonly used atomic displacements coordinate. As a result, the drag force induced by the interaction between a dislocation and phonons was expressed as a separate term to represent *J*-integral and it made the *J*-integral be path-dependent. And by assuming the dislocation as a localized defect, the influence of dislocation core properties on the drag force was numerically investigated. To do this, the phonon coordinate was expressed as a superposition of independent eigenvectors, which were classified into symmetric and anti-symmetric oscillation modes. Furthermore, this approach enabled C_1^{dis} that quantified the drag force in Chapter 3 to be derived as a function of dislocation core width, frequency, and oscillation mode in high frequency limit.

In this dissertation, the fundamentals of drag force acting on a moving dislocation in the discrete medium were systematically explored under various environments and extended to the LAGBs. In particular, I focused on the fact that the result of drag mechanisms coincides as dislocation oscillation despite their sources are different. From this, the general equations of a moving dislocation and LAGBs to solve the dislocation velocity were derived. Furthermore, the relationship between the drag force and dislocation core properties was elucidated. The proposed approach in this dissertation has academic significance in that it can be *generally* applied to moving defects despite the diversity of the drag sources and may contributes to enhance an accuracy of multiscale plasticity analysis for extremely deformed materials.

Appendix. A

Derivation of dispersion relation in a triangular lattice

A displacement of wave that propagates along positive *x* axis with velocity *v* can be represented by

$$u(m,n) = u_0 \exp\left(iq_x\left(mb - vt\right)\right) \cdot \exp\left(iq_y nb\right), \tag{A.1}$$

where u_0 is an amplitude of the displacement and *b* is a distance between two neighboring atoms. Under the assumption of the closest interaction between atoms, the force equilibrium equation is derived as

$$\begin{aligned} M\ddot{u}(m,n) = K\big[&u(m+1/2, n+\sqrt{3}/2) + u(m+1/2, n-\sqrt{3}/2) + u(m+1, n) \\ &+ u(m-1/2, n+\sqrt{3}/2) + u(m-1/2, n-\sqrt{3}/2) + u(m-1, n) - 6u(m,n)\big] \end{aligned} \tag{A.2}$$

If we define $w \equiv q_x v$, then Eq. (A.2) finally becomes

$$w(q_x, q_y) = 2\sqrt{\frac{K}{M}}\left[\sin^2\frac{q_x b}{2} + \sin^2\frac{(q_x + \sqrt{3}q_y)b}{4} + \sin^2\frac{(q_x - \sqrt{3}q_y)b}{4}\right]^{1/2}. \tag{A.3}$$

Appendix. B

Derivation of the lattice Green's function

The lattice Green's function in one-dimensional lattice with considering an anharmonic atomic displacement was firstly derived by Ohashi[64] . We expanded it to two-dimensional case in our previous study[48] and reproduce it in here. If we define a displacement of atom *m* in response to elastic stress V_m, and additional deviation from the static equilibrium position due to anharmonic scattering as u_m, then total displacement becomes $V_m + u_m$. The total energy of the system *H* can be expressed by

$$H = \frac{1}{2}M\sum_n \dot{u}_n^2 + \sum_n A_n(V_n + u_n) + \frac{1}{2}\sum_m\sum_n B_{mn}(V_m + u_m)(V_n + u_n) + \frac{1}{6}\sum_l\sum_m\sum_n C_{lmn}(V_l + u_l)(V_m + u_m)(V_n + u_n) + O(V^4, u^4), \tag{B.1}$$

where A_n, B_{mn} and C_{lmn} are first, second, and third derivatives of potential energy in unconstrained state *E*, respectively. Here, A_n is equal to zero because the potential energy becomes minimum in equilibrium state and B_{mn} corresponds to an elastic constant. If we consider a potential energy occurred by only elastic displacement E_0, it is expressed as

$$E_0 = \frac{1}{2}\sum_m\sum_n B_{mn}V_mV_n + \frac{1}{6}\sum_l\sum_m\sum_n C_{lmn}V_lV_mV_n + O(V^4). \tag{B.2}$$

Since harmonic displacement minimizes system's potential energy, $\partial E_0/\partial V_n$ should be zero. Thus,

$$\sum_m B_{mn}V_m + \frac{1}{2}\sum_l\sum_m C_{lm}V_lV_m + O(V^3) = 0. \tag{B.3}$$

If we insert Eq. (B.3) into Eq. (B.1) and ignore the high-order terms, the total potential energy of the system becomes

$$E = E_0 + \frac{1}{2}\sum_m\sum_n B_{mn}u_mu_n + \frac{1}{2}\sum_l\sum_m\sum_n C_{lmn}V_lu_mu_n. \tag{B.4}$$

Therefore, the contribution of anharmonicity to system's total energy becomes

$$H_{anh} = \frac{1}{2} M \sum_m \dot{u}_m^2 + \frac{1}{2} \sum_m \sum_n B_{mn} u_m u_n + \frac{1}{2} \sum_l \sum_m \sum_n C_{lmn} V_l u_m u_n \,. \tag{B.5}$$

From $\partial H_{anh}/\partial t = 0$, the equation of motion is derived as Eq. (B.6).

$$M\ddot{u}_m \delta_{mn} + \sum_m B_{mn} u_m + \sum_l \sum_m C_{lmn} V_l u_m = 0 \,. \tag{B.6}$$

If we insert $u_m = u_0 \exp(-iwt)$, then Eq. (B.6) is converted to Eq. (B.7).

$$\sum_m [-Mw^2 \delta_{mn} + B_{mn}] u_m = -\sum_m \left[\sum_l C_{lmn} V_l \right] u_m \,. \tag{B.7}$$

In matrix equation, Eq. (B.7) becomes

$$\mathbf{L}\vec{\mathbf{u}} = \mathbf{\Delta L}\vec{\mathbf{u}} \tag{B.8}$$

where $L_{mn} = -Mw^2 \delta_{mn} + B_{mn} = M(w^2(k) - w^2)\delta_{mn}$ and $\Delta L_{mn} = -\sum_l C_{lmn} V_l$. Here, $w(k)$ is a dispersion of waves. The solution of Eq. (B.8) can be expressed as a sum of incoming and scattered waves, which are defined as $\vec{\mathbf{u}}_\mathbf{i}$ and $\vec{\mathbf{u}}_\mathbf{s}$, respectively. Since $\vec{\mathbf{u}}_\mathbf{i}$ is a homogenous but $\vec{\mathbf{u}}_\boldsymbol{s}$ is a particular solution, the solution of Eq. (B.8) can be derived as Eq. (B.9).

$$\vec{\mathbf{u}} = \vec{\mathbf{u}}_\mathbf{i} + \mathbf{L}^{-1}\mathbf{\Delta L}\vec{\mathbf{u}} \,. \tag{B.9}$$

If we define the lattice Green's function, **G**, as $\mathbf{G} \equiv \mathbf{L}^{-1}$. Thus, **G** is derived as Eq. (B.10) in first Brillouine zone (BZ).

$$G_{mn}(w) = \frac{b}{2\pi M} \int_{1st\,BZ} \frac{e^{ikb(m-n)}}{w^2(k) - w^2} dk \,. \tag{B.10}$$

In this work, however, we apply **G** in two-dimensional lattice so it is defined as Eq. (B.11).

$$G(\vec{\mathbf{r}} - \vec{\mathbf{r}}_\mathbf{0}, w) = \frac{b^2}{4\pi^2 M} \int_{1st\,BZ} \frac{e^{i\vec{\mathbf{k}}\cdot(\vec{\mathbf{r}} - \vec{\mathbf{r}}_\mathbf{0})}}{w^2(\vec{\mathbf{k}}) - w^2} d\vec{\mathbf{k}} \,. \tag{B.11}$$

Appendix. C

Minimum energy state of the LAGB based on the linear elasticity theory

Assume that N dislocations that they were initially at (x_0, y_i), where $i = 1,2,\cdots,N$, move positive x direction without cross-slip. At arbitrary time, t, the total energy of the system, E_{tot}, can be expressed by summation of elastic strain energy done by the externally applied stress, E_{app}, self-energy of each dislocation, E_{self}, and interaction energy between the dislocations, E_{int}, as Eq. (C.1).

$$E_{tot} = E_{app} + NE_{self} + E_{\text{int}}. \tag{C.1}$$

At dynamic equilibrium state, E_{tot} must be minimized with respect to dislocation position at t, $x_i(t)$. Since E_{app} and E_{self} are independent to the dislocation position, E_{tot} has minimum value when E_{int} is minimized.

The shear stress acting at (x, y) due to i th dislocation at (x_i, y_i), whose Burgers vector is **b**, is expressed as Eq. (C.2).

$$\sigma_{12}(x,y) = \frac{\mu b}{2\pi(1-\upsilon)} \frac{(x-x_i)[(x-x_i)^2 - (y-y_i)^2]}{[(x-x_i)^2 + (y-y_i)^2]^2} \tag{C.2}$$

where μ is a shear modulus, υ is Poisson's ratio. Thus, the shear stress acting at j th dislocation induced by interaction with other $N-1$ dislocations becomes

$$\sigma_{12}^{j} = \frac{\mu b}{2\pi(1-\nu)} \sum_{\substack{i=1 \\ (i\neq j)}}^{N} \frac{(x_j - x_i)[(x_j - x_i)^2 - (y_j - y_i)^2]}{[(x_j - x_i)^2 + (y_j - y_i)^2]^2}. \tag{C.3}$$

The interaction energy between the j th dislocation and other dislocations, E_{int}^{j}, is a work done by displacing the cut plane, $y = y_j$, to make the j th dislocation in the presence of stress field σ_{12}^{j} is derived as Eq. (C.4).

$$E_{\text{int}}^{j} = \int_{x_j}^{\infty} \sigma_{12}^{j} b dx_j \ . \tag{C.4}$$

Therefore, the total interaction energy can be derived as

$$E_{\text{int}} = \frac{1}{2}\sum_{j=1}^{N} E_{\text{int}}^{j} = \frac{\mu b}{4\pi(1-\nu)} \sum_{\substack{j=1 \\ (i\neq j)}}^{N} \sum_{i=1}^{N} \int_{x_j}^{\infty} \frac{(x_j - x_i)[(x_j - x_i)^2 - (y_j - y_i)^2]}{[(x_j - x_i)^2 - (y_j - y_i)^2]^2} dx_j \ . \tag{C.5}$$

To find the equilibrium state, both $\partial E_{int}/\partial x_j = 0$ and $\partial^2 E_{int}/\partial x_j^2 > 0$ must be satisfied. As a result, when $x_i = x_j \ (i = 1, 2, \cdots, N, (i \neq j))$, the both conditions are satisfied. In other words, when the LAGB maintains its configuration as a straight line, it has a minimum energy.

Appendix. D

Derivation of effective mass of the LAGB

The displacement at $\mathbf{r}$, $\mathbf{u}(\mathbf{r})$, can be described in complex plane as

$$\mathbf{u}(\mathbf{r}) = \sum_{\mathbf{q}} \sum_{p} u_{\mathbf{q}p} e^{i\mathbf{q}\cdot\mathbf{r}} \hat{\mathbf{e}}_{\mathbf{q}p} \tag{D.1}$$

where $\hat{\mathbf{e}}_{\mathbf{q}p}$ is a polarization vector for three modes $(p = 1,2,3)$, and q is a wavenumber. Here, $p = 1$ corresponds to longitudinal and $p = 2$ and 3 correspond to transverse modes of the dislocation. The dislocation is embedded as in Fig. 4.10a and its slip area is confined to $z = 0$ plane. Additionally, $\bar{\mathbf{u}}_{\mathbf{q}p} = \mathbf{u}_{-\mathbf{q}p}$ is satisfied.

The kinetic energy of system is derived as

$$T = \frac{1}{2}\rho V \left|\frac{d\mathbf{u}}{dt}\right|^2 = \frac{1}{2}\rho V \sum_{\mathbf{q}} \sum_{p} \bar{\mathbf{u}}_{\mathbf{q}p} \mathbf{u}_{\mathbf{q}p}\,, \tag{D.2}$$

where ρ and V is density and volume of the system, respectively. Elastic strain energy is expressed as

$$U_{elastic} = \frac{1}{2} V \sum_{p} C_p \left|\frac{\partial \mathbf{u}}{\partial \mathbf{r}}\right|^2 = \frac{1}{2} V \sum_{\mathbf{q}} \sum_{p} q^2 C_p \bar{\mathbf{u}}_{\mathbf{q}p} \mathbf{u}_{\mathbf{q}p}\,, \tag{D.3}$$

where $C_1 = 2\mu(1-\upsilon)/(1-2\upsilon)$ and $C_2 = C_3 = \mu$. Here, υ is Poisson's ratio. And the potential energy of LAGB is derived as

$$U_{LAGB} = \frac{1}{2} \sum_{\mathbf{R}} \int_{C} \mathbf{n}\cdot\boldsymbol{\sigma}(\mathbf{r}-\mathbf{R})\cdot\mathbf{b}\, dS = \frac{1}{2} \int_{C} n_i \left(\sum_{\mathbf{R}} \sigma_{ij}(\mathbf{r}-\mathbf{R}) \right) b_j\, dS, \tag{D.4}$$

where S is slipped area by each dislocation whose Burgers vector is $\mathbf{b}$ and is located at $\mathbf{R}$, and $\mathbf{n}$ is normal vector the area. Since only shear components of the stress contributes to U_{LAGB}, the stress is derived as

$$\boldsymbol{\sigma}(\mathbf{r}) = \mu \frac{\partial \mathbf{u}}{\partial \mathbf{r}} = i\mu \sum_{\mathbf{q}} \sum_{p} \left(\hat{\mathbf{q}} \hat{\mathbf{e}}_{\mathbf{q}p} + \hat{\mathbf{e}}_{\mathbf{q}p} \hat{\mathbf{q}} \right) q u_{\mathbf{q}p} e^{i\mathbf{q}\cdot\mathbf{r}}, \tag{D.5}$$

where $\hat{\mathbf{q}}$ is a normalized vector of $\mathbf{q}$. If we insert Eq. (D.5) into Eq. (D.4), Eq. (D.6) is derived.

$$U_{LAGB} = \frac{1}{2} \sum_{\mathbf{q}} \sum_{p} A_{\mathbf{q}p} \left(\sum_{\mathbf{R}} e^{-i\mathbf{q}\cdot\mathbf{R}} \right) u_{\mathbf{q}p}, \tag{D.6}$$

where

$$A_{\mathbf{q}p} = \mu b q \Phi_{\mathbf{q}p} f(\mathbf{q}), \tag{D.7}$$

$$\Phi_{\mathbf{q}p} = (\hat{\mathbf{n}} \cdot \hat{\mathbf{q}})(\hat{\mathbf{e}}_{\mathbf{q}p} \cdot \hat{\mathbf{b}}) + (\hat{\mathbf{n}} \cdot \hat{\mathbf{e}}_{\mathbf{q}p})(\hat{\mathbf{q}} \cdot \hat{\mathbf{b}}), \tag{D.8}$$

$$f(\mathbf{q}) = i \oint_{C} e^{i\mathbf{q}\cdot\mathbf{r}} dS \cdot \tag{D.9}$$

Here, $\hat{\mathbf{b}}$ is a normalized vector of $\mathbf{b}$. Furthermore, since elastic wave propagates from the free edges of system, each dislocation that consists the LAGB starts to move at different time. As a result, if we assume that 0-th dislocation starts to move at $t = 0$, j-th dislocation starts its motion at $t = -jd/C_t$ where d is a distance between neighboring dislocations and C_t is a speed of the shear wave. Therefore, $A_{\mathbf{q}p}$ becomes

$$A_{\mathbf{q}p}(\mathbf{q}, \mathbf{R}, \mathbf{v}, t) = \mu b q \Phi_{\mathbf{q}p} \left(i \oint_{C} e^{-i\mathbf{q}\cdot(\mathbf{r}-\mathbf{v}t)} \, dS \right) = A^{0}_{\mathbf{q}p} e^{-i\mathbf{q}\cdot\mathbf{v}t} e^{-i\mathbf{q}\cdot\mathbf{v}\frac{R}{C_t}}, \tag{D.10}$$

where $R = jd$. This leads U_{LAGB} to become

$$U_{LAGB} = \frac{1}{2} \sum_{\mathbf{q}} \sum_{p} A^{0}_{\mathbf{q}p} \left[\sum_{R} e^{-i\mathbf{q}\cdot R\left(\hat{\mathbf{e}}_3 + \frac{\mathbf{v}}{C_t} \right)} \right] e^{-i\mathbf{q}\cdot\mathbf{v}t} u_{\mathbf{q}p} = \frac{1}{2} \sum_{\mathbf{q}} \sum_{p} B_{\mathbf{q}p}(\mathbf{q}, \mathbf{v}, t) u_{\mathbf{q}p}, \tag{D.11}$$

where $B_{qp} = A^{0}_{\mathbf{q}p} \sum_{R} [\exp(-i\mathbf{q} \cdot R(\hat{\mathbf{e}}_3 + \mathbf{v}/C_t))] \exp(-i\mathbf{q} \cdot \mathbf{v}t)$.

Therefore, Lagrangian, L, becomes $L = T - (U_{elastic} + U_{LAGB})$. Through Euler-Lagrange equation in complex space, it is reduced to

$$\ddot{u}_{\mathbf{q}p} + w^{2}_{\mathbf{q}p} u_{\mathbf{q}p} + \frac{1}{\rho V} \overline{B}_{\mathbf{q}p} = 0, \tag{D.12}$$

where $w_{\mathbf{q}p} = q\sqrt{C_p/\rho}$. The solution of Eq. (D.12) is expressed by a sum of homogenous and

particular solutions as

$$u_{\mathbf{q}p} = u_{\mathbf{q}p}^h(t) + u_{\mathbf{q}p}^p(t) = c_{\mathbf{q}p}^1 e^{iw_{\mathbf{q}p}t} + c_{\mathbf{q}p}^2 e^{-iw_{\mathbf{q}p}t} - \frac{\overline{B}_{\mathbf{q}p}(t)}{\rho V\{w_{\mathbf{q}p}^2 - (\mathbf{q}\cdot\mathbf{v})^2\}}. \tag{D.13}$$

In addition to the energy of free oscillators, the particular solution induces kinetic energy occurred by uniform motion of the LAGB, T_{LAGB}. It becomes

$$\begin{aligned} T_{LAGB} &= \frac{1}{2}\rho V \sum_{\mathbf{q}}\sum_{p} \dot{\overline{u}}_{\mathbf{q}p}^{p}\dot{u}_{\mathbf{q}p}^{p} \\ &= \frac{1}{2}\frac{1}{\rho V}\sum_{\mathbf{q}}\sum_{p}(\mathbf{q}\cdot\mathbf{v})^2 \frac{\overline{B}_{\mathbf{q}p}B_{\mathbf{q}p}}{\{w_{\mathbf{q}p}^2 - (\mathbf{q}\cdot\mathbf{v})^2\}^2} \\ &= \frac{1}{2}\frac{1}{\rho V}\sum_{\mathbf{q}}\sum_{p}(\mathbf{q}\cdot\mathbf{v})^2 \frac{|B_{\mathbf{q}p}|^2}{w_{\mathbf{q}p}^4}\left\{1-\left(\frac{\mathbf{q}\cdot\mathbf{v}}{w_{\mathbf{q}p}}\right)^2\right\}^{-2} \\ &\approx \frac{1}{2}\frac{1}{\rho V}\sum_{\mathbf{q}}\sum_{p}(\mathbf{q}\cdot\mathbf{v})^2 \frac{|B_{\mathbf{q}p}|^2}{w_{\mathbf{q}p}^4}\left\{1+2\left(\frac{\mathbf{q}\cdot\mathbf{v}}{w_{\mathbf{q}p}}\right)^2\right\}. \end{aligned} \tag{D.14}$$

Also, additional potential energy becomes $U_{add} \sim \sum_{\mathbf{q}}\sum_{p}\bar{u}_{\mathbf{q}p}^{p}u_{\mathbf{q}p}^{p}$ so that

$$U_{add} \sim \frac{1}{(\rho V)^2}\sum_{\mathbf{q}}\sum_{p}\frac{|B_{\mathbf{q}p}|^2}{w_{\mathbf{q}p}^4}\left\{1+2\left(\frac{\mathbf{q}\cdot\mathbf{v}}{w_{\mathbf{q}p}}\right)^2\right\}. \tag{D.15}$$

By comparing the lowest-order term of $\mathbf{v}$ in between Eq. (D.14) and Eq. (D.15), it is concluded that the latter is negligible compared to the former. Therefore, it is valid to consider only kinetic term. As a result,

$$T_{LAGB} = \frac{1}{2}\frac{1}{\rho V}\sum_{\mathbf{q}}\sum_{p}(\mathbf{q}\cdot\mathbf{v})^2 \frac{|B_{\mathbf{q}p}|^2}{w_{\mathbf{q}p}^4} = \frac{1}{2}m_{ij}^{LAGB}v_i v_j, \tag{D.16}$$

where m_{ij}^{LAGB} is defined as an effective mass of LAGB. As a result, it is expressed as

$$m_{ij}^{LAGB} = \frac{\rho b^2}{V}\sum_{\mathbf{q}}\sum_{p}\left\{\frac{\mu\Phi_{\mathbf{q}p}|f(\mathbf{q})|}{C_p}\right\}^2\left[\sum_{R,R'}e^{-i\mathbf{q}\cdot(R-R')\left(\hat{\mathbf{e}}_3+\frac{\mathbf{v}}{C_t}\right)}\right]\hat{q}_i\hat{q}_j. \tag{D.17}$$

This is a general definition of the effective mass. Now, we derive m_{ij}^{LAGB} when the LAGB consists of infinitely-long straight dislocations.

From Fig. 4.10, we derive $f(\mathbf{q})$ for straight dislocation whose length is L at first. So, Eq. (D.9) becomes Eq. (D.18).

$$\begin{aligned} f(\mathbf{q}) &= i\int_{-\infty}^{0} e^{iq_y y}dy \int_{-L/2}^{L/2} e^{iq_x x}dx \\ &= \frac{2\sin(q_x L/2)}{q_x} i\int_{-\infty}^{0} e^{iq_y y}dy = \frac{2\sin(q_x L/2)}{q_x} i\int_{0}^{\infty} e^{-iq_y y}dy. \end{aligned} \tag{D.18}$$

By Ref. 51, Eq. (D.18) is converted to

$$f(\mathbf{q}) = \lim_{\sigma\to 0} \frac{2\sin(q_x L/2)}{q_x(q_y - i\sigma)}. \tag{D.19}$$

Since the dislocation moves *y* direction on $z = 0$ plane, the effective mass for $L \to \infty$ becomes

$$m_{yy}^{LAGB} = \frac{\rho b^2}{V} \lim_{\substack{\sigma\to 0 \\ L\to\infty}} \sum_{\mathbf{q}} \sum_{p} (\hat{q}_y)^2 \left\{ \frac{\mu\Phi_{\mathbf{q}p}}{C_p} \right\}^2 \left| \frac{2\sin(q_x L/2)}{q_x(q_y - i\sigma)} \right|^2 \left[\sum_{R,R'} e^{-i\mathbf{q}\cdot(R-R')\left(\hat{\mathbf{e}}_3 + \frac{\mathbf{v}}{C_t}\right)} \right]. \tag{D.20}$$

And by using Dirac delta function, $\delta(x)$, Eq. (D.21) is obtained.

$$\begin{aligned} \lim_{L\to\infty} \left| \frac{2\sin(q_x L/2)}{q_x(q_y - i\sigma)} \right|^2 &= \frac{2}{q_y^2 + \sigma^2} \lim_{L\to\infty} \frac{1-\cos(q_x L)}{q_x^2} \\ &= \frac{`}{\pi} \frac{2}{q_y^2 + \sigma^2} \lim_{L\to\infty} \frac{1}{L} \frac{1-\cos(q_x L)}{q_x^2} (\pi L) \\ &= \frac{2\pi L\delta(q_x)}{q_y^2 + \sigma^2}. \end{aligned} \tag{D.21}$$

If we insert Eq. (D.21) into Eq. (D.20) and replace $\Sigma_{\mathbf{q}}$ with $(V/2\pi)^3 \int d^3\mathbf{q}$, then the effective mass per unit length, m_{LAGB}^*, is derived as Eq. (D.22).

$$m_{LAGB}^* = \frac{\rho b^2}{4\pi^2} \sum_{R,R'} \int \left[(\hat{q}_y)^2 \delta(q_x) \frac{1}{q_y^2 + \sigma^2} \sum_{p} \left\{ \frac{\mu\Phi_{\mathbf{q}p}}{C_p} \right\}^2 \right] \left[e^{-i\mathbf{q}\cdot(R-R')\left(\hat{\mathbf{e}}_3 + \frac{\mathbf{v}}{C_t}\right)} \right] d\mathbf{q}. \tag{D.22}$$

By Ehelby[113], if we define $\boldsymbol{\varphi}_{\mathbf{q}} = (\hat{\mathbf{q}}\cdot\hat{\mathbf{b}})\hat{\mathbf{n}} + (\hat{\mathbf{q}}\cdot\hat{\mathbf{n}})\hat{\mathbf{b}}$, we can express $\Phi_{\mathbf{q}p}^2$ from Eq. (D.8).

$$\Phi_{qp}^2 = \boldsymbol{\varphi}_{\mathbf{q}} \cdot \hat{\mathbf{e}}_{\mathbf{q}p} \hat{\mathbf{e}}_{\mathbf{q}p} \cdot \boldsymbol{\varphi}_{\mathbf{q}} \tag{D.23}$$

Therefore,

$$\sum_p \left(\frac{\mu \Phi_{qp}}{C_p} \right)^2 = r\Phi_{q1}^2 + \Phi_{q2}^2 + \Phi_{q3}^2$$
$$= r\boldsymbol{\varphi}_\mathbf{q} \cdot \hat{\mathbf{e}}_{\mathbf{q}1}\hat{\mathbf{e}}_{\mathbf{q}1} \cdot \boldsymbol{\varphi}_\mathbf{q} + \boldsymbol{\varphi}_\mathbf{q} \cdot (\tilde{\mathbf{I}} - \hat{\mathbf{e}}_{\mathbf{q}1}\hat{\mathbf{e}}_{\mathbf{q}1}) \cdot \boldsymbol{\varphi}_\mathbf{q} \quad \text{(D.24)}$$
$$= \boldsymbol{\varphi}_\mathbf{q} \cdot (\tilde{\mathbf{I}} - (1-r)\hat{\mathbf{e}}_{\mathbf{q}1}\hat{\mathbf{e}}_{\mathbf{q}1}) \cdot \boldsymbol{\varphi}_\mathbf{q}$$
$$= \varphi_\mathbf{q}^2 - (1-r)(\boldsymbol{\varphi}_\mathbf{q} \cdot \hat{\mathbf{e}}_{\mathbf{q}1})^2 .$$

where $r = \mu / C_1$ and $\tilde{\mathbf{I}} = \hat{\mathbf{e}}_{\mathbf{q}1}\hat{\mathbf{e}}_{\mathbf{q}1} + \hat{\mathbf{e}}_{\mathbf{q}2}\hat{\mathbf{e}}_{\mathbf{q}2} + \hat{\mathbf{e}}_{\mathbf{q}3}\hat{\mathbf{e}}_{\mathbf{q}3}$ is the identity tensor. Since we define $\hat{\mathbf{e}}_{\mathbf{q}1} = \hat{\mathbf{q}}$, Eq. (D.24) is converted to Eq. (D.25).

$$\sum_p \left(\frac{\mu \Phi_{qp}}{C_p} \right)^2 = (\hat{\mathbf{q}} \cdot \hat{\mathbf{b}})^2 + (\hat{\mathbf{q}} \cdot \hat{\mathbf{n}})^2 - 4(1-r)(\hat{\mathbf{q}} \cdot \hat{\mathbf{b}})^2 (\hat{\mathbf{q}} \cdot \hat{\mathbf{n}})^2 . \quad \text{(D.25)}$$

If we define $\hat{\mathbf{q}} = \hat{q}_x\hat{\mathbf{e}}_\mathbf{1} + \hat{q}_y\hat{\mathbf{e}}_\mathbf{2} + \hat{q}_z\hat{\mathbf{e}}_\mathbf{3}$, $\hat{\mathbf{b}} = \cos\Theta\,\hat{\mathbf{e}}_\mathbf{1} + \sin\Theta\,\hat{\mathbf{e}}_\mathbf{2}$, and $\hat{\mathbf{n}} = \hat{\mathbf{e}}_\mathbf{3}$ according to Fig. 4.10, Eq. (D.25) becomes

$$\sum_p \left(\frac{\mu \Phi_{qp}}{C_p} \right)^2 = (\hat{q}_x \cos\Theta + \hat{q}_y \sin\Theta)^2 + \hat{q}_z^2 - 4(1-r)\hat{q}_z^2 (\hat{q}_x \cos\Theta + \hat{q}_y \sin\Theta)^2 , \quad \text{(D.26)}$$

where Θ is an angle between dislocation line and Burgers vector. After inserting Eq. (D.26) to Eq. (D.22), the integration is carried out over a sphere, whose radius is q_D that is defined as Debye cutoff. Owing to the existence of $\delta(q_x)$ in the integrand, the integration regime is confined to a circle on $q_x = 0$ plane. So if we define $q_y = q\cos\theta$ and $q_z = q\sin\theta$ where $q = \sqrt{q_y^2 + q_z^2}$ and let $\sigma \to 0$, Eq. (D.22) becomes

$$m_{LAGb}^* = \frac{\rho b^2}{4\pi^2} \int_\sigma^{q_D} \frac{1}{q} dq$$
$$\int_0^{2\pi} \left[\cos^2\theta \sin^2\Theta + \sin^2\theta - 4(1-r)\sin^2\theta \cos^2\theta \sin^2\Theta \right] \left[\sum_{R,R'} e^{-iq(R-R')(\sin\theta + \frac{v}{C_t}\cos\theta)} \right] d\theta .$$
(D.27)

If we define $\mathrm{f}(\theta) \equiv \sin\theta + (v/C_t)\cos\theta$, following relation is satisfied.

$$\sum_{R,R'} e^{-iq(R-R')f(\theta)} = \sum_{j=-N}^{N} e^{-iqdjf(\theta)} \sum_{j'=-N}^{N} e^{iqdj'f(\theta)} = \left(\sum_{j'=-N}^{N} e^{iqdj'f(\theta)} \right)^2$$
$$= 2\sum_{k=1}^{2N}(2N+1-k)\cos(qkdf(\theta)) + 2N+1, \tag{D.28}$$

where $2N+1$ is the total number of dislocations that make up the LAGB. As a result, the effective mass becomes

$$m^*_{LAGB} = \frac{\rho b^2}{4\pi^2} \int_{\sigma}^{q_D} \int_{0}^{2\pi} \frac{1}{q} \left[\cos^2\theta \sin^2\Theta + \sin^2\theta - 4(1-r)\sin^2\theta\cos^2\theta\sin^2\Theta \right]$$
$$\left[2N+1+2\sum_{k=1}^{N}(2N+1-k)\cos(gkdf(\theta)) \right] dqd\theta. \tag{D.29}$$

Since all the LAGBs that are considered in our work consist of only edge-type dislocations whose Burgers vector lies on xy plane, $\Theta = \pi/2$ is inserted. Then, Eq. (D.29) is simplified to

$$m^*_{LAGb} = \frac{\rho b^2}{4\pi}(2N+1)(1+r)\ln\left(\frac{q_D}{\sigma}\right)$$
$$+ \frac{\rho b^2}{2\pi^2}\sum_{k=1}^{2N}(2N+1-k)\int_{0}^{2\pi}\left[1-4(1-r)\sin^2\theta\cos^2\theta\right]d\theta\int_{0}^{q_D}\frac{1}{q}\cos(qkdf(\theta))dq. \tag{D.30}$$

If we use following relation

$$\int \frac{\cos(x)}{x}dx = \frac{1}{2}\sum_{n=1}^{\infty}\frac{(-1)^n x^{2n}}{n(2n)!} + \ln(x) + \gamma + const\ , \tag{D.31}$$

where γ is Euler-Mascheroni constant, the Eq. (D.30) becomes

$$m^*_{LAGB} = \frac{\rho b^2}{4\pi}(2N+1)(1+r)\ln\left(\frac{q_D}{\sigma}\right) + \frac{\rho b^2}{2\pi}(1+r)\sum_{k=1}^{2N}(2N+1-k)\ln\left(\frac{q_D}{\sigma}\right)$$
$$+ \frac{\rho b^2}{4\pi^2}\sum_{k=1}^{2N}\sum_{n=1}^{\infty}(2N+1-k)\frac{(-1)^n(q_D kd)^{2n}}{n(2n)!}\int_{0}^{2\pi}(f(\theta))^{2n}\left[1-4(1-r)\sin^2\theta\cos^2\theta\right]d\theta. \tag{D.32}$$

Since $\sum_{k=1}^{2N}(2N+1-k) = N(N+1)$, the effective mass of LAGB is finally derived as

$$
\begin{aligned}
m^*_{LAGb} &= \frac{\rho b^2}{4\pi}(1+r)(2N^2+4N+1)\ln\left(\frac{q_D}{\sigma}\right) \\
&\quad + \frac{\rho b^2}{4\pi^2}\sum_{k=1}^{2N}\sum_{n=1}^{\infty}(2N+1-k)\frac{(-1)^n(q_D kd)^{2n}}{n(2n)!}\int_0^{2\pi}(f(\theta))^{2n}\left[1-(1-r)\sin^2 2\theta\right]d\theta \\
&= (2N^2+4N+1)m^*_{dis} + \frac{\rho b^2}{4\pi^2}\sum_{k=1}^{2N}\sum_{n=1}^{\infty}(2N+1-k)\frac{(-1)^n(q_D kd)^{2n}}{n(2n)!}\int_0^{2\pi}(f(\theta))^{2n}\,g(\theta)d\theta,
\end{aligned}
$$

(D.33)

where $m^*_{dis} = (\rho b^2/4\pi)(1+r)\ln(q_D/\sigma)$ and $g(\theta) = 1-(1-r)\sin^2 2\theta$. Here m^*_{dis} is effective mass of single edge dislocation, which was derived by Brailsford[111]. And since q_D is defined in discrete momentum space, the system has finite number of degree of freedoms. Therefore, q_D is defined as $(6\pi^2/\Gamma)^{1/3}$ where Γ is an atomic volume in real space.

Appendix. E

Classifying eigenmodes of G-matrix

In Eq. (5.73), the eigenvalues and eigenvectors for mode μ of $\mathbf{G}$ can be obtained by solving Eq. (E.1)

$$\mathbf{G}\boldsymbol{\psi}^{\mu} = \beta^{\mu}\boldsymbol{\psi}^{\mu}. \tag{E.1}$$

In tensor form, Eq. (E.1) is expressed as

$$G_{i,j}\psi_j^{\mu} - \beta^{\mu}\delta_{i,k}\psi_k^{\mu} = 0. \tag{E.2}$$

Here, a comma does not mean differentiation but was used to distinguish matrix element. From the mathematical form of $\mathbf{G}$, its element satisfies

$$G_{i,j} = G_{N+1-i,N+1-j}, \tag{E.3}$$

where N is the total number of column vectors of $\mathbf{G}$. Note that N is odd number. Thus, Eq. (E.4) is also satisfied.

$$G_{i,j}\psi_{N+1-j}^{\mu} - \beta^{\mu}\delta_{N+1-i,k}\psi_k^{\mu} = 0. \tag{E.4}$$

By adding Eq. (E.4) to Eq. (E.2) and subtracting Eq. (E.4) from Eq. (E.2), Eq. (E.5) and (E.6) are derived, respectively.

$$G_{i,j}\left(\psi_j^{\mu} + \psi_{N+1-j}^{\mu}\right) - \beta^{\mu}\left(\psi_i^{\mu} + \psi_{N+1-i}^{\mu}\right) = 0, \tag{E.5}$$

$$G_{i,j}\left(\psi_j^{\mu} - \psi_{N+1-j}^{\mu}\right) - \beta^{\mu}\left(\psi_i^{\mu} - \psi_{N+1-i}^{\mu}\right) = 0. \tag{E.6}$$

In order to satisfy both Eq. (E.5) and (E.6) for arbitrary $\mathbf{G}$ and β^{μ}, $\Psi_i^{\mu} = -\Psi_{N+1-i}^{\mu}$ or $\Psi_i^{\mu} = \Psi_{N+1-i}^{\mu}$ must be satisfied, respectively. The former corresponds to anti-symmetric mode and the latter corresponds to symmetric modes. Note that $\Psi_{(N+1)/2}^{\mu}$ that is a center element of the

eigenvector must be always zero for the anti-symmetric mode but can be any value for the symmetric mode. Especially, among the symmetric modes, there is one mode where all elements of its eigenvector are same. This is a rigid mode and corresponding eigenvalue is zero. This is proved in Appendix F.

Appendix. F

Eigenvalue of the rigid mode

Since the eigenvector of rigid mode is $\Psi = [11\cdots 1]^{\mathrm{T}}$, $\upsilon(n)$ becomes

$$\upsilon(n) = (1-P)\left[g(n+\sigma_G) - g(n+\sigma_G+1) + g(n-\sigma_G) - g(n-\sigma_G-1) - 4f^2 \sum_{m=-\sigma_G}^{\sigma_G} g(n-m) \right] \tag{F.1}$$

for $n = -\sigma_G - 1$ and $n = \sigma_G + 1$ by Eq. (5.72-1) and

$$\upsilon(n) = (1-P)\left[g(n+\sigma_G) - g(n+\sigma_G+1) + g(n-\sigma_G) - g(n-\sigma_G-1) - 4f^2 \sum_{m=-\sigma_G}^{\sigma_G} g(n-m) + 1 \right] \tag{F.2}$$

for $-\sigma_G \le n \le \sigma_G$ by Eq. (5.72-2). If we define bracket terms in Eq. (F.1) and (F.2) as F_1 and F_2, respectively, then

$$F_1 = g(n+\sigma_G) - g(n+\sigma_G+1) + g(n-\sigma_G) - g(n-\sigma_G-1) - 4f^2 \sum_{m=-\sigma_G}^{\sigma_G} g(n-m) \quad . \tag{F.3}$$

$$F_2 = g(n+\sigma_G) - g(n+\sigma_G+1) + g(n-\sigma_G) - g(n-\sigma_G-1) - 4f^2 \sum_{m=-\sigma_G}^{\sigma_G} g(n-m) + 1 \quad . \tag{F.4}$$

Case 1. $n = -\sigma_G - 1$ or $n = \sigma_G + 1$

In this case, Eq. (F.3) becomes

$$\begin{aligned} F_1 &= g(1) - g(0) + g(2\sigma_G+1) - g(2\sigma_G+2) - 4f^2 \sum_{m=-\sigma_G}^{\sigma_G} g(\sigma_G+1-m) \\ &= -\frac{1+e^{-z}}{2\sinh z}\left(1+e^{-(2\sigma_G+1)z}\right) - 4f^2 \sum_{m=-\sigma_G}^{\sigma_G} g(\sigma_G+1-m). \end{aligned} \tag{F.5}$$

Since

$$\sum_{m=-\sigma_G}^{\sigma_G} g(\sigma_G+1-m) = g(1)+g(2)+\cdots+g(2\sigma_G+1) = -\frac{1}{2\sinh z}\frac{1+e^{-(2\sigma_G+1)z}}{1+e^{z}}\ , \qquad \text{(F.6)}$$

Eq. (F.5) becomes

$$\begin{aligned} F_1 &= -\frac{1+e^{-z}}{2\sinh z}\left(1+e^{-(2\sigma_G+1)z}\right)+\frac{4f^2}{2\sinh z}\left(1+e^{-(2\sigma_G+1)z}\right) \\ &= -\frac{\left(1+e^{-(2\sigma_G+1)z}\right)}{2\sinh z}\left[(1+e^{-z})-\frac{4f^2}{1+e^{z}}\right]. \end{aligned} \qquad \text{(F.7)}$$

Since $f=\cosh(z/2)$, the bracket term in Eq. (F.7) becomes zero. Therefore,

$$\upsilon(n) = G_{nk}\psi_k = 0\,. \qquad \text{(F.8)}$$

for $n=-\sigma_G-1$ or $n=\sigma_G+1$.

Case 2. $-\sigma_G \le n \le \sigma_G$

In this case, Eq. (F.4) becomes

$$F_2 = \frac{(-1)^{n+\sigma_G}}{\sinh z}e^{-\sigma_G z}(1+e^{-z})\cosh(nz) - 4f^2\sum_{m=-\sigma_G}^{\sigma_G} g(n-m)+1\ . \qquad \text{(F.9)}$$

First, if $n+\sigma_G$ is odd number, the second term in the RHS of Eq. (F.9) becomes

$$\begin{aligned}
\sum_{m=-\sigma_G}^{\sigma_G} g(n-m) &= g(n+\sigma_G)+g(n+\sigma_G-1)+\cdots+g(0)+g(1)+\cdots g(n-\sigma_G+1)+g(n-\sigma_G) \\
&= -\frac{1}{2\sinh z}\left[\left(e^{-(n+\sigma_G)z}-e^{-(n+\sigma_G-1)z}\right)+\left(e^{-(n+\sigma_G-2)z}-e^{-(n+\sigma_G-3)z}\right)+\cdots+\left(e^{-z}-1\right)\right] \\
&\quad -\frac{1}{2\sinh z}\left[\left(e^{-z}-e^{-2z}\right)+\cdots+\left(e^{-(n-\sigma_G+2)z}-e^{-(n-\sigma_G+1)z}\right)\right]-\frac{1}{2\sinh z}e^{(n-\sigma_G)z} \\
&= -\frac{(1-e^{z})}{2\sinh z}e^{-(n+\sigma_G)z}\left[1+e^{2z}+\cdots+e^{(n+\sigma_G-1)z}\right]-\frac{(1-e^{-z})}{2\sinh z}e^{-z}\left[1+e^{-2z}+\cdots+e^{(n-\sigma_G+3)z}\right] \\
&\quad -\frac{1}{2\sinh z}e^{(n-\sigma_G)z} \\
&= -\frac{(1-e^{z})}{2\sinh z}e^{-(n+\sigma_G)z}\frac{1-e^{(n+\sigma_G+1)z}}{1-e^{2z}}-\frac{(1-e^{-z})}{2\sinh z}e^{-z}\frac{1-e^{(n-\sigma_G+1)z}}{1-e^{-2z}}-\frac{1}{2\sinh z}e^{(n-\sigma_G)z} \\
&= -\frac{1}{2\sinh z}\left[\frac{2e^{-\sigma_G z}}{1+e^{z}}\cosh(nz)-\tanh\left(\frac{z}{2}\right)\right].
\end{aligned} \tag{F.10}$$

If we insert Eq. (F.10) into Eq. (F.9), then

$$\begin{aligned}
F_2 &= -\frac{e^{-\sigma_G z}\cosh(nz)}{\sinh z}\left[(1+e^{-z})-\frac{4f^2}{1+e^{z}}\right]-\frac{2f^2}{\sinh z}\tanh\left(\frac{z}{2}\right)+1 \\
&= -\frac{e^{-\sigma_G z}\cosh(nz)}{\sinh z}\left[(1+e^{-z})-\frac{4f^2}{1+e^{z}}\right]-\frac{f^2}{\cosh^2(z/2)}+1.
\end{aligned} \tag{F.11}$$

Since $f=\cosh(z/2)$, the bracket term in Eq. (F.11) becomes zero and finally, $F_2=0$. Second, if $n+\sigma_G$ is even number, the second term in the RHS of Eq. (F.9) becomes

$$\begin{aligned}
\sum_{m=-\sigma_G}^{\sigma_G} g(n-m) &= \frac{(1-e^{z})}{2\sinh z}e^{-(n+\sigma_G)z}\left[1+e^{2z}+\cdots+e^{(n+\sigma_G-2)z}\right]+\frac{(1-e^{-z})}{2\sinh z}e^{-z}\left[1+e^{-2z}+\cdots+e^{(n-\sigma_G+2)z}\right] \\
&\quad +\frac{1}{2\sinh z}e^{(n-\sigma_G)z} \\
&= \frac{(1-e^{z})}{2\sinh z}e^{-(n+\sigma_G)z}\frac{1-e^{(n+\sigma_G)z}}{1-e^{2z}}+\frac{(1-e^{-z})}{2\sinh z}e^{-z}\frac{1-e^{(n-\sigma_G)z}}{1-e^{-2z}}-\frac{1}{2\sinh z}e^{(n-\sigma_G)z} \\
&= \frac{1}{2\sinh z}\left[\frac{2e^{-\sigma_G z}}{1+e^{z}}\cosh(nz)+\tanh\left(\frac{z}{2}\right)\right].
\end{aligned} \tag{F.12}$$

If we insert Eq. (F.12) into Eq. (F.9), then

$$F_2 = \frac{e^{-\sigma_G z}\cosh(nz)}{\sinh z}\left[(1+e^{-z}) - \frac{4f^2}{1+e^z}\right] - \frac{2f^2}{\sinh z}\tanh\left(\frac{z}{2}\right) + 1$$
$$= \frac{e^{-\sigma_G z}\cosh(nz)}{\sinh z}\left[(1+e^{-z}) - \frac{4f^2}{1+e^z}\right] - \frac{f^2}{\cosh^2(z/2)} + 1. \quad \text{(F.13)}$$

Since $f = \cosh(z/2)$, the bracket term in Eq. (F.13) becomes zero and finally, $F_2 = 0$. As a result, Eq. (F.8) is also satisfied for $-\sigma_G \le n \le \sigma_G$. Therefore, we proved that $\mathbf{G\Psi} = \mathbf{0}$, or $\beta = 0$ for the rigid mode.

References

1. Volterra, V., 1907. Sur l'équilibre des corps élastiques multiplement connexes. *Ecole Norm. Super.* **24**, 401-517.

2. Marian, J., Cai, W. & Bulatov, V. V., 2004. Dynamic transitions from smooth to rough to twinning in dislocation motion. *Nat. Mater.* **3**, 158-163.

3. Gordon, P. A., Neeraj, T., Li, Y. & Li, J., 2010. Screw dislocation mobility in BCC metals: the role of the compact core on double-kink nucleation. *Model. Simul. Mater. Sci. Eng.* **18**, 085008.

4. Osetsky, Y. N. & Bacon, D. J., 2003. An atomic-level model for studying the dynamics of edge dislocations in metals. *Model. Simul. Mater. Sci. Eng.* **11**, 427-446.

5. Cai, W., Bulatov, V. V., Chang, J., Li, J. & Yip, S., 2004. Dislocation core effects on mobility, in : F. R. N. Nabarro (Ed.). *Dislocations in Solids* (North-Holland, Amsterdam).

6. Takeuchi, S., 1999. Dislocation core effects on plasticity. *Rad. Eff. Defects. Sol.* **148**, 333-344.

7. Justo, J. F., Bulatov, V. V. & Yip, S., 1999. Dislocation core reconstruction and its effect on dislocation mobility in silicon. *J. Appl. Phys.* **86**, 4249-4257.

8. Maeda, K. & Takeuch, S., 1996. Enhancement of dislocation mobility in semiconducting crystals by electronic excitation, in : F. R. N. Nabarro, M. S. Duesbery (Eds.). *Dislocations in Solids* (North-Holland, Amsterdam).

9. Wang, J. N., 1996. Prediction of Peierls stresses for different crystals. *Mater. Sci. Eng. A* **206**, 259-269.

10. Duesbery, M. S., 1989. The dislocation core and plasticity, in: F. R. N. Nabarro (Ed.). *Dislocations in Solids* (North-Holland, Amsterdam).

11. Aubry, S., Kang, K., Ryu, S. & Cai, W., 2011. Energy barrier for homogeneous dislocation nucleation: comparing atomistic and continuum models. *Scr. Mater.* **64**, 1043-1046.

12. Woodward, C., Trinkle, D. R., Hector Jr, L. G. & Olmsted, D. L., 2008. Prediction of dislocation cores in aluminum from density functional theory. *Phys. Rev. Lett.* **100**, 045507.

13. Ninomiya, T., 1968. Dislocation vibration and phonon scattering. *J. Phys. Soc. Jpn.* **25**, 830-840.

14. Glass, N. E., 1983. A lattice-dynamics model of an oscillating screw dislocation. *J. Phys.* **44**, 741-753.

15. Earmme, Y. Y. & Weiner, J. H., 1977. Dislocation dynamics in the modified Frenkel-Kontorova model. *J. Appl. Phys.* **48**, 3317-3331.

16. Lee, M. G., Lim, H., Adams, B. L., Hirth, J. P. & Wagoner, R. H., 2010. A dislocation density-based single crystal constitutive equation. *Int. J. Plast.* **26**, 925-938.

17. Rodríguez-Martínez, J. A., Rodríguez-Millan, M., Rusinek, A. & Arias, A., 2011. A dislocation-based constitutive description for modeling the behavior of FCC metals within wide ranges of strain rate and temperature. *Mech. Mater.* **43**, 901-912.

18. Resende, T. C., Bouvier, S., Abed-Meraim, F., Balan, T. & Sablin, S. –S., 2013. Dislocation-based model for the prediction of behavior of b.c.c. materials – Grain size and strain path effects. *Int. J. Plast.* **47**, 29-48.

19. Ha, S., Jang, J. –H. & Kim, K. T., 2017. Finite element implementation of dislocation-density-based crystal plasticity model and its application to pure aluminum crystalline materials. *Int. J. Mech. Sci.* **120**, 249-262.

20. Castelluccio, G. M. & McDowell, D. L., 2017. Mesoscale cyclic crystal plasticity with dislocation substructures. *Int. J. Plast.* **98**, 1-26.

21. Sung, J. H., Kim, J. H. & Wagoner, R. H., 2010. A plastic constitutive equation incorporating strain, strain-rate, and temperature. *Int. J. Plast.* **26**, 1746-1771.

22. Gao, C. Y. & Zhang, L. C., 2012. Constitutive modelling of plasticity of fcc metals under extremely high strain rates. *Int. J. Plast.* **32-33**, 121-133.

23. Ardeljan, M., Beyerlein, I. J. & Knezevic, M., 2014. A dislocation density based crystal plasticity finite element model: Application to a two-phase polycrystalline HCP/BCC composites. *J. Mech. Phys. Solids.* **66**, 16-31.

24. Bertin, N. & Capolungo, L., 2018. A FFT-based formulation for discrete dislocation dynamics in heterogeneous media. *J. Comp. Phys.* **355**, 366-384.

25. Santos-Güemes, R., Esteban-Manzanares, G., Papadimitriou, I., Segurado, J., Capolungo, L. & LLorca, J., 2018. Discrete dislocation dynamics simulations of dislocation-θ' precipitate interaction in Al-Cu alloys. *J. Mech. Phys. Solids* **118**, 228-244.

26. Rao, S. I., Woodward, C., Akdim, B., Antillon, E., Parthasarathy, T. A., El-Awady, J. A. & Dimiduk, D. M., 2019. Large-scale dislocation dynamics simulations of strain hardening of Ni microcrystals under tensile loading. *Acta. Mater.* **164**, 171-183.

27. Eshelby, J. D., 1956. Supersonic dislocations and dislocations in dispersive media. *Proc. Phys. Soc.* B **69**, 1013-1019.

28. Hirth, J. P. & Lothe. J., 1982. *Theory of dislocations*, Wiley.

29. Markenscoff, X. & Ni, L., 2001. The transient motion of a dislocation with a ramp-like core. *J. Mech. Phys. Solids* **49**, 1603-1619.

30. Pellegrini, Y. –P., 2014. Equation of motion and subsonic-transonic transitions of rectilinear edge dislocations: A collective-variable approach. *Phys. Rev. B* **90**, 054120.

31. Koizumi, H., Kirchner, H. O. K. & Suzuki, T., 2002. Lattice wave emission from a moving dislocation. *Phys. Rev. B* **65**, 214104

32. Wei, Y. & Peng, S. Y., 2017. The stress-velocity relationship of twinning partial dislocations and the phonon-based physical interpretation. *Sci. China-Phys. Mech. Astron.* **60**, 114611.

33. Peng, S., Wei, Y., Jin, Z. & Yang, W., 2019. Supersonic screw dislocations gliding at the shear wave speed. *Phys. Rev. Lett.* **122**, 045501.

34. Gumbsch, P. & Gao, H., 1999. Dislocations faster than the speed of sound. *Science* **283**, 965-968.

35. Tsuzuki, H., Branicio, P. S. & Rino, J. P., 2008. Accelerating dislocations to transonic

and supersonic speeds in anisotropic metals. *Appl. Phys. Lett.* **92**, 191909.

36. Atkinson, W. & Cabrera, N., 1965. Motion of a Frenkel-Kontorowa dislocation in a one-dimensional crystal. *Phys. Rev.* **138**, 763-766.

37. Swinburne, T. D. & Dudarev, S. L., 2015. Phonon drag force acting on a mobile crystal defect: Full treatment of discreteness and nonlinearity. *Phys. Rev. B* **92**, 134302.

38. Verschueren, J., Gurrutxaga-Lerma, B., Balint, D. S., Sutton, A. P. & Dini, D., 2018. Instabilities of high speed dislocations. *Phys. Rev. Lett.* **121**, 145502.

39. Amrit, J., Ramiere, A. & Volz, S., 2018. Role of fluttering dislocations in the thermal interface resistance between silicon crystal and plastic solid ^{4}He. *Phys. Rev. B* **97**, 014308.

40. Chen, X., Xiong, L., McDowell, D. & Chen, Y., 2017. Effects of phonons on mobility of dislocations and dislocation arrays. *Scr. Mater.* **137**, 22-26.

41. Alshits, V. I. & Sandler, Yu. M., 1974. Flutter mechanism of dislocation drag. *Phys. Stat. Sol. B* **64**, K45-K49.

42. Blaschke, D. N., 2019. Properties of dislocation drag from phonon wind at ambient conditions. *Materials* **12**, 948.

43. Al'shitz, V. A. & Indenbom, V. L., 1975. Dynamic dragging of dislocation. *Sov. Phys. Usp.* **18**, 1-20.

44. Al'shitz, V. I., Mitlianskij, M. D. & Kotowski, R. K., 1979. The phonon wind as a non-linear mechanism of dislocation dragging. *Arch. Mech.* **31**, 91-105.

45. Brailsford, A. D., 1972. Anharmonicity contributions to dislocation drag. *J. Appl. Phys.* **43**, 1380-1393.

46. Blaschke, D. N., Mottola, E. & Preston, D. L., 2018. On the velocity dependence of the dislocation drag coefficient from phonon wind. Tech. Rep. LA-UR-16-24559, Los Alamos Natl. Lab www.osti.gov/biblio/1434423/.

47. Kresse, O. & Truskinovsky, L., 2003. Mobility of lattice defects: discrete and continuum approaches. *J. Mech. Phys. Solids* **51**, 1305-1332.

48. Kim, S., Ho, D. T., Kang, K., Kim & S. Y., 2016. Phonon scattering during dislocation

motion inducing stress-drop in cubic metals. *Acta. Mater.* **115**, 143-154.

49. Wang, L. & Abeyaratne, R., 2018. A one-dimensional peridynamic model of defect propagation and its relation to certain other continuum models. *J. Mech. Phys. Solids* **116**, 334-349.

50. Celli, V. & Flytzanis, N., 1970. Motion of screw dislocation in a crystal. *J. Appl. Phys.* **41**, 4443-4447.

51. Heitler, W., 1944. *The Quantum theory of Radiation*, 2nd Ed., Oxford.

52. Kresse, O. & Truskinovsky, L., 2007. Prototypical lattice model of a moving defect: The role of environmental viscosity. *Phys. Solids. Earth.* **43**, 63-66.

53. Ishioka, S., 1971. Uniform motion of a screw dislocation in a lattice. *J. Phys. Soc. Jpn.* **30**, 323-327.

54. Sanders, W. T., 1962. Peierls stress for an idealized crystal model. *Phys. Rev.* **128**, 1540-1549.

55. Kuskin, A. Y. & Yanilkin, A. V., 2013. Atomistic simulation of the motion of dislocations in metals under phonon drag conditions, *Phys. Solid. State.* **55**, 1010-1019.

56. Ninomiya, T., 1974. Frictional force acting on a dislocation –Fluttering mechanism. *J. Phys. Soc. Jpn.* **36**, 399-405.

57. Ninomiya, T. & Ishioka, S., 1967. Dislocation vibration: Effective mass and line tension. *J. Phys. Soc. Jpn.* **23**, 361-372.

58. Plimpton, S., 1995. Fast parallel algorithms for short-range molecular dynamics. *J. Comp. Phys.* **117**, 1-19.

59. Mendelev, M. I., Han, S., Srolovitz, D. J., Ackland, G. J., Sun, D. Y. & Asta, M., 2003. Development of new interatomic potentials appropriate for crystalline and liquid iron, *Phil. Mag. A.* **83**, 3977-3994.

60. Smirnova, D. E., Kuskin, A. Y., Starikov, S. V., Stegailov, V. V., Insepov, Z., Rest, J. & Yacout, A. M., 2013. A ternary EAM interatomic potential for U-Mo alloys with xenon. *Model. Simul. Mater. Sci. Eng.* **21**, 035011.

61. Nosé, S., 1984. A unified formulation of the constant temperature molecular dynamics

methods, *J. Chem. Phys.* **81**, 511-519.

62. Hoover, W. G., 1985. Canonical dynamics: Equilibrium phase-space distributions, *Phys. Rev. A* **31**, 1695-1697.

63. Filippova, V. P., Kunavin, S. A. & Pugachev, M. S., 2015. Calculation of the parameters of the Lennard-Jones potential for pairs of identical atoms based on the properties of solid substances. *Inorg. Mater: Appl. Res.* **6**, 1-4.

64. Ohashi, K., 1968. Scattering of lattice waves by dislocations. *J. Phys. Soc. Jpn.* **24**, 437-445.

65. Weinberger, C. R., 2010. Dislocation drag at the nanoscale. *Acta. Mater.* **58**, 6535-6541.

66. Koehler, J. S., 1955. The velocity of dislocations. *J. Phys. Soc. Jap.* **10**, 669-672.

67. Granato, A. & Lücke, K., 1956. Theory of mechanical damping due to dislocations. *J. Appl. Phys.* **27**, 583-593.

68. Simpson, H. M. & Sosin, A. 1971. Contribution of defect dragging to dislocation damping. I. Theory. *Phys. Rev. B* **5**, 1382-1393.

69. Simpson, H. M., Sosin, A. & Johnson, D. F. 1971. Contribution of defect dragging to dislocation damping. II. Experimental. *Phys. Rev. B* **5**, 1393-1401.

70. Krasnikov, V. S. & Mayer, A. E., 2018. Influence of local stresses on motion of edge dislocation in aluminum. *Int. J. Plast.* **101**, 170-187.

71. Marian, J. & Caro, A., 2006. Moving dislocations in disordered alloys: Connecting continuum and discrete models with atomistic simulations. *Phys. Rev. B.* **74**, 024113.

72. Cho, J., Molinari & J. –F., Anciaux, G., 2017. Mobility law of dislocations with several character angles and temperatures in FCC aluminum. *Int. J. Plast.* **90**, 66-75.

73. Landau, L. D. & Lifshitz, E. M., 1976. *Mechanics, Course of Theoretical Physics*, vol. 1 Butterworth-Heinemann, Oxford.

74. Gillis, P. P. & Kratochvil, J. 1970. Dislocation acceleration. *Philos. Mag. A* **21**, 425-432.

75. Gurrutxaga-Lerma, B., Balint, D. S., Dini, D., Eakins, D. E. & Sutton, A. P. 2013. A dynamic discrete dislocation plasticity method for the simulation of plastic relaxation under shock loading. *Proc. R. Soc. A* **469**, 20130141.

76. Gurrutxaga-Lerma, B., 2016. The role of the mobility law of dislocations in the plastic response of shock loaded pure metals. *Model. Simul. Mater. Sci. Eng.* **24**, 065006.

77. Blaschke, D. N., 2019. Velocity dependent dislocation drag from phonon wind and crystal geometry. *J. Phys. Chem. Solids.* **124**, 24-35.

78. Li., Q. & Shi, S.-Q., 2002. Dislocation jumping over the sound barrier in tungsten. *Appl. Phys. Lett.* **80**, 3069-3071.

79. Pellegrini, Y. –P., 2014. Equation of motion and subsonic-transonic transitions of rectilinear edge dislocations: A collective-variable approach. *Phys. Rev. B* **90**, 054120.

80. Lazar, M., Pellegrini, Y. –P., 2016. Distributional and regularized radiation fields of non-uniformly moving straight dislocations and elastodynamic Tamm problem. *J. Mech. Phys. Solids.* **96**, 632-659.

81. Lifshitz, I. M. & Kosevich, A. M., 1966. The dynamics of a crystal lattice with defects. *Rep. Prog. Phys.* **29**, 217-254.

82. Montroll, E. W. & Potts, R. B., 1955. Effect of defects on lattice vibrations. *Phys. Rev.* **100**, 525-543.

83. Maradudin, A. A., Mazur, P., Montroll, E. W. & Weiss, G. H., 1958. Remarks on the vibrations of diatomic lattices. *Rev. Mod. Phys.* **30**, 175-196.

84. Mills, M. J. & Stadelmann, P., 1989. A study of the structure of Lomer and 60° dislocations in aluminium using high-resolution transmission electron microscopy. *Phil. Mag. A* **60**, 355-384.

85. Srinivasan, S. G., Liao, X. Z., Baskes, M. I., McCabe, R. J., Zhao, Y. H. & Zhu, Y. T., 2005. Compact and dissociated dislocations in aluminum: Implications for deformation. *Phys. Rev. Lett.* **94**, 125502.

86. Tang, Y., 2018. Uncovering the inertia of dislocation motion and negative mechanical response in crystals. *Sci. Rep.* **8**, 140.

87. Mishin, Y., Farkas, D., Mehl, M. J. & Papaconstantopoulos, D. A., 1999. Interatomic potentials for monoatomic metals from experimental data and *ab initio* calculations. *Phys. Rev. B* **59**, 3393.

88. Mishin, Y., Mehl, M. J., Papaconstantopoulos D. A., Voter, A. F. & Kress, J. D., 2001.

Structural stability and lattice defects in copper: *Ab initio*, tight-binding, and embedded-atom calculations. *Phys. Rev. B* **63**, 224106.

89. Angelo, J. E., Moody, N. R. & Baskes, M. I., 1995. Trapping of hydrogen to lattice defects in nickel. *Model. Simul. Mater. Sci. Eng.* **3**, 289-307.

90. Ackland, G. J. Tichy, G., Vitek, V. & Finnis, M. W., 2006. Simple N-body potentials for the noble metals and nickel. *Phil. Mag. A* **56**, 735-756.

91. Wang, Z. Q. & Beyerlein, I. J., 2008. Stress orientation and relativistic effects on the separation of moving screw dislocations. *Phys. Rev. B* **77**, 184112.

92. Pellegrini, Y. –P., 2012. Screw and edge dislocations with time-dependent core width: from dynamical core equations to an equation of motion. *J. Mech. Phys. Solids* **60**, 227-249.

93. Hirth, J. P., Zbib, H. M. & Lothe, J., 1998. Forces on high velocity dislocations. *Model. Simul. Mater. Sci. Eng.* **6**, 165-169.

94. Chen, B., Lutker, K., Raju, S. V., Yan, J., Kanitpanyacharoen, W., Lei, J., Yang, S., Wenk, H.-R., Mao, H. & Williams, Q., 2012. Texture of nanocrystalline nickel: Probing the lower size limit of dislocation activity. *Science* **338**, 1448-1451.

95. Hughes, D. A. & Hansen, N., 2014. Exploring the limit of dislocation based plasticity in nanostructured metals. *Phys. Rev. Lett.* **112**, 135504.

96. Shan, Z., Stach, E. A., Wiezorek, J. M. K., Knapp, J. A., Follstaedt, D. M. & Mao, S. X., 2004. Grain boundary-mediated plasticity in nanocrystalline nickel. *Science* **305**, 654-657.

97. Li, R. & Chew, B. W., 2017. Grain boundary traction signatures: Quantifying the asymmetrical dislocation emission processes under tension and compression. *J. Mech. Phys. Solids* **103**, 142-154.

98. Quek, S., S., Chooi, Z. H., Wu, Z., Zhang, Y. W., Srolovitz, D., 2016. The inverse hall-petch relation in nanocrystalline metals: A discrete dislocation dynamics analysis. *J. Mech. Phys. Solids* **88**, 252-266.

99. Sanosoz, F. & Molinary, J. F., 2005. Mechanical behavior of $\sum$ tilt grain boundaries in nanoscale Cu and Al: A quasicontinuum study. *Acta. Mater.* **53**, 1931-1944.

100. Zhang, L., Lu, C., Tieu, K. & Shibuta, Y., 2018. Dynamic interaction between grain boundary and stacking fault tetrahedron. *Scr. Mater.* **144**, 78-83.

101. Lim, A. T., Haataja, M., Cai, W. & Srolovitz, D. J., 2012. Stress-driven migration of simple low-angle mixed grain boundaries. *Acta, Mater.* **60**, 1395-1407.

102. Du, H., Jia, C. –L., Houben, L., Metlenko, V., De Souza, R. A., Waser, R. & Mayer, J., 2015. Atomic structure and chemistry of dislocation cores at low-angle tilt grain boundary in $SrTiO_3$ bicrystals. *Acta. Mater.* **89**, 344-351.

103. Gu, Y., Xiang, Y., Srolovitz, D. J., El-Awady, J. A., 2018. Self-healing of low angle grain boundaries by vacancy diffusion and dislocation climb. *Scr. Mater.* **155**. 155-159.

104. Kim, S. I., Lee, K. H., Mun, H. A., Kim, H. S., Hwang, S. W., Roh, J. W., Yang, D. J., Shin. W. H., Li, X. S., Lee, Y. H., Snyder, G. J. & Kim, S. W., 2015. Dense dislocation arrays embedded in grain boundaries for high-performance bulk thermoelectrics. *Science* **348**, 109-114.

105. Yasaei, P., Fathizadeh, A., Hantehzadeh, R., Majee, A. K., El-Ghandour, A., Estrada, D., Foster, C., Aksamija, Z., Khalili-Araghi, F. & Salehi-Khojin, A., 2015. Bimodal phonon scattering in graphene grain boundaries. *Nano Letters* **15**, 4532-4540.

106. Sutton, A. P. & Balluffi, R. W., 1995. *Interfaces in Crystalline Materials*, Oxford University Press.

107. Winning, M., Rollett, A. D., Gottstein, G., Srolovitz, D. J., Lim, A. & Shvindlerman, L. S., 2010. Mobility of low-angle grain boundaries in pure metals. *Phil. Mag.* **90**, 3107-3128.

108. Read, W. T. & Shockley, W., 1950. Dislocation models of crystal grain boundaries. *Phys. Rev.* **78**, 275-289.

109. Hull, D. & Bacon, D. J., 2011. *Introduction to dislocations*, 5th Ed., Elsevier.

110. Brailsford, A. D., 1966. Stress field of a dislocation. *Phys. Rev.* **142**, 383-387.

111. Brailsford, A. D., 1966. Effective mass of a dislocation. *Phys. Rev.* **142**, 388-391.

112. Sakamoto, M., 1991. High-velocity dislocations: Effective mass, effective line tension and multiplication. *Phil. Mag. A* **63**, 1241-1248.

113. Eshelby, J. D., 1962. The interaction of kinks and elastic waves. *Proc. Roy. Soc. A* **266**, 222-246.

114. Kim, H. –S, Kang, S. D., Tang, Y., Hanus, R. & Snyder, G. J., 2016. Dislocation strain as the mechanism of phonon scattering at grain boundaries. *Mater. Horizons* **3**, 234-240.

115. Eshelby, J. D.,1951. The force on an elastic singularity. *Phil. Trans. Roy. Soc. A* **244**, 87-112.

116. Rice, J. R., 1968. A path-independent integral and the approximate analysis of strain concentrations by notes and cracks. *J. Appl. Mech* **35**, 379-388

117. Eshelby, J. D., 1956. The continuum theory of lattice defects. *Solid State Phys.* **3**, 79-144.

118. Noether, E., 1971. Invariant variation problems. *Transp. Theory. Stat. Phys.* **1**, 186-207.

119. Lubarda, V. A. & Markenscoff, X., 2007. Configurational force on a lattice dislocation and the Peierls stress. *Arch. Appl. Mech.* **77**, 147-154.

120. Lubarda, V. A., 2015. Determination of interaction forces between parallel dislocations by the valuation of *J* integrals of plane elasticity. *Cont. Mech. Therm.* **28**, 391-405.

121. Seo, Y., Jung, G.-Y., Kim, I.-H. & Pak, Y. E., 2018. Configurational forces on elastic line singularities. *J. Appl Mech.* **85**, 034501.

122. Baxevanakis, K. P. & Giannakopoulos, A E., 2015. Finite element analysis of discrete edge dislocations: Configurational forces and conserved integrals. *Int. J. Solids. Struct.* **62**, 52-65.

123. Ballarini, R. & Royer-Carfagni, G., 2016. A Newtonian interpretation of configurational forces on dislocations and cracks. *J. Mech. Phys. Solids* **95**, 602-620.

124. Nishioka, T. & Atluri, S. N., 1983. Path-independent integrals, energy release rates, and general solutions of near-tip fields in mixed-mode dynamic fracture mechanics. *Eng. Fract. Mech.* **18**, 1-22.

125. Maugin, G. A. & Trimarco, C., 1992. Pseudomomentum and material forces in nonlinear elasticity: variational formulations and application to brittle fracture. *Acta Mech.* **94**, 1-28.

126. Ni, L. & Markenscoff, X., 2008. The self-force and effective mass of a generally accelerating dislocation I: Screw dislocation. *J. Mech. Phys. Solids* **56**, 1348-1379.

127. Stroh, A. N., 1962. Force on a moving dislocation. *Phys. Rev.* **128**, 55-61.

128. Simha, N. K., Fischer, F. D., Shan, G. X., Chen, C. R. & Kolednik, O., 2008. *J*-integral and crack driving force in elastic-plastic materials. *J. Mech. Phys. Solids* **56**, 2876-2895.

129. Lothe, J., 1961. Lorentz force on screw dislocations and related problems. *Phys. Rev.* **122**, 78-82.

130. Kosevich, A. M., 1965. Dynamical theory of dislocations. *Sov. Phys. Usp.* **7**, 837-854.

131. Ninomiya, T., 1972. A theory of dislocation motion in a crystal. I. General and application to one-dimensional lattice. *J. Phys. Soc. Jpn.* **33**, 921-928.

132. Slepyan, L. I., 2001. Feeding and dissipative waves in fracture and phase transition. I. Some 1D structures and a square-cell lattice. *J. Mech. Phys. Solids.* 49, 469-511.

133. Agiasofitou, E. & Lazar, M., 2017. Micromecchanics of dislocations in solids: ***J***-, *M*-, and ***L***-integrals and their fundamental relations. *Int. J. Eng. Sci.* **114**,16-40.

134. Budiansky, B. & Rice, J. R., 1973. Conservation laws and energy-release rates. *J. Appl. Mech.* **40**, 201-203.

135. Sun, X.-Y., Cordier, P., Taupin, V., Fressengeas, C. & Karki, B. B., 2017. Continuous description of grain boundaries using crystal defect fields: the example of a {310}/[001] tilt boundary in MgO. Eur. J. Mineral. **29**, 155-165.

136. Holland, V. F. & Lindenmekyer, P. H., 1965. Direct observation of dislocation networks in folded-chain crystals of polyethylene. J. Appl. Phys. **36**, 3049-3056.

137. Marcinkowski, M. J. & Brown, N. 1961. Theory and direct observation of dislocations in the Fe_3Al supperlattices. Acta. Metall. **9**, 764-786.

Table 3.1. Input parameters to solve Eq. (3.16) and Eq. (3.31) for the 2D LJ triangular lattices at 0 K. Parameters in shaded cells were obtained phenomenologically by fitting the solutions of Eq. (3.16) to MD simulation results. Other parameters were derived by the formulas introduced in the main text or directly measured from the simulation results.

Parameter	$0.5\varepsilon_0$	$1.0\varepsilon_0$	$2.0\varepsilon_0$	$3.0\varepsilon_0$
b [Å]		2.545		
w_0 [$\times 10^{13}\mathrm{s}^{-1}$]	5.21	7.37	10.42	12.76
Ω [$\times 10^{13}\mathrm{s}^{-1}$]	19.28	27.26	38.55	47.22
C_t [km/s]	2.09	2.95	4.18	5.12
Φ_{dis}		4.21		
M_{dis} [m/(s · GPa)]	102	70	48	38
η	0.073	0.069	0.067	0.066
C_1^{dis}	0.0168	0.0159	0.0154	0.0152
C_2^{dis}	1.1379	1.0756	1.0444	1.0288
σ_P [GPa]	2.0	3.5	7.0	10.0
B_0 [$\times 10^{-3}$Pa · s]	2.496	3.884	5.239	6.656

Table 3.2. Input parameters used to solve Eq. (3.16) for perfect and extended edge dislocations in cubic crystals at 0 K. Parameters in shaded cells were obtained phenomenologically by fitting the solutions of Eq. (3.16) to MD simulation results. Other parameters were derived by the linear elasticity theory or direct measurements of the MD simulation results.

Material	b [Å]	C_t [km/s]	$w_0[\times 10^{13}\mathrm{s}^{-1}]$	M_{dis} [km/(s · GPa)]	C_1^{dis}	C_2^{dis}
Fe	2.473	2.99	7.31	2.78	0.91	1.004
Mo	2.745	4.08	9.10	2.08	0.92	1.002
Al	2.864	3.22	6.89	6.13	0.96	1.04
Cu	2.556	2.15	5.07	3.67	0.96	1.03
Ni	2.489	2.89	7.00	3.78	0.97	1.02
Au	2.884	1.18	2.46	1.77	0.96	1.02

Table 3.3. Input parameters used to solve Eq. (3.16) for perfect and extended edge dislocations in cubic crystals at 300 K. Parameters in shaded cells were obtained phenomenologically by fitting the solutions of Eq. (3.16) to MD simulation results. Other parameters were derived by the linear elasticity theory or direct measurements of the MD simulation results. Here, $C_t(=\sqrt{G/\rho})$ is not included because the changes in shear modulus and density of the crystals are so small that there is no significant difference in C_t compared to that at 0 K.

Material	$w_0[\times 10^{13}\mathrm{s}^{-1}]$	M_{dis} [km/(s · GPa)]	C_1^{dis}	C_2^{dis}
Fe	6.94	4.65	1.45	1.35
Mo	8.70	3.00	1.55	1.30
Al	6.76	16.24	1.28	1.30
Ni	6.76	14.95	2.55	1.90

Table 4.1. Input parameters used to solve Eq. (4.6) for LAGBs at 0 K. Parameters in shaded cells were obtained phenomenologically by fitting the solutions of Eq. (4.6) to MD simulation results. Here, w_0 and M_{dis} were obtained by MD simulations of perfect lattice and single edge dislocations by using the LJ potential of $\varepsilon = \varepsilon_0$ with the same parameters, respectively. Since all the LAGBs used in this study consist of same edge dislocations, they share the same M_{dis}.

σ_{app}	$w_0[\times 10^{13}\mathrm{s}^{-1}]$	M_{dis} [m/(s · GPa)]	C_1^{LAGB}	C_2^{LAGB}
5.60 GPa	7.37	70	85	0.175
6.02 GPa			84	0.180
6.88 GPa			83	0.185
7.30 GPa			82	0.190

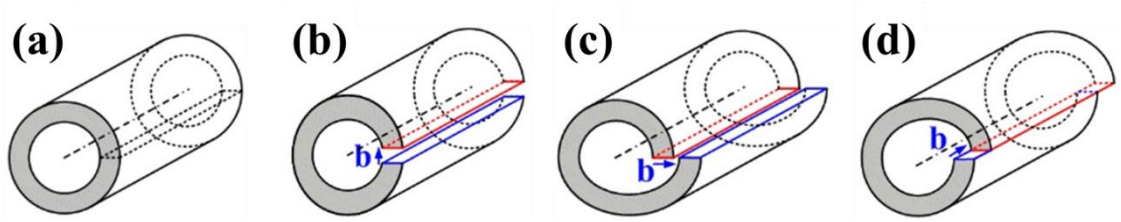

Figure 1.1. Volterra dislocation models[135]. A solid-dotted line across the center of cylinder represents the dislocation line and a dashed rectangle in each figure corresponds to the cut plane. And **b** is Burgers vector. (a) A perfect system, (b) and (c) represent edge dislocations but different **b**, and (d) a scrwe dislocation.

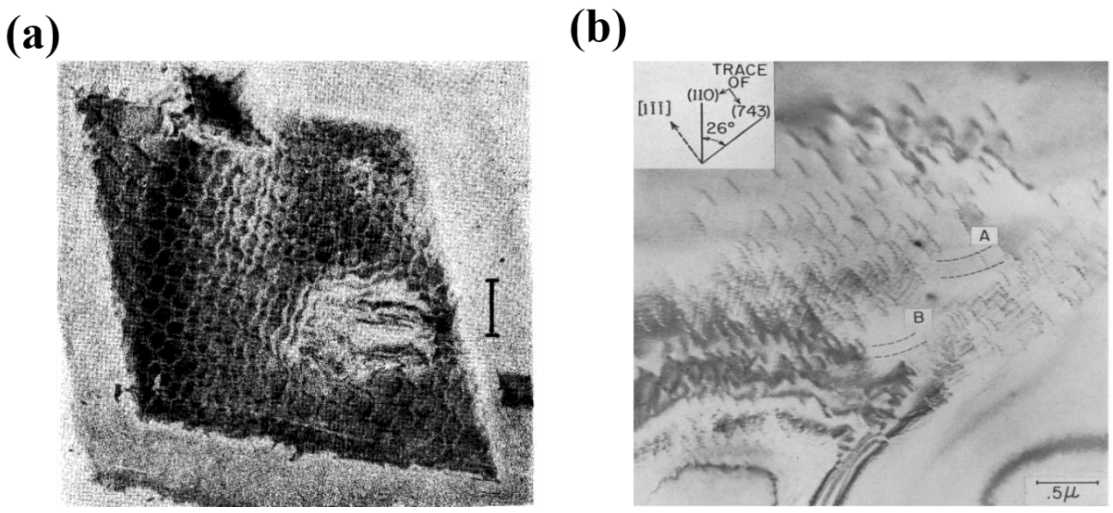

Figure 1.2. Direct observations of the dislocations . (a) The dislocation networks captured by diffraction contrast electron microscopy (Ref. (136)), and (b) a band of scrwe dislocations in Fe_3Al supperlattices captured by transmission electron microscopy (Ref. (137)).

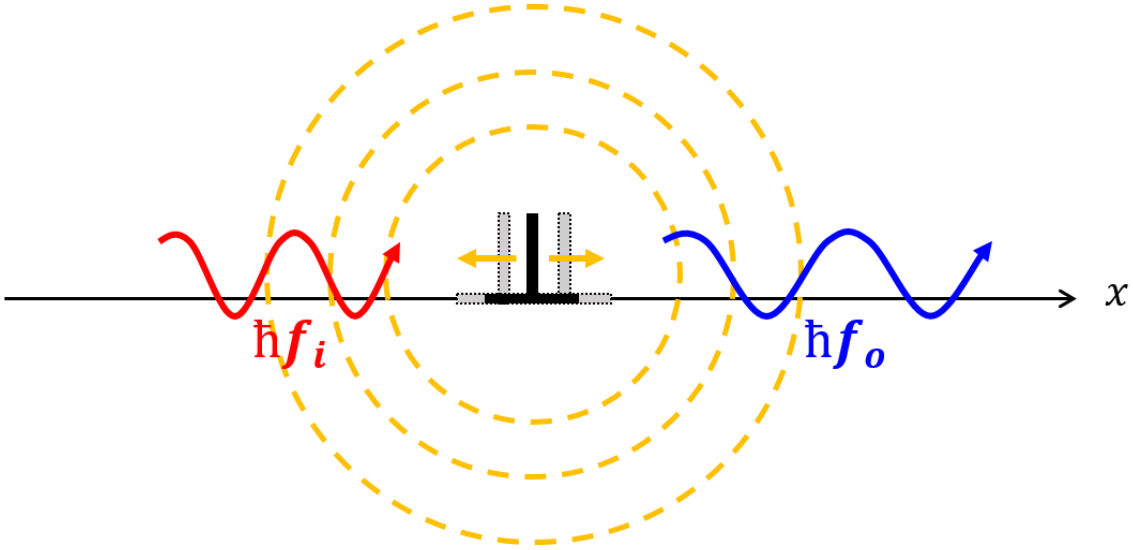

Figure 1.3. The phonon whose frequency is f_i impinge to the moving dislocation. This results in the dislcoation oscillation and secondary waves are emitted from the dislocaiton core as shwon in yellow dashed curve. Thus, the incomping phonon is scattered and outcome phonon has frequency f_o.

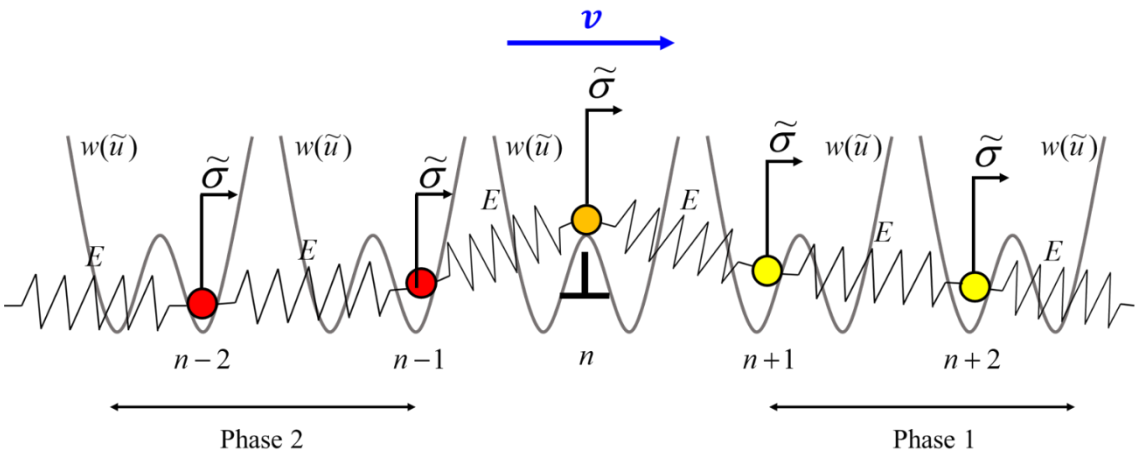

Figure 1.4. One-dimensional atomic chain to describe the dislocation motion. All atoms are attached to a rigid substrate and the interaction between atom and substrate follows bi-harmonic potential $w(\tilde{u})$. And the interaction bewteen atoms is described by Hooke's law. As the dislocation glides towards positive x direction under applied stress $\tilde{\sigma}$, the atoms that were initially at phase 1 move to the neigboring Peierls valley, or phase 2.

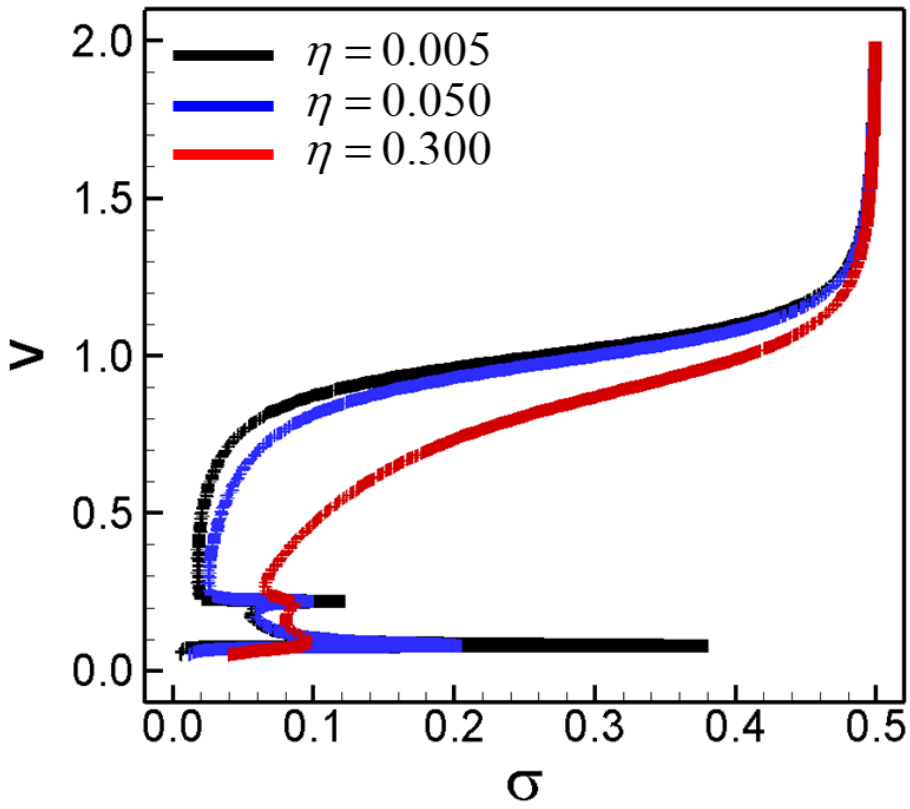

Figure 1.5. The relationship bewteen the normalized stress and normalized dislocation velocity with variable damping coefiicients. Here, the radiation drag is the dominant drag mechanism during the dislocation motion.

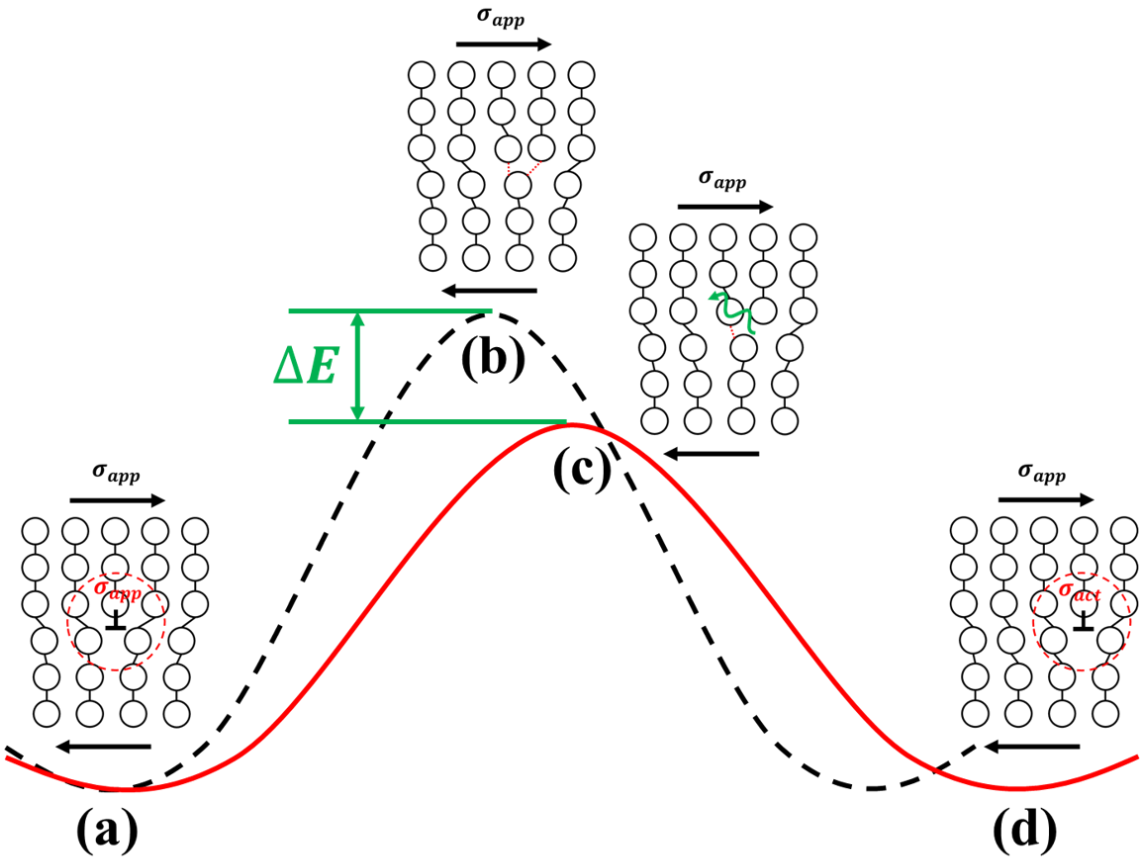

Figure 2.1. Potential energy change during the dislocation motion. Black dashed curve represents an ideal Peierls valley without energy dissipation and red solid one represents an actual Peierls valley with the energy dissipation, ΔE. Ideally, the dislocation at (a) initial state moves to (b) transition state under applied stress σ_{app}. However, an atomic bond inside the dislocation core breaks, which results in energy dissipation. Thus, the dislocation core reaches to the transient state (c). Finally, the dislocation moves to the neighboring Peierls valley as shown in (d). The energy dissipation leads to stress-drop from σ_{app} to σ_{act} around the dislocation core.

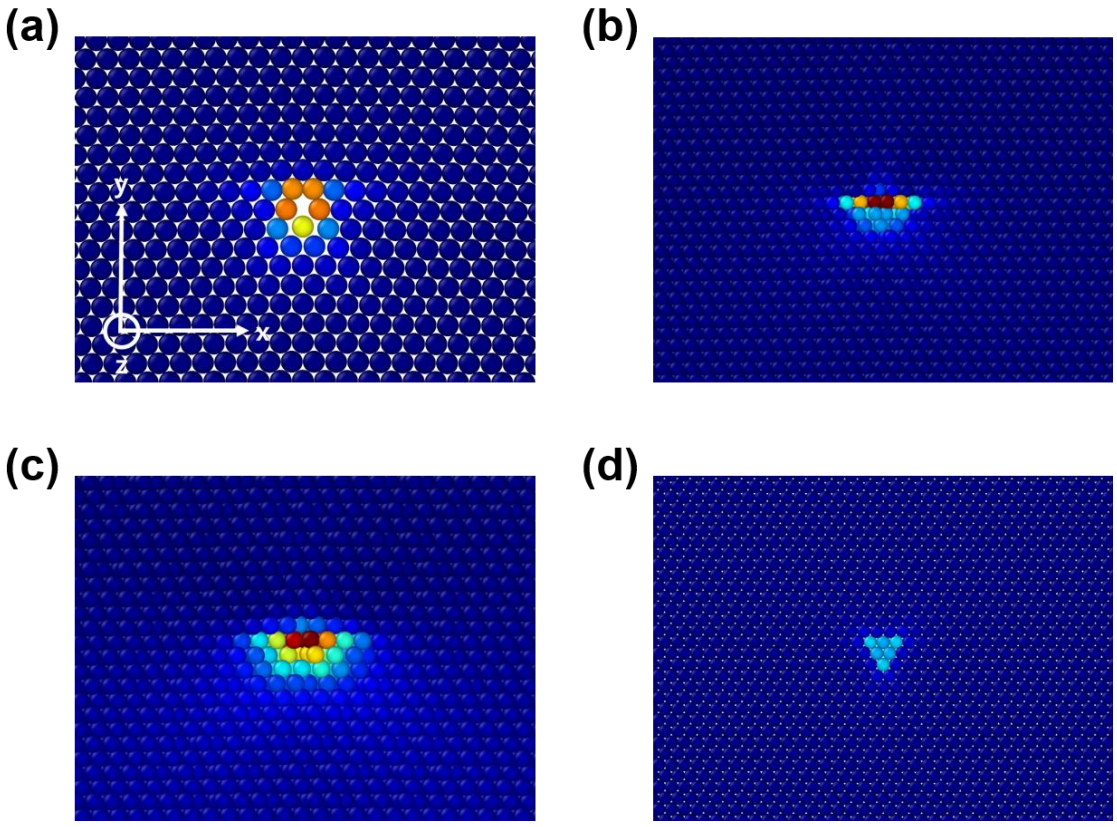

Figure 2.2. Equilibrium dislocation core structures at 0 K. Each figure corresponds to an edge dislocation in (a) 2D triangular lattice, (b) iron, and (c) molybdenum, respectively. And (d) is a screw dislocation in iron. Color represents a potential energy.

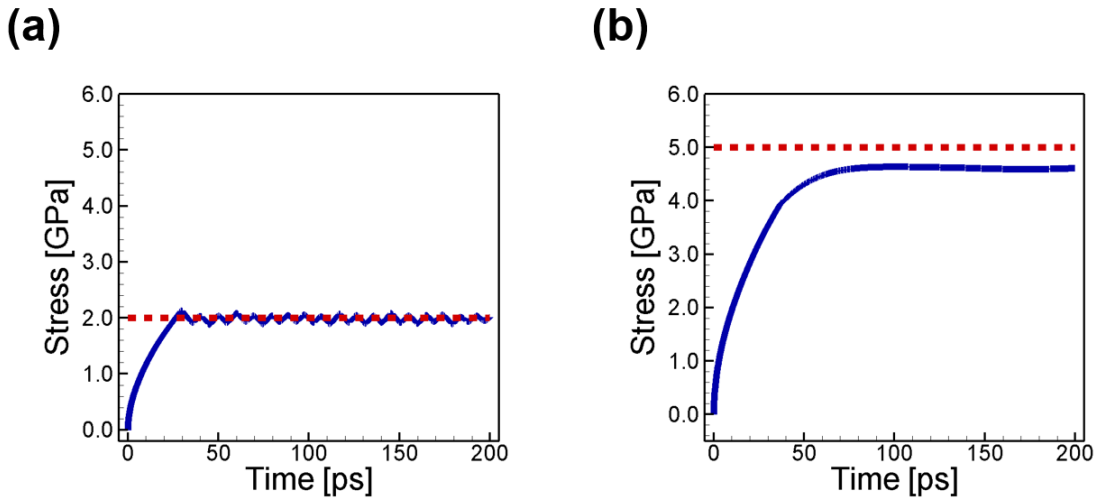

Figure 2.3. An average stress around of the edge dislocation core in the 2D triangular lattice of $\varepsilon = \varepsilon_0$ over time. Red dotted line represents σ_{app} and blue line represents the average stress, or actual stress σ_{act}, around the dislocation. Each figure corresponds to when (a) $\sigma_{app} = 2.0$ GPa, and (b) $\sigma_{app} = 5.0$ GPa.

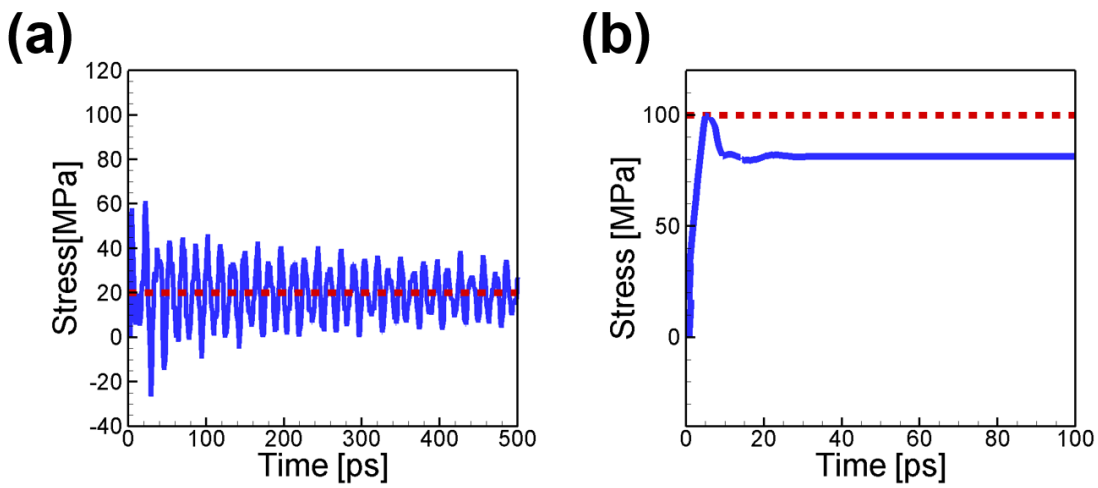

Figure 2.4. An average stress around of the edge dislocation core in iron nanoplate over time. Red dotted line represents σ_{app} and blue line represents actual stress σ_{act} around the dislocation. Each figure corresponds to when (a) $\sigma_{app} = 20$ MPa, and (b) $\sigma_{app} = 100$ MPa..

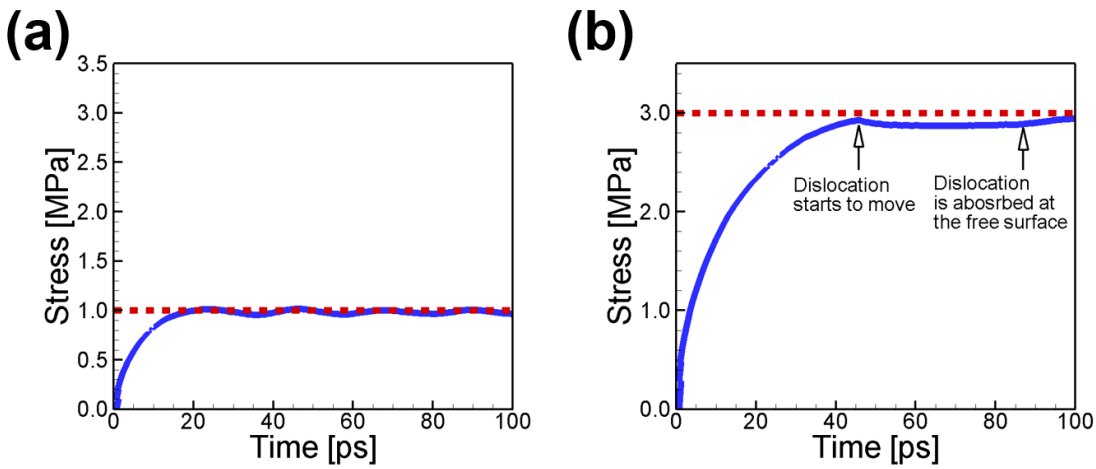

Figure 2.5. An average stress around of the screw dislocation core in iron nanowire over time. Red dotted line represents σ_{app} and blue line represents actual stress σ_{act} around the dislocation. Each figure corresponds to when (a) $\sigma_{app} = 1.0$ GPa, and (b) $\sigma_{app} = 3.0$ GPa.

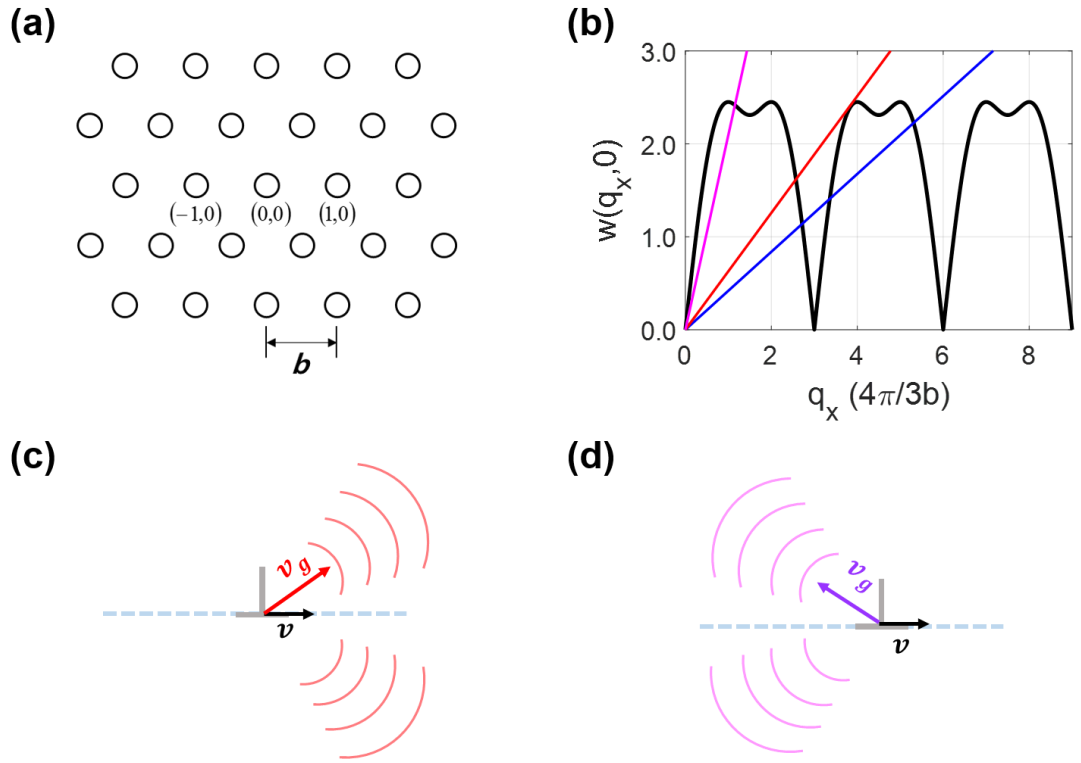

Figure 2.6. (a) An atomic structure of the triangular lattice. A center of the dislocation core is defined as the origin. (b) Black line represents a dispersion curve of the triangular lattice. And linear lines correspond to $w = q_x v$. Blue, red and purple lines are when $v = 0.10C_t, 0.15C_t,$ and $0.50C_t$, respectively. The excited waves are emitted whenever $w = q_x v$ intersects with the dispersion curve. (c) The *forward* wave emission with group velocity v_g from the dislocation whose speed is v. (d) The *backward* wave emission with group velocity v_g from the dislocation whose speed is v.

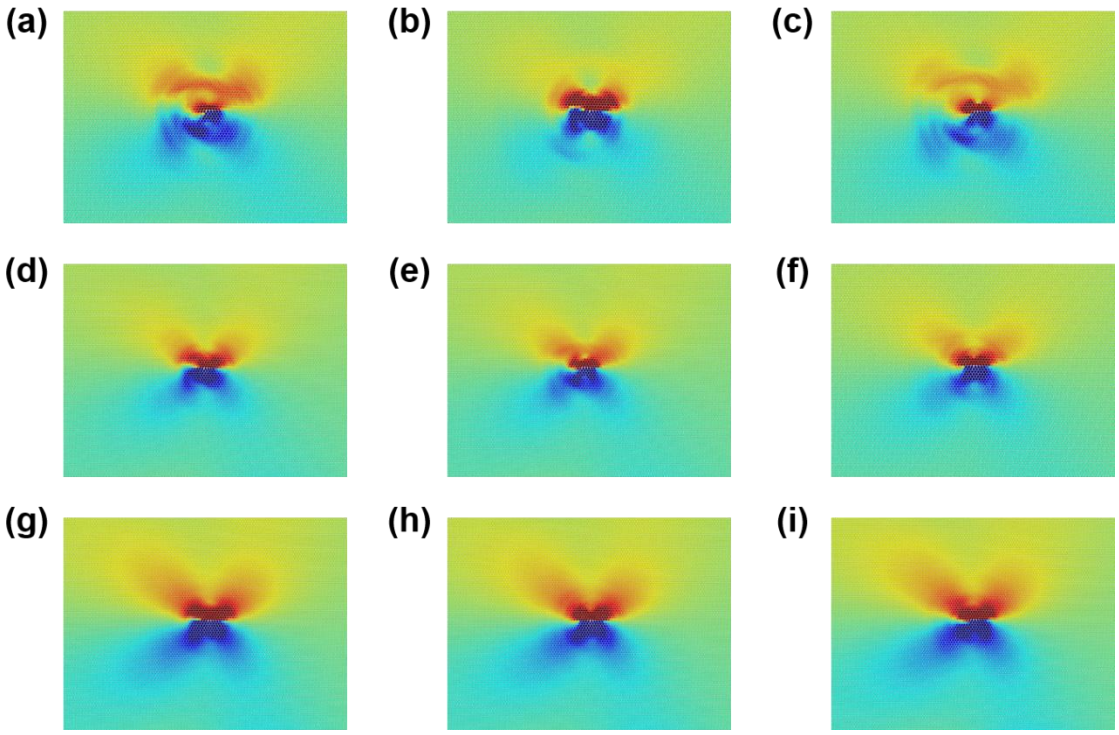

Figure 2.7. The simulation results of the emission of lattice waves from the moving edge dislocation in the 2D triangular lattice of $\varepsilon = 3.0\varepsilon_0$. Color represents a speed of atom in x direction. When $v = 0.135C_t$, the waves are emitted with changing time (a) $t = 99$ ps, (b) $t = 100$ ps, and (c) $t = 101$ ps. When $v = 0.171C_t$,, the waves are emitted with changing time (d) $t = 70$ ps, (e) $t = 71$ ps, and (f) $t = 72$ ps. And when $v = 0.189C_t$, the waves are emitted with changing time (g) $t = 152$ ps, (h) $t = 153$ ps, and (i) $t = 154$ ps.

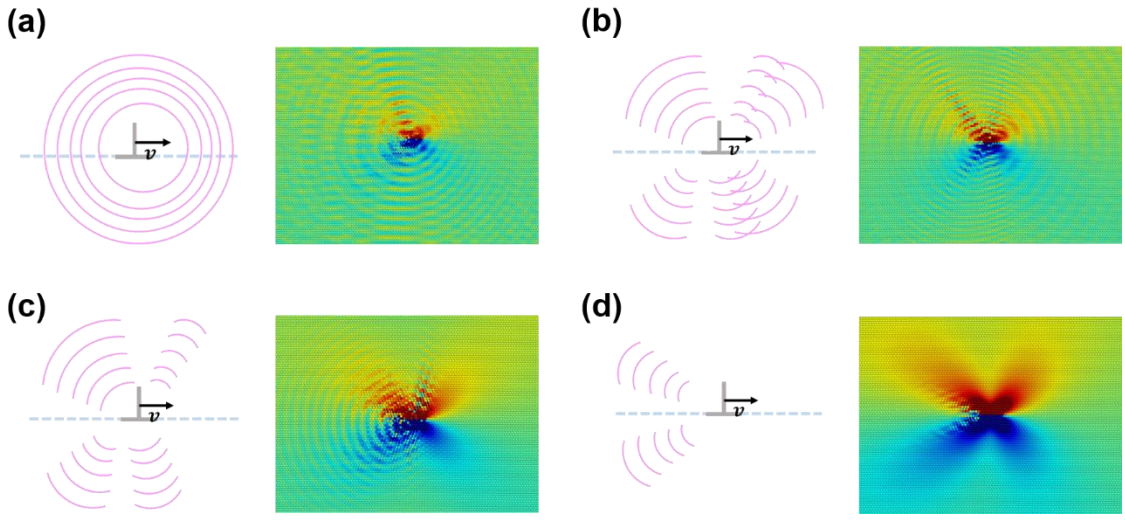

Figure 2.8. The simulation results of the emission of lattice waves from the moving edge dislocation in the molybdenum at 0 K and its graphical descriptions. Color represents a speed of atom in x direction. Each figure corresponds to when (a) $v = 0.049C_t$, (b) $v = 0.066C_t$, (c) $v = 0.104C_t$, and (d) $v = 0.246C_t$.

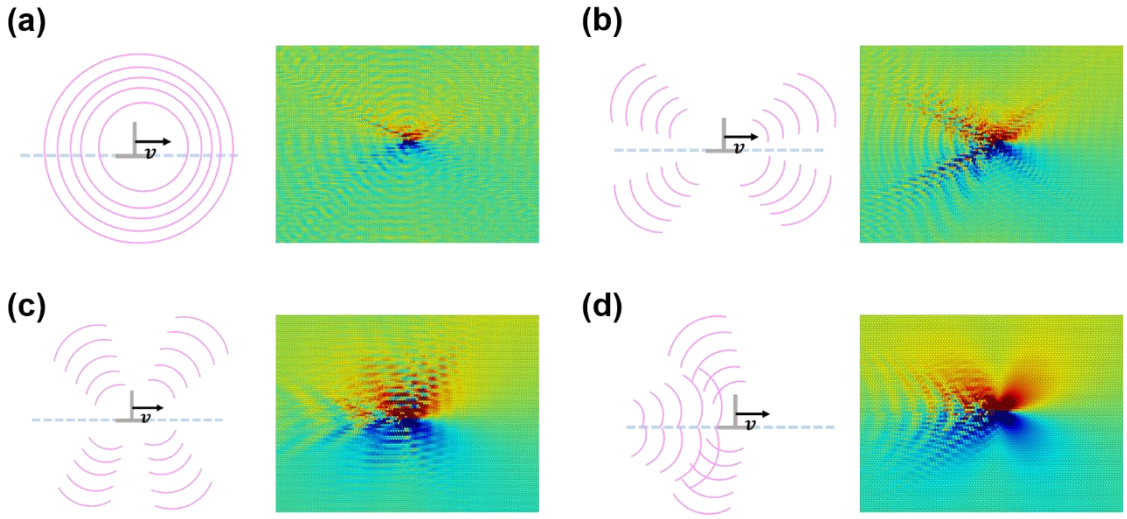

Figure 2.9. The simulation results of the emission of lattice waves from the moving edge dislocation in the iron at 0 K and its graphical descriptions. Color represents a speed of atom in *x* direction. Each figure corresponds to when (a) $v = 0.106C_t$, (b) $v = 0.199C_t$, (c) $v = 0.348C_t$, and (d) $v = 0.455C_t$.

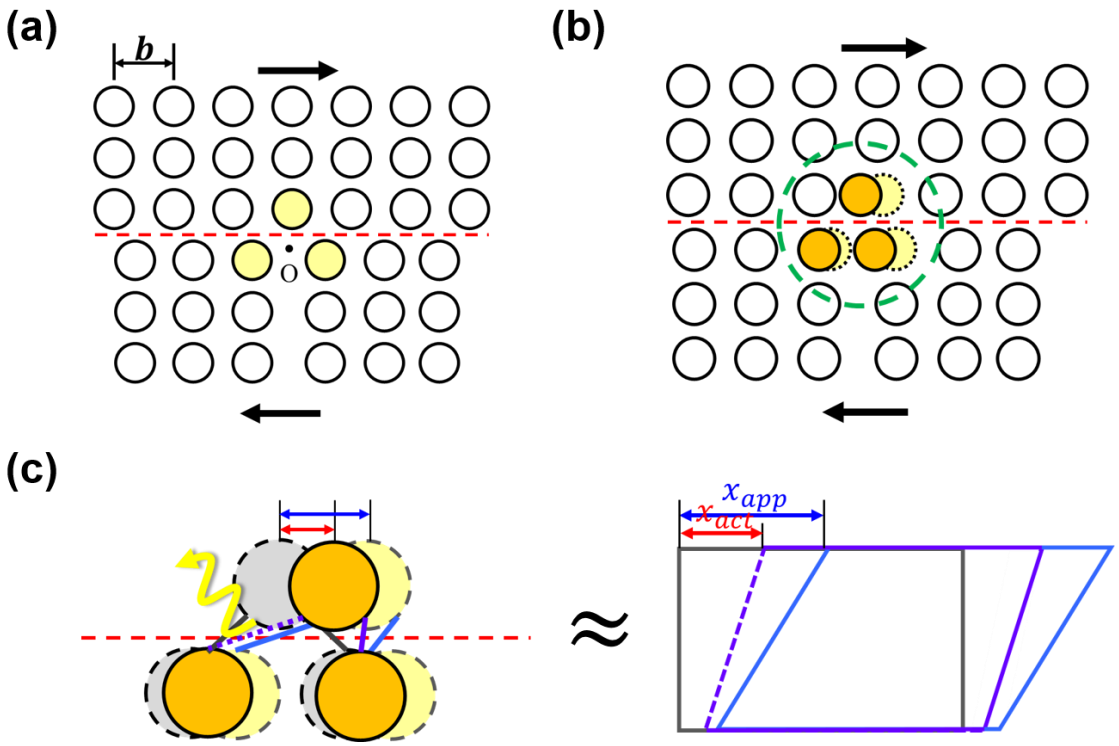

Figure 2.10. (a) Dislocation core when not moving, i.e., $\sigma_{app} < \sigma_P$. The core atoms are colored bright yellow. (b) Dislocation core when moving, i.e., $\sigma_{app} > \sigma_P$. As it moves, elastic waves emitted from the core are scattered and part of the energy dissipates from the core. As a result, the core retreats. The retreated core atoms are colored orange, and the scattering occurs within the region marked by the green dashed circle. (c) Enlarged view of the region within the green circle in (b), where gray atoms represent initial core atoms without any loading. As σ_{app} is applied, they deform to the bright yellow atoms. However, as phonon scattering, the core atoms retreat slightly. As a result, they finally deform to the orange-colored atoms. This process can roughly be described by simple shear deformation of the cell from a rectangular to parallelogram shape. Here, x_{app} is the ideal elongation due to σ_{app} if there is no scattering, and x_{act} is the actual elongation resulting from phonon scattering.

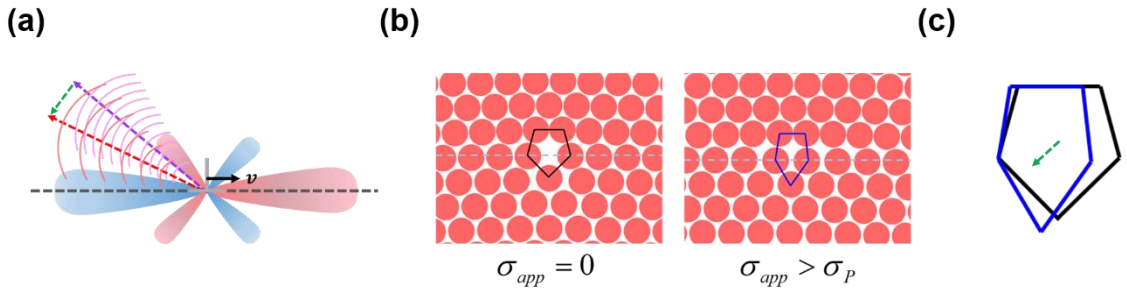

Figure 2.11. (a) Phonon scattering around the moving dislocation core. Purple arrow represents a lattice wave emitted from the dislocation core. And it is scattered by anharmonic strain field around the core. The scattered wave, which is shown by red arrow, has different frequency from it of the emitted wave and its propagating direction is changed. As a result, the dislocation core is pulled back, which is described by green arrow. (b) The equilibrium core structure when $\sigma_{app} = 0$ and $\sigma_{app} > \sigma_P$. (c) An enlarged description of the change of core structure when it moves. Because of the scattering (described by green arrow), the core structure during its motion is deformed by pulling back it from the stationary state.

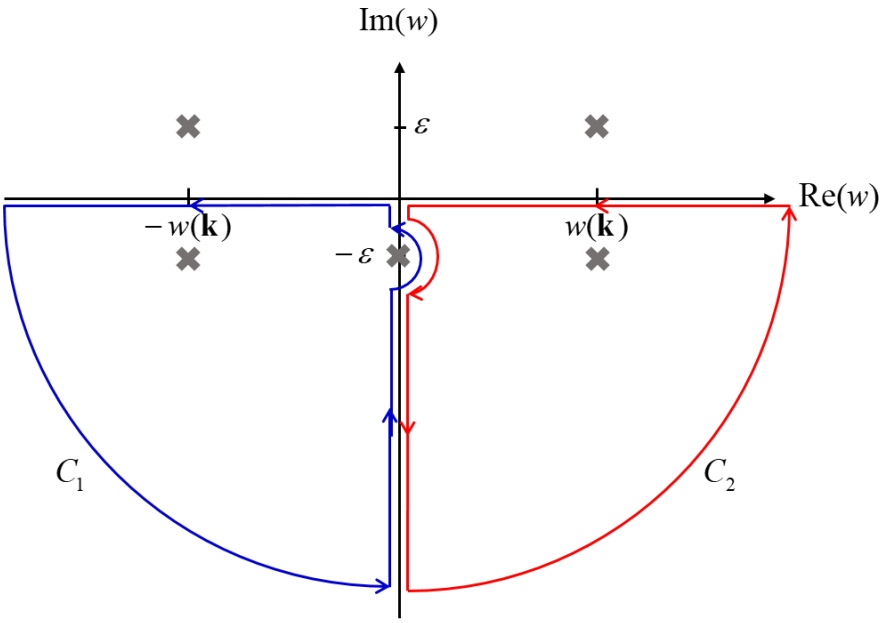

Figure 2.12. Integration path to calculate Eq. (2.6). Cross marks represent isolated poles, and blue and red paths represent contours C_1 and C_2, respectively.

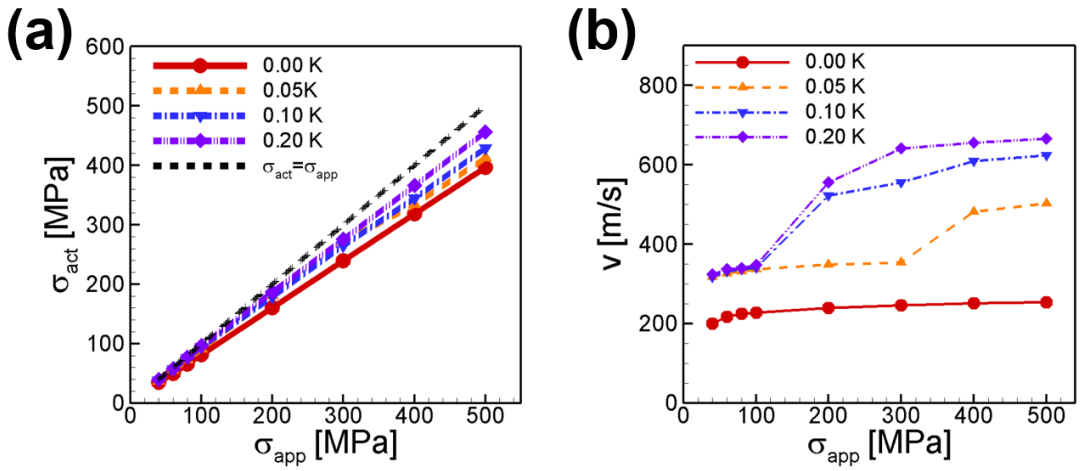

Figure 2.13. (a) MD simulation result showing the relation between σ_{app} and σ_{act} at various temperature and (b) the relation between σ_{app} and v at various temperatures for an edge dislocation while it glides in the iron nanoplate.

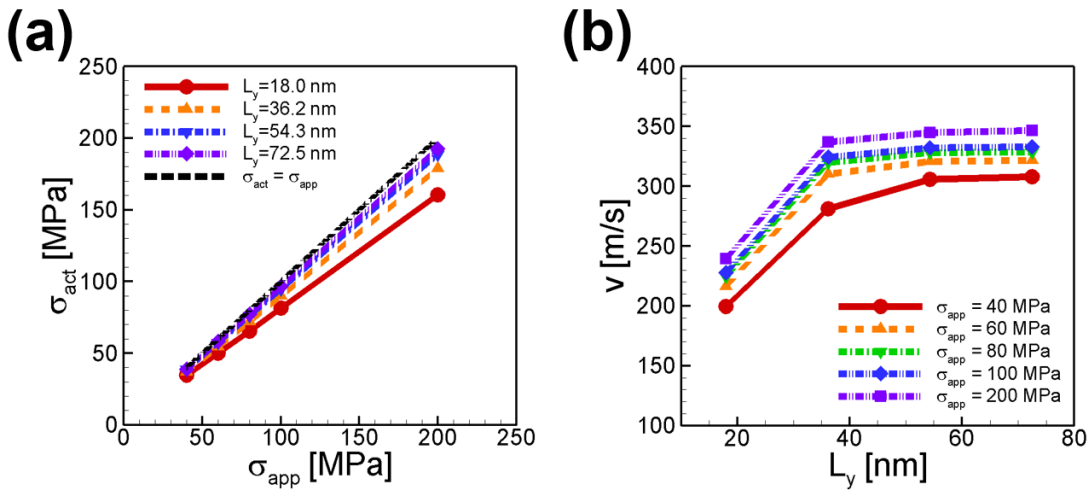

Figure 2.14. (a) MD simulation result showing the relation between σ_{app} and σ_{act} at various plate thicknesses (L_y) and (b) the relation between L_y and v at various σ_{app} for an edge dislocation while it glides in the iron nanoplate.

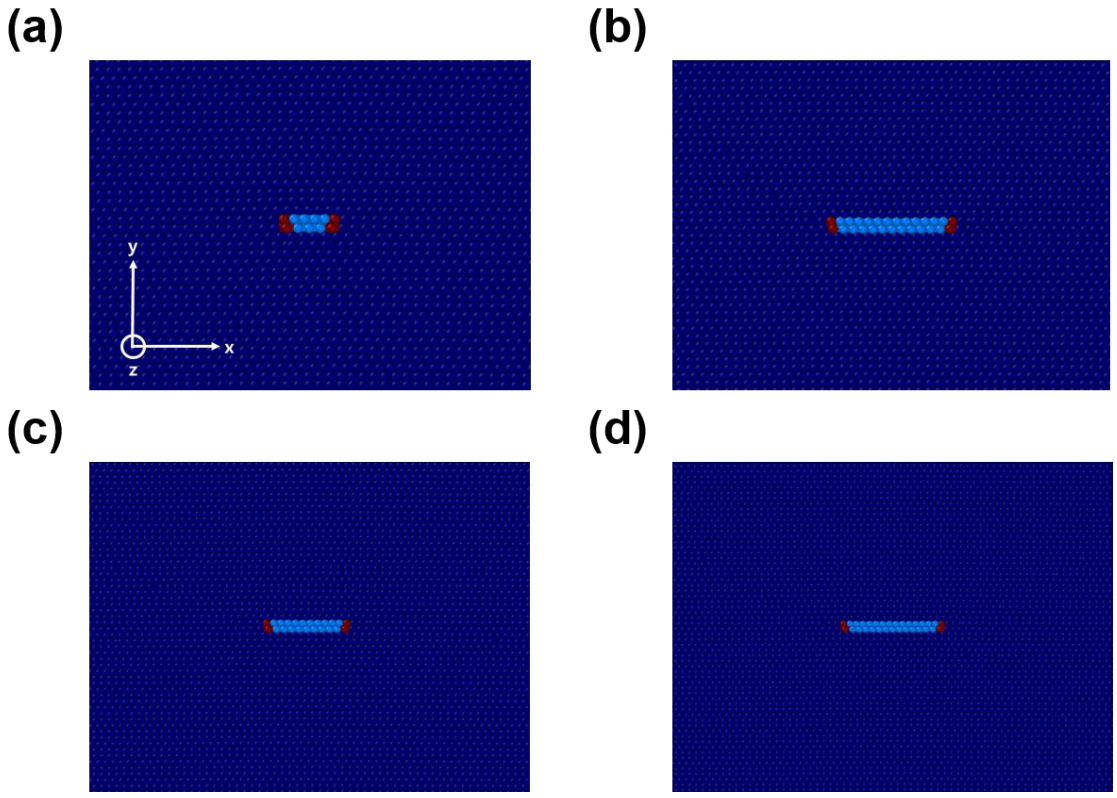

Figure 3.1. Equilibrium core structures of an extended edge dislocation in (a) aluminum, (b) copper, (c) nickel, and (d) gold at 0 K. Color represents a common neighbor analysis. Red atoms are partial dislocations, and light-blue atoms between red atoms are stacking faults.

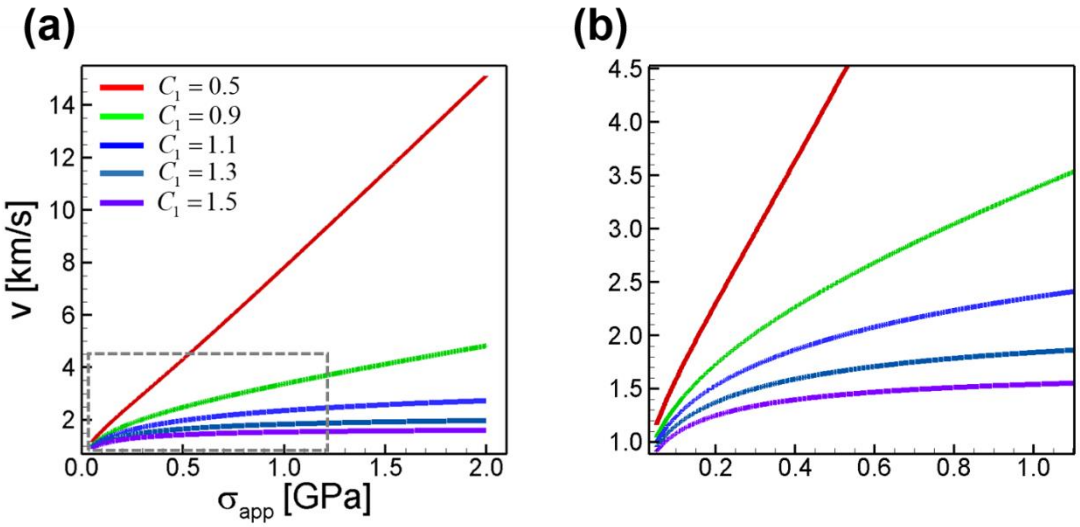

Figure 3.2. (a) Theoretical relationship between applied stress and dislocation speed obtained by solving Eq. (3.16) with changing C_1^{dis}. Here, we used the same input parameters used for nickel at 300 K, which are listed in Table 3.3, except with fixed $C_2^{dis} = 1.2$. (b) Enlarged graph of the gray rectangular area in (a).

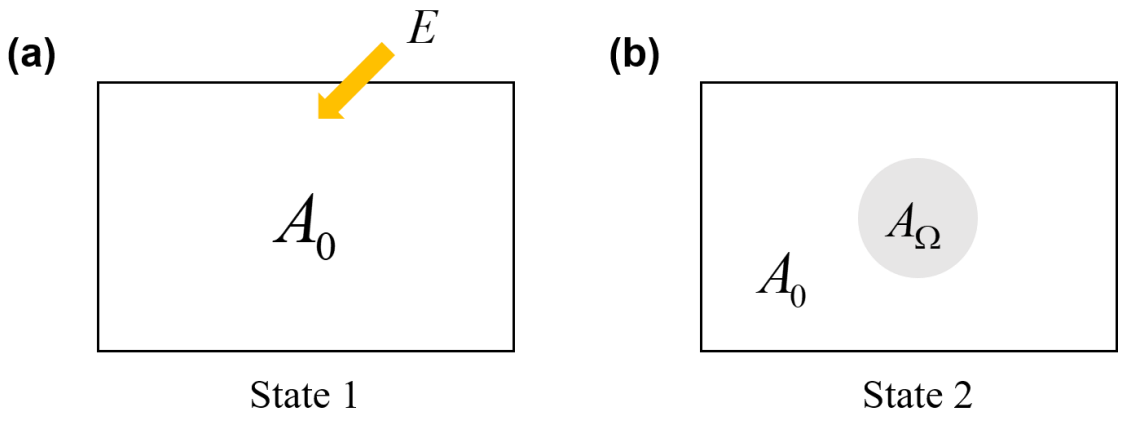

Figure 3.3. (a) A perfect system in which every atom oscillates with a natural frequency w_0 under externally supplied energy. (b) A defected system that consists of two isolated subsystems. A region denoted by gray color (A_Ω) corresponds to the defect and it consists of the atoms whose oscillation frequency is Ω. The remain consists of atoms whose frequency is w_0 without any defects.

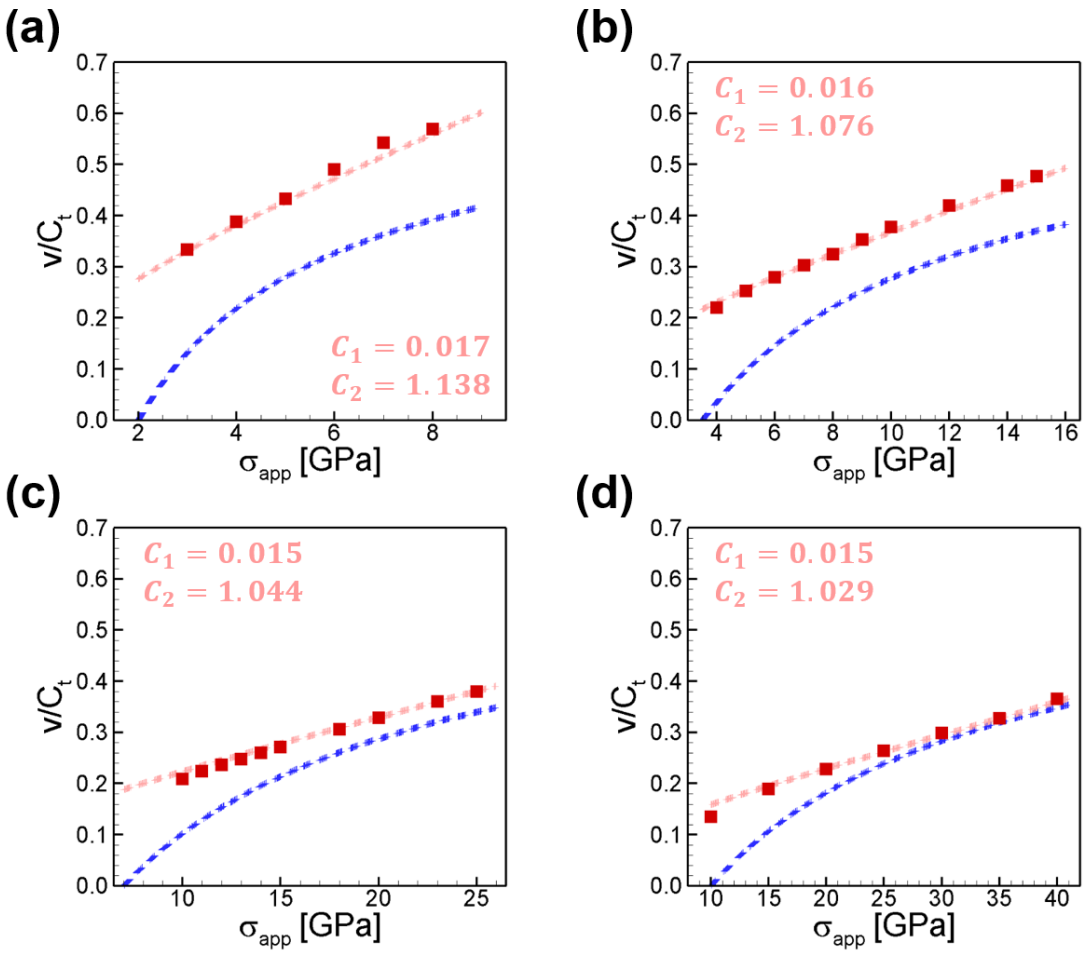

Figure 3.4. Relationship between applied stress and speed of dislocation for the LJ triangular lattices. In each figure, red square points represent the results of the MD simulation. And blue-dotted and light red-dotted lines are solutions obtained by the continuum theory (Eq. (3.31)) and the DLD theory (Eq. (3.16)), respectively. The group parameters C_1^{dis} and C_2^{dis} to solve Eq. (3.16) are provided in the figures. Each figure corresponds to when (a) $\varepsilon = 0.5\varepsilon_0$, (b) $\varepsilon = 1.0\varepsilon_0$, (c) $\varepsilon = 2.0\varepsilon_0$, and (d) $\varepsilon = 3.0\varepsilon_0$.

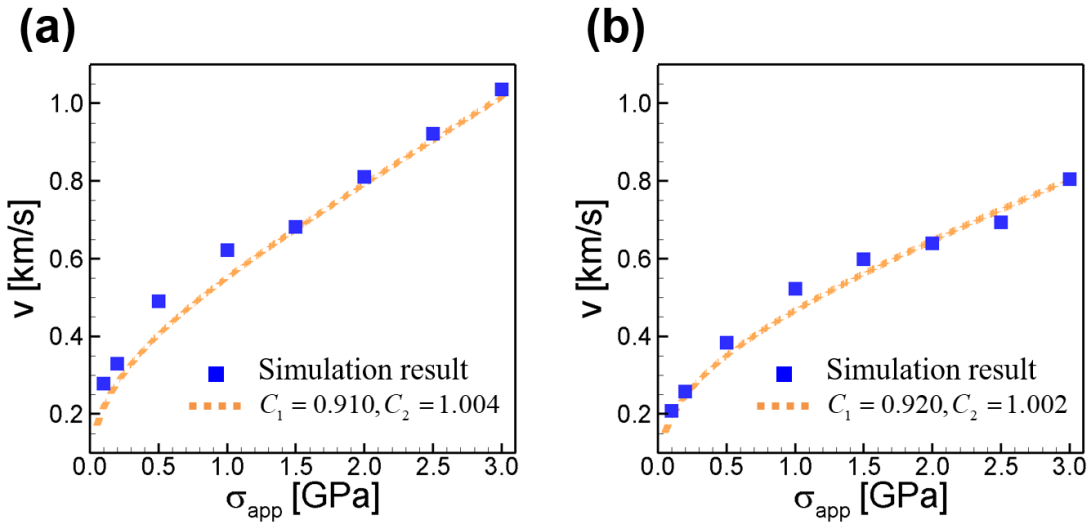

Figure 3.5. Relationship between applied stress and speed of a dislocation in (a) iron and (b) molybdenum at 0 K. Orange dashed lines correspond to solutions of Eq. (3.16) by inserting the input parameters listed in Table 3.2, and C_1^{dis} and C_2^{dis} are specified in each figure. Blue squares are results obtained by MD simulations.

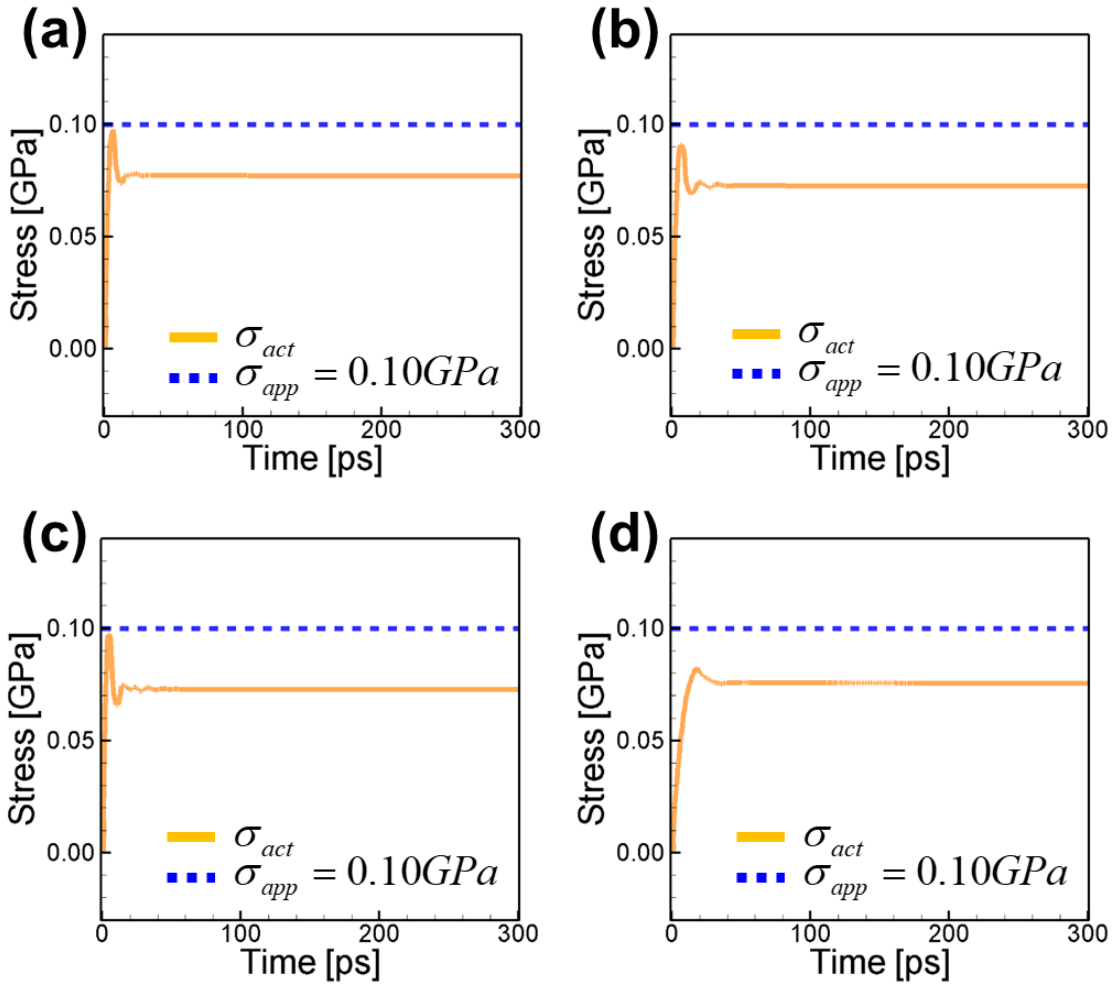

Figure 3.6. Variations in actual stress inside a system with a single extended edge dislocation over simulation time when $\sigma_{app} > \sigma_P$ is applied. Each figure corresponds to the dislocation motion in (a) aluminum, (b) copper, (c) nickel, and (d) gold.

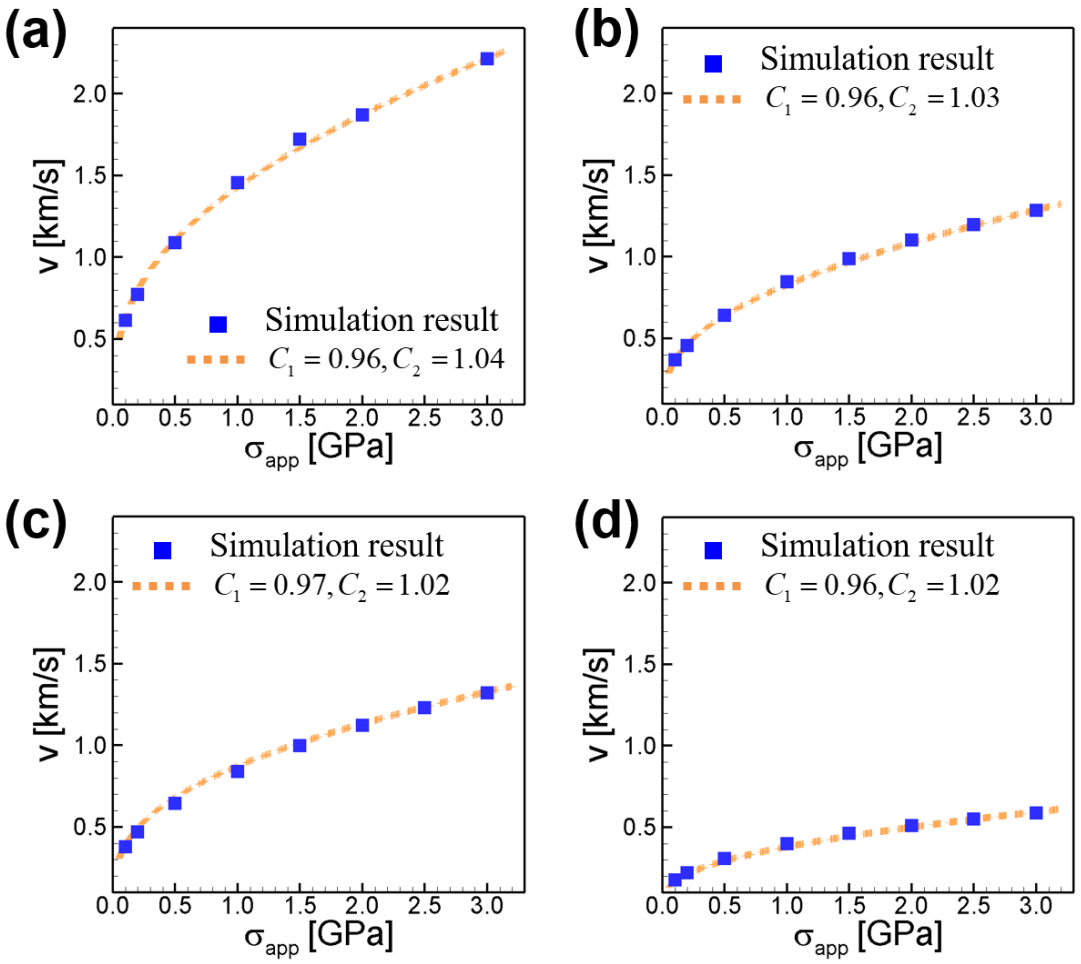

Figure 3.7. Relationship between applied stress and speed of an extended dislocation in (a) aluminum, (b) copper, (c) nickel, and (d) gold at 0 K. Orange dashed lines correspond to solutions of Eq. (3.16) obtained by inserting the input parameters listed in Table 3.2, and C_1^{dis} and C_2^{dis} are specified in each figure. Blue squares are results obtained by MD simulations.

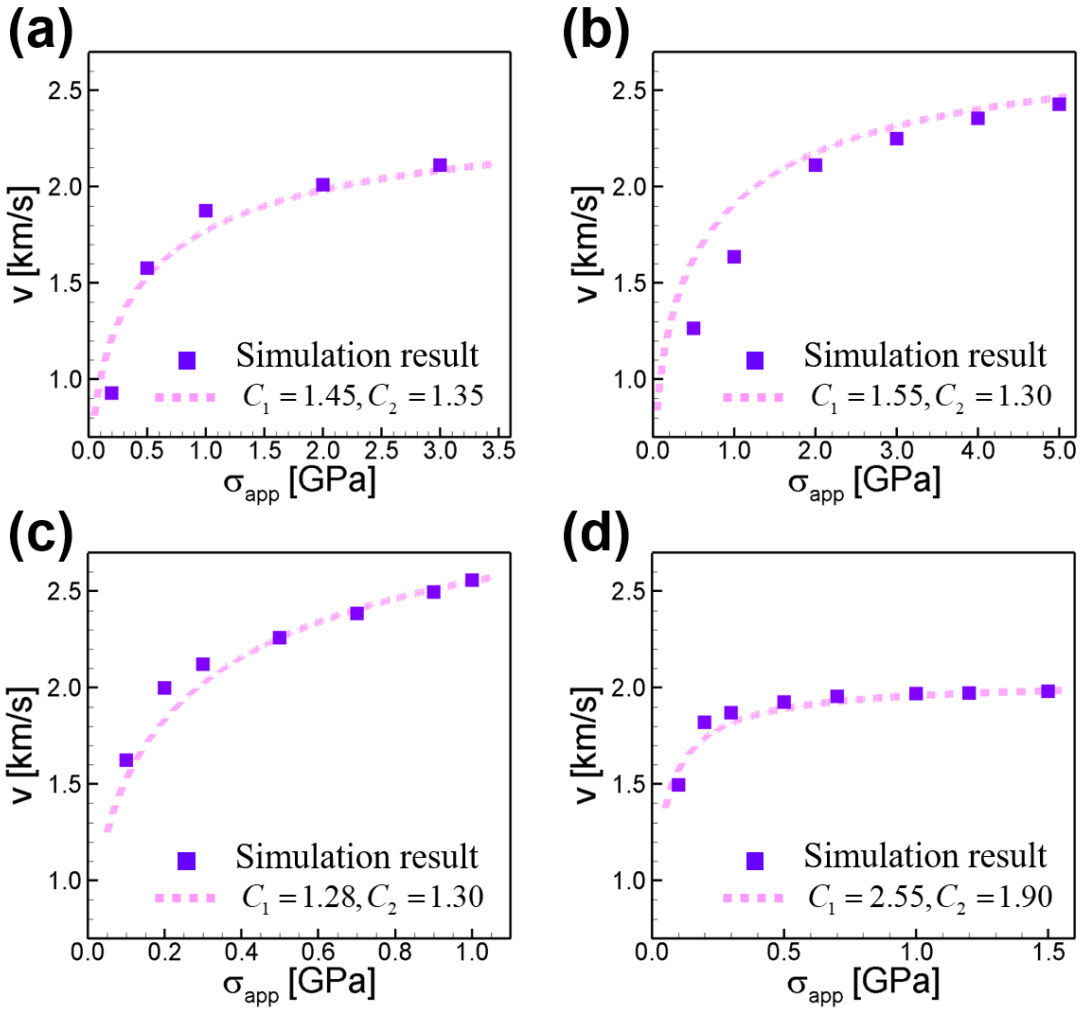

Figure 3.8. Relationship between applied stress and speed of an extended dislocation in (a) iron, (b) molybdenum, (c) aluminum, and (d) nickel at 300 K. Lavender dashed lines correspond to solutions of Eq. (3.16) obtained by inserting the input parameters listed in Table 3.3, and C_1^{dis} and C_2^{dis} are specified in each figure. Purple squares are results obtained by MD simulations.

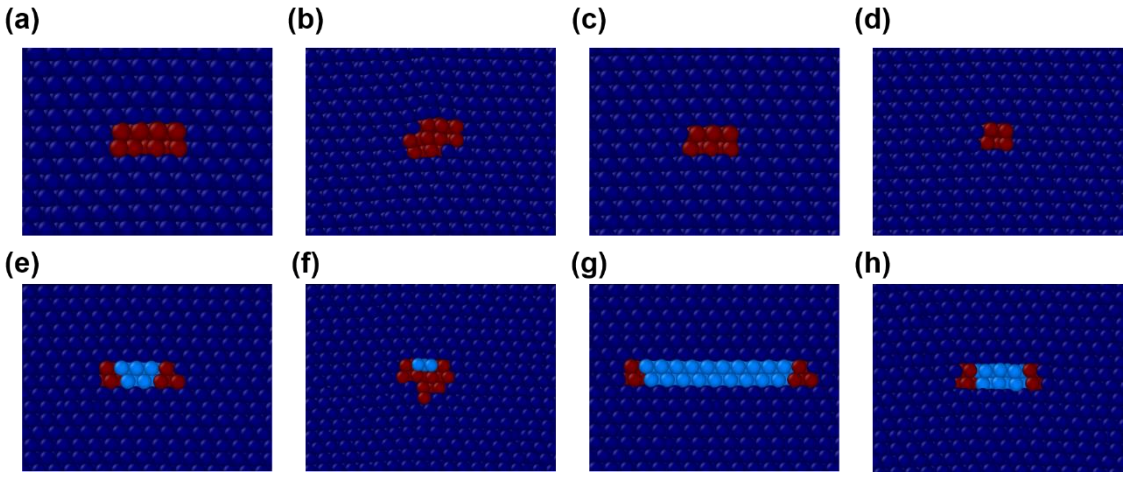

Figure 3.9. Structures of dislocation cores while in motion at 0 K and 300 K. Edge dislocation core in iron at (a) 0 K and (b) 300 K under $\sigma_{app} = 3.0\,GPa$. Edge dislocation core in molybdenum at (c) 0 K and (d) 300 K under $\sigma_{app} = 3.0\,GPa$. Extended edge dislocation core in aluminum at (e) 0 K and (f) 300 K under $\sigma_{app} = 1.0\,GPa$. Extended edge dislocation core in nickel at (g) 0 K and (h) 300 K under $\sigma_{app} = 1.5\,GPa$. Color represents a common neighbor analysis.

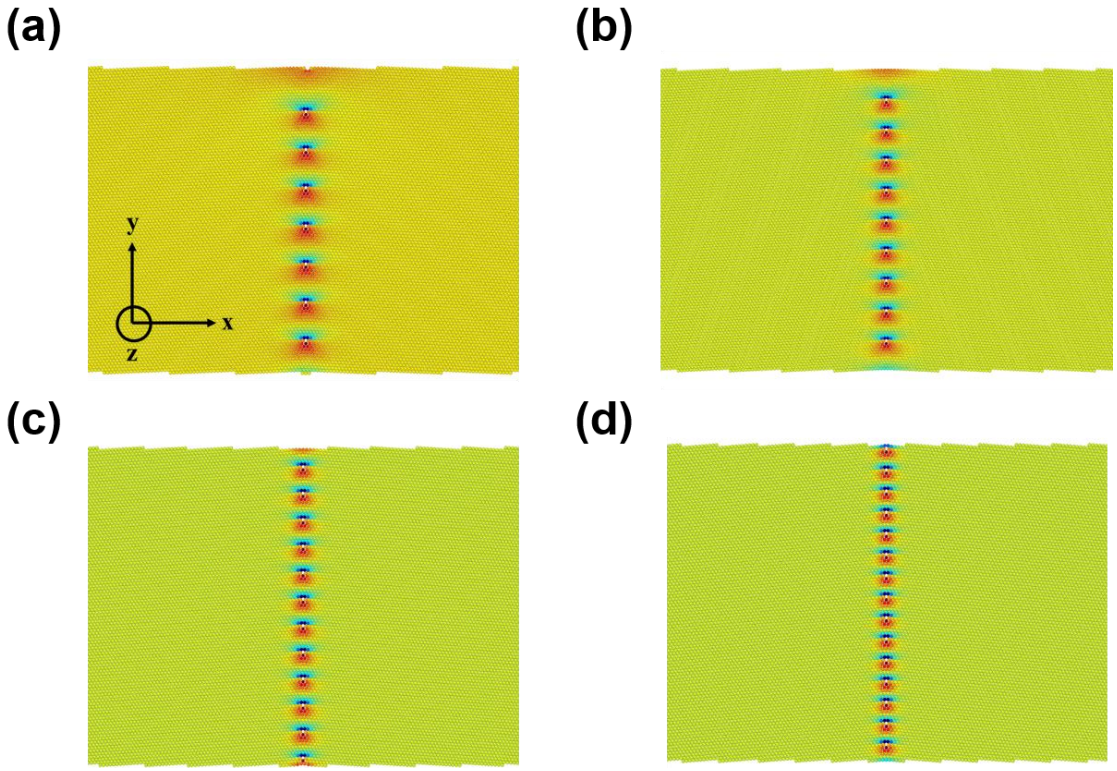

Figure 4.1. Equilibrium structures of symmetric tilt LAGBs at 0 K with misorientation angles of (a) $\theta = 5.09°$, (b) $\theta = 6.01°$, (c) $\theta = 7.34°$, and (d) $\theta = 9.42°$. Each LAGB consists of the same edge dislocations whose Burgers vector has only an *x* component. Color represents σ_{xx}.

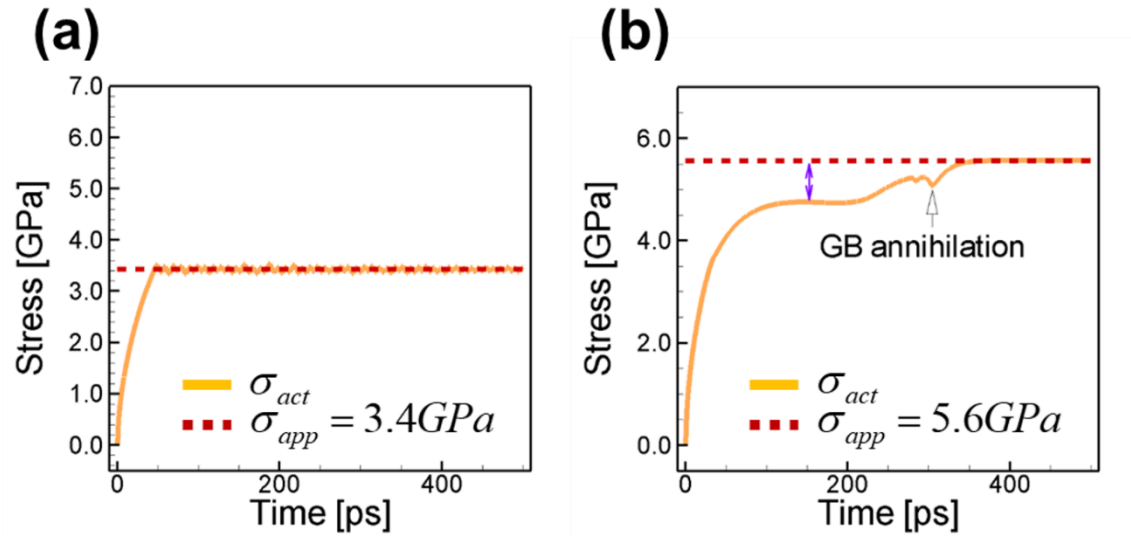

Figure 4.2. Variations in actual stress inside a system with an inserted LAGB that has $\theta = 5.09^\circ$ over simulation time when σ_{app} is applied. Each figure corresponds to (a) when $\sigma_{app} < \sigma_P$ and (b) $\sigma_{app} > \sigma_P$.

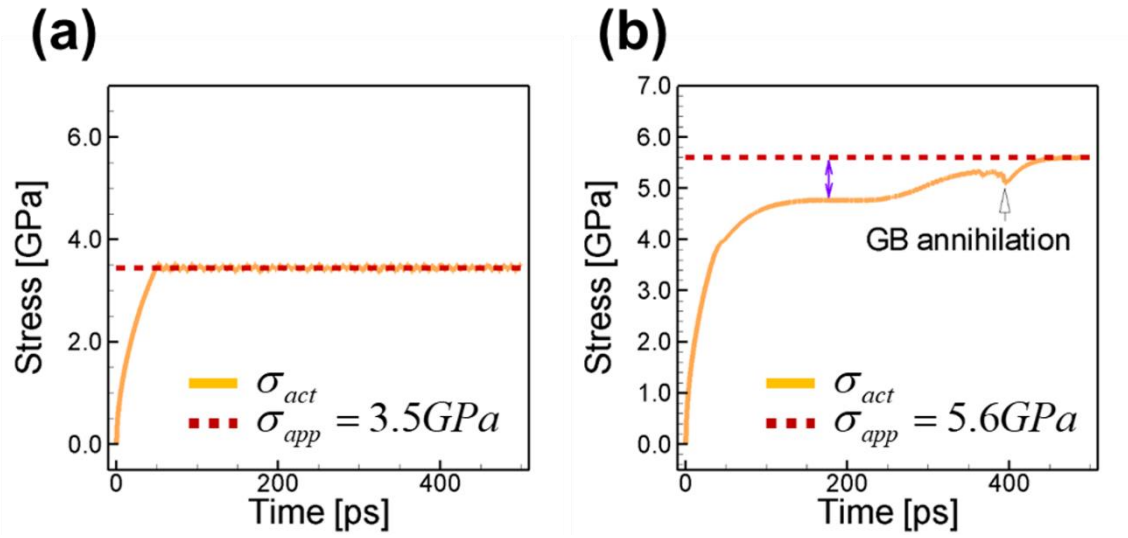

Figure 4.3. Variations in actual stress inside a system with an inserted LAGB that has $\theta = 6.01^\circ$ over simulation time when σ_{app} is applied. Each figure corresponds to (a) when $\sigma_{app} < \sigma_P$ and (b) $\sigma_{app} > \sigma_P$.

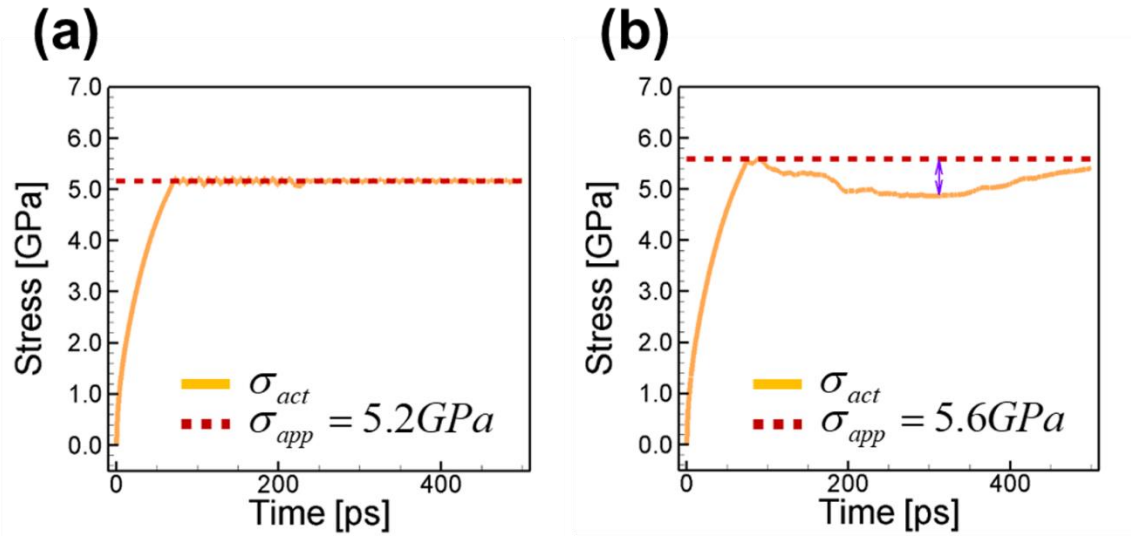

Figure 4.4. Variations in actual stress inside a system with an inserted LAGB that has $\theta = 7.34^\circ$ over simulation time when σ_{app} is applied. Each figure corresponds to (a) when $\sigma_{app} < \sigma_P$ and (b) $\sigma_{app} > \sigma_P$.

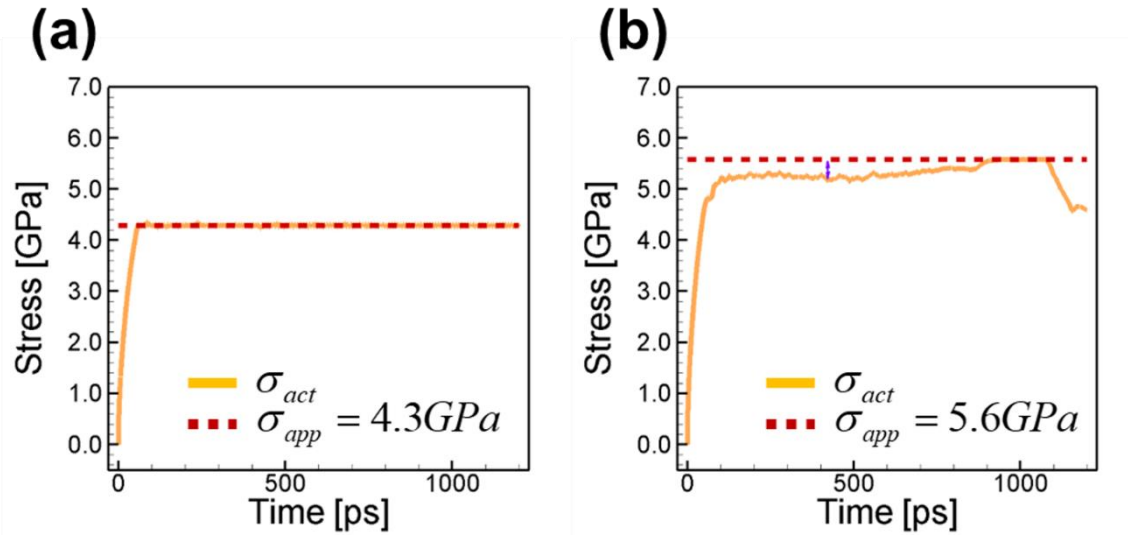

Figure 4.5. Variations in actual stress inside a system with an inserted LAGB that has $\theta = 9.42^\circ$ over simulation time when σ_{app} is applied. Each figure corresponds to (a) when $\sigma_{app} < \sigma_P$ and (b) $\sigma_{app} > \sigma_P$.

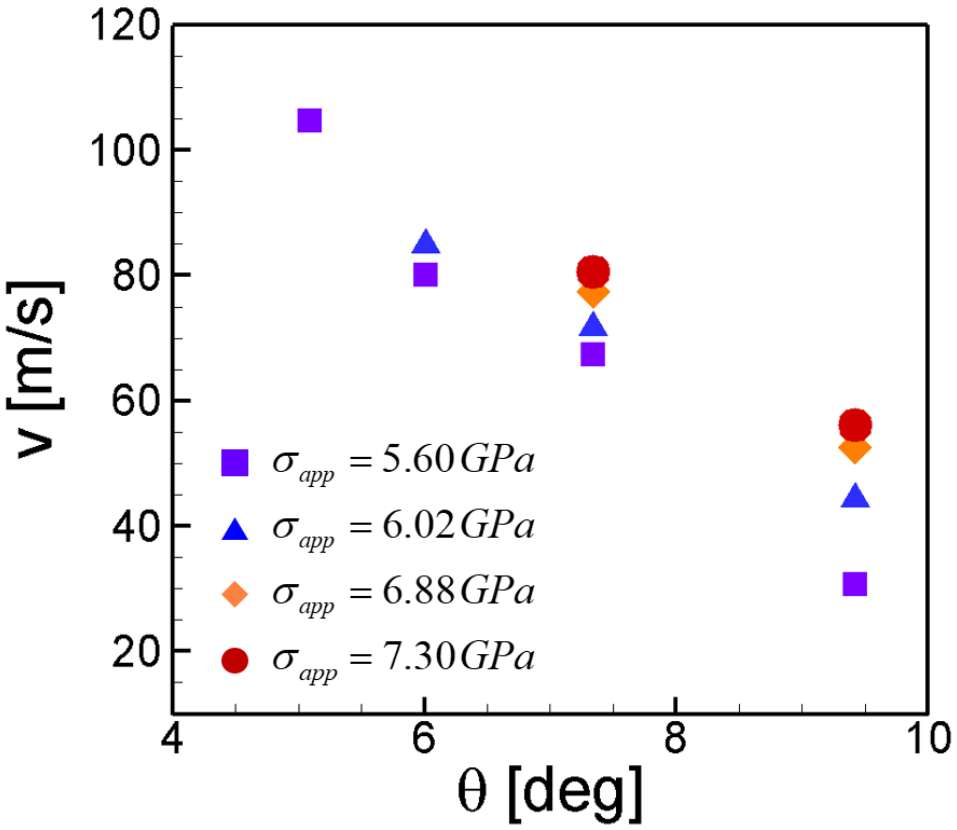

Figure 4.6. Relationship between misorientation angle and LAGB velocity.

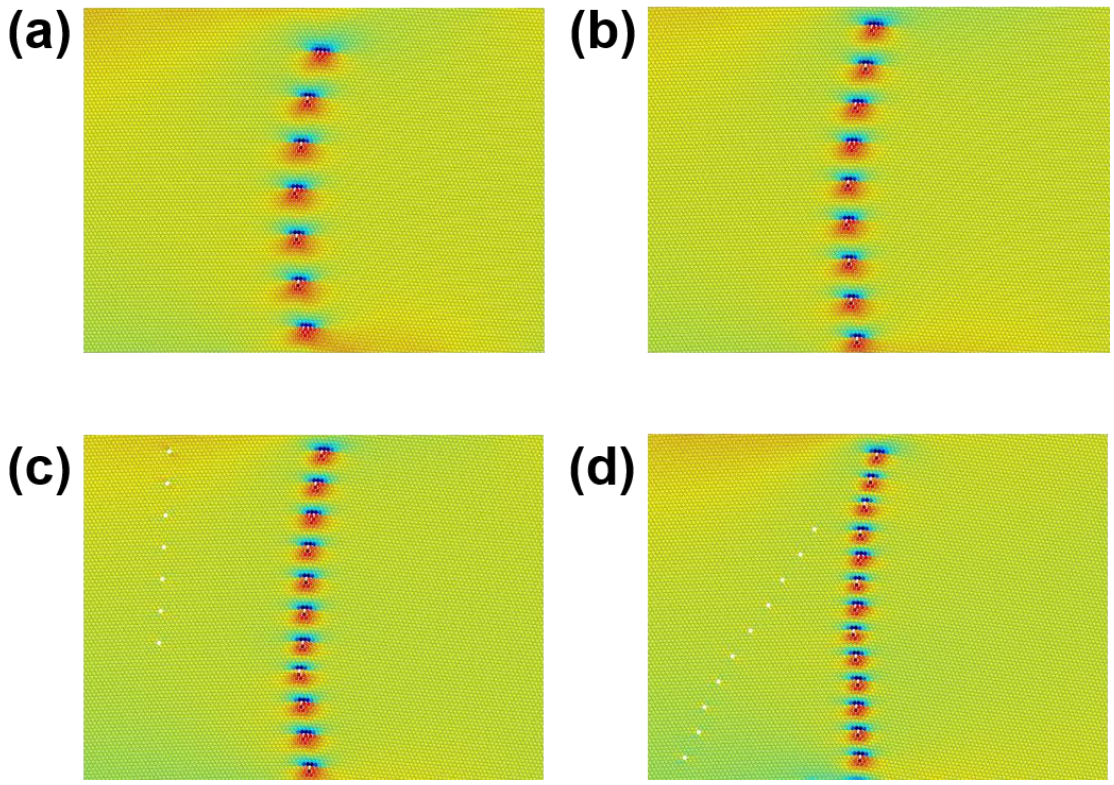

Figure 4.7. Curved shapes of LAGBs in motion by applied stress. Each figure corresponds to (a) $\theta = 5.09°$, (b) $\theta = 6.01°$, (c) $\theta = 7.34°$, and (d) $\theta = 9.42°$.

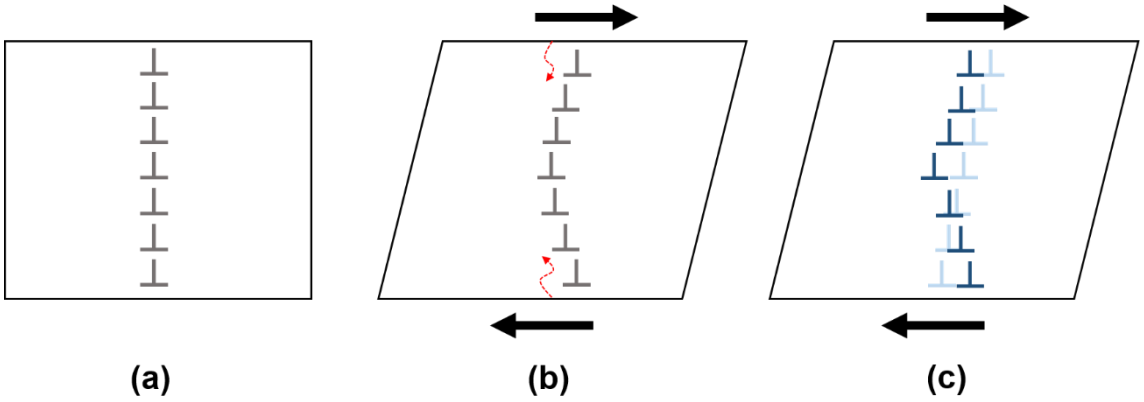

Figure 4.8. Graphical description of the structure of an LAGB at different times under shear stress. (a) Initial state when $\sigma_{app} = 0$. (b) Transition state of the LAGB under $\sigma_{app}(> \sigma_c)$, where σ_c is the critical stress required to move the LAGB. Since the elastic wave supplied by σ_{app} (marked by a red dashed arrow) travels from the free surface to the inside of the system, each dislocation comprising the LAGB begins its motion at a different time. This causes the structure of the LAGB to become curved. (c) The dynamic equilibrium state of the LAGB is marked by dark blue, whereas the sky blue-colored LAGB is the ideal structure expected when only linear elasticity theory is considered.

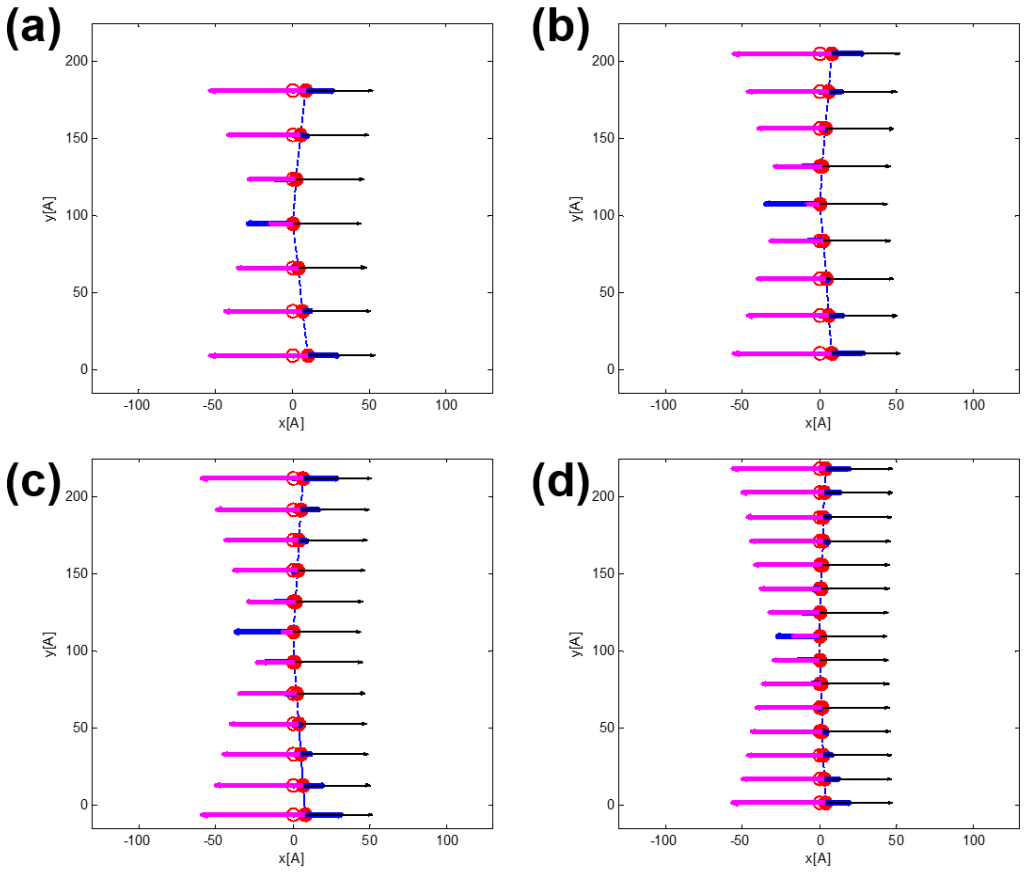

Figure 4.9. Force distributions acting on constituent dislocations of LAGBs for various misorientation angles. Hollow circles represent ideal structures of the LAGBs that are expected by only linear elasticity theory, and filled circles represent actual structures where the drag effect is considered. Black, blue, and purple arrows represent the external load, force from interactions among dislocations, and drag force acting on each dislocation, respectively. The length of the arrows is proportional to the magnitude of the force, and their directions correspond to those of the forces. Each figure describes the LAGB for which (a) $\theta = 5.09°$, (b) $\theta = 6.01°$, (c) $\theta = 7.34°$, and (d) $\theta = 9.42°$.

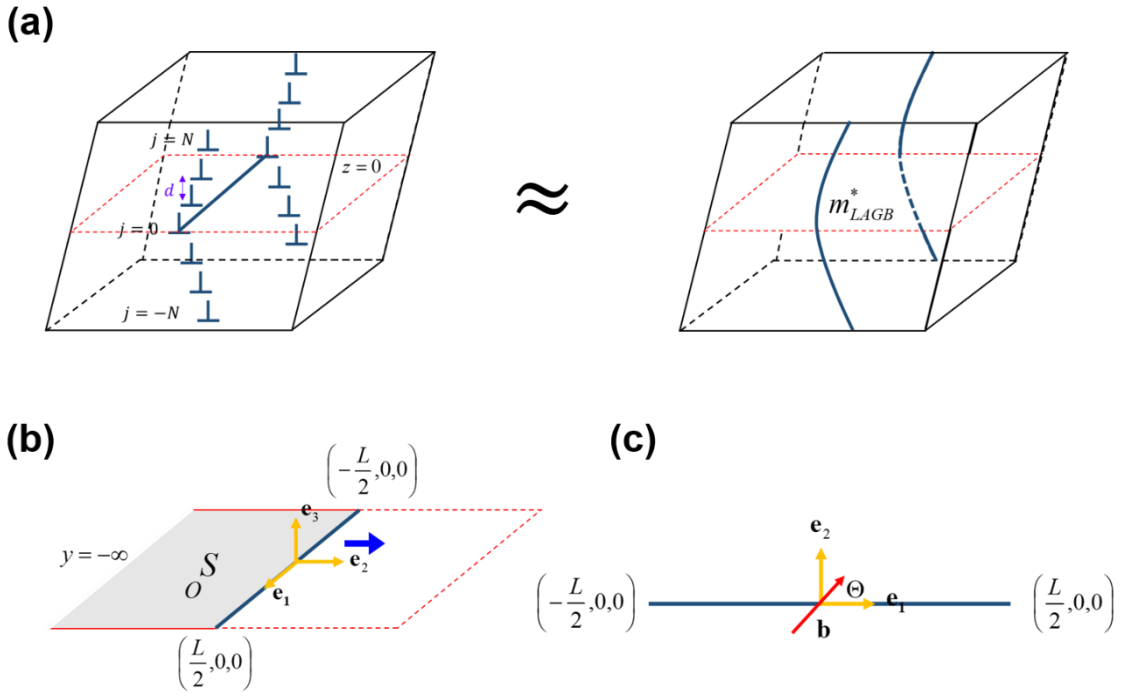

Figure 4.10. (a) Theoretical model of a curved LAGB under external stress. The LAGB consists of $2N+1$ edge dislocations, where the 0^{th} dislocation corresponds to the center of the LAGB. The right figure is an alternative continuum model where the array of dislocations is replaced with an oscillating string whose effective mass per thickness is defined as m^*_{LAGB}. (b) Enlarged configuration of the $z=0$ plane in (a). Note that we used a different coordinate system here than that defined in Fig. 4.1. The shaded region represents an area slipped by the moving dislocation toward the positive *y* direction, and the glide of the dislocation is confined to the *xy* plane. (c) Enlarged configuration of the 0^{th} dislocation in the $z=0$ plane in (b). Here, Θ is the angle between the Burgers vector and the *x* axis, and L is the length of the dislocation.

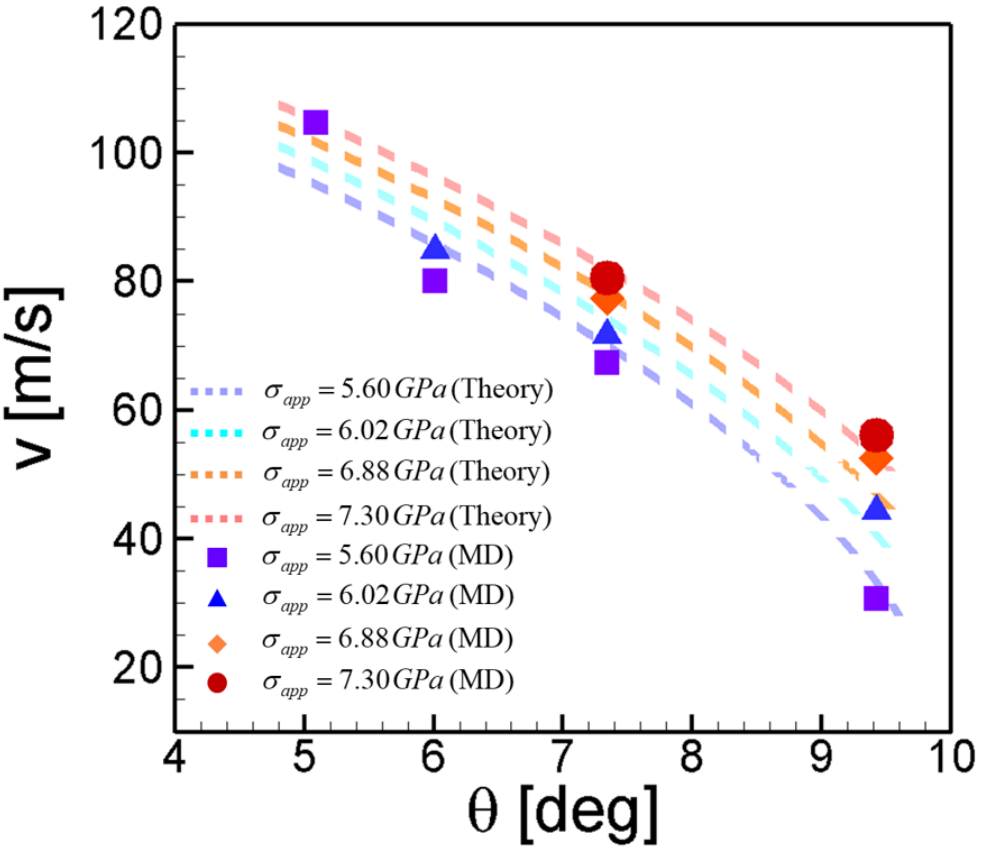

Figure 4.11. Relationship between misorientation angle and LAGB speed. Markers are the results of MD simulations, and dashed lines correspond to theoretical solutions of Eq. (4.6) under different stresses. The input parameters used to solve Eq. (4.6) are summarized in Table 4.1.

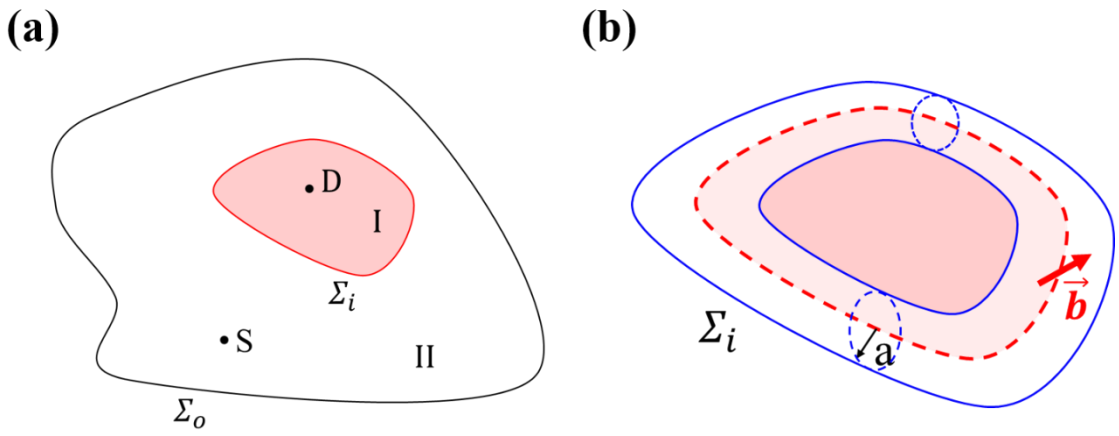

Figure 5.1. (a) A system that includes a dislocation loop *D* in region I and other singularities *S* in region II. (b) Enlarged view of the dislocation loop *D*. Here, the dislocation is surrounded by a cylindrical tube whose radius is a. In both (a) and (b), the shaded region represents slipped area by the dislocation loop.

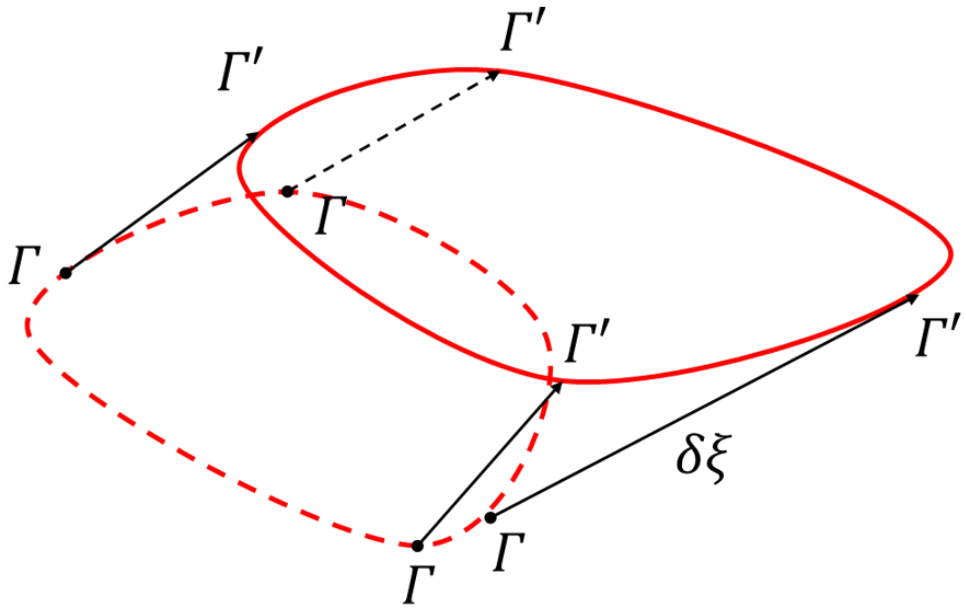

Figure 5.2. A motion of dislocation loop.

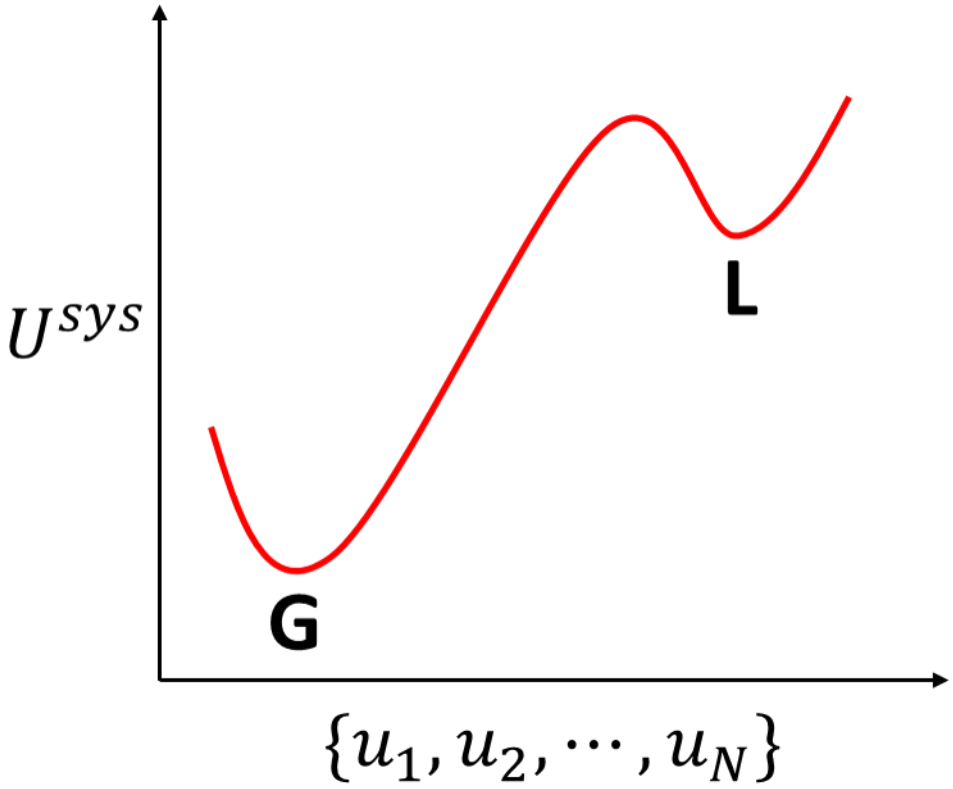

Figure 5.3. Simple description of the N dimensional potential energy surface as a function of atomic displacements. If there is no defect, the system is located at a valley 'G'. In contrast, if the dislocation is inserted, then the system is located at a valley 'L'.

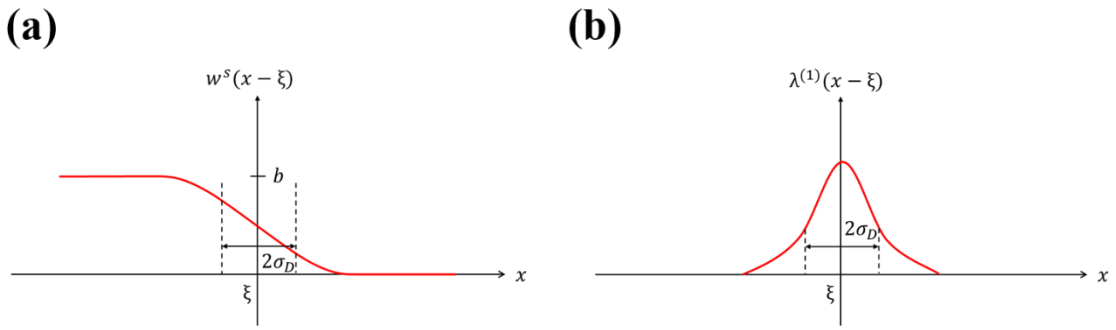

Figure 5.4. (a) Dislocation displacement field under static equilibrium state. (b) Compactness function of the dislocation core. Here, $\lambda^{(1)}(x-\xi) = dw^s/d\xi$ and $\lambda^{(1)}$ is assumed as gaussian distribution function whose mean is ξ and standard deviation is σ_D. We assumed that the dislocation core width is $2\sigma_D$ in this study.

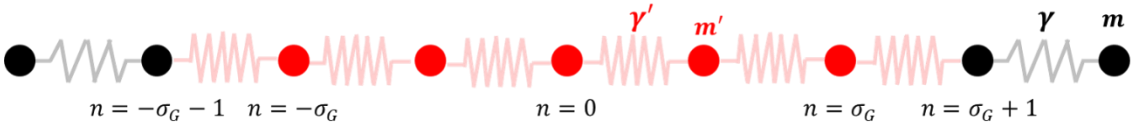

Figure 5.5. Discrete lattice model for dislocation oscillation. Red and black atoms correspond to the atoms inside and outside of the dislocation core, respectively.

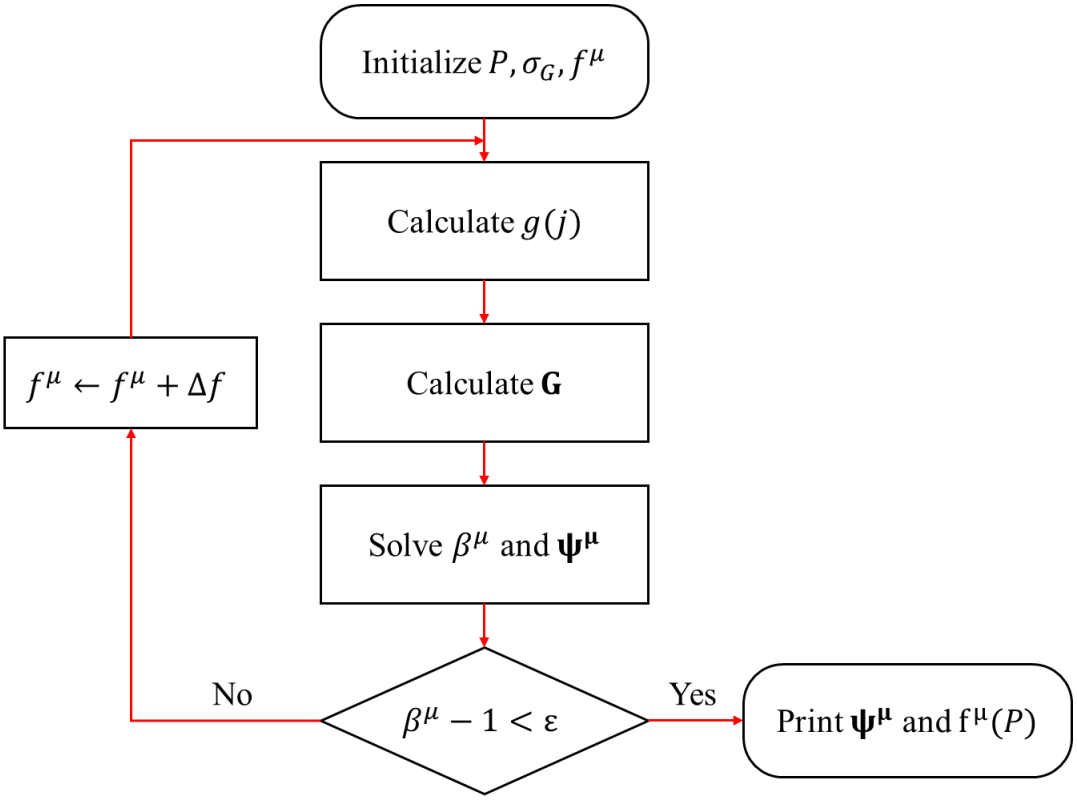

Figure 5.6. A schematic algorithm to find eigenvector and corresponding frequency at given P for mode μ. By repeating this algorithm for every μ, all eigenvectors and frequencies as a function of P can be obtained.

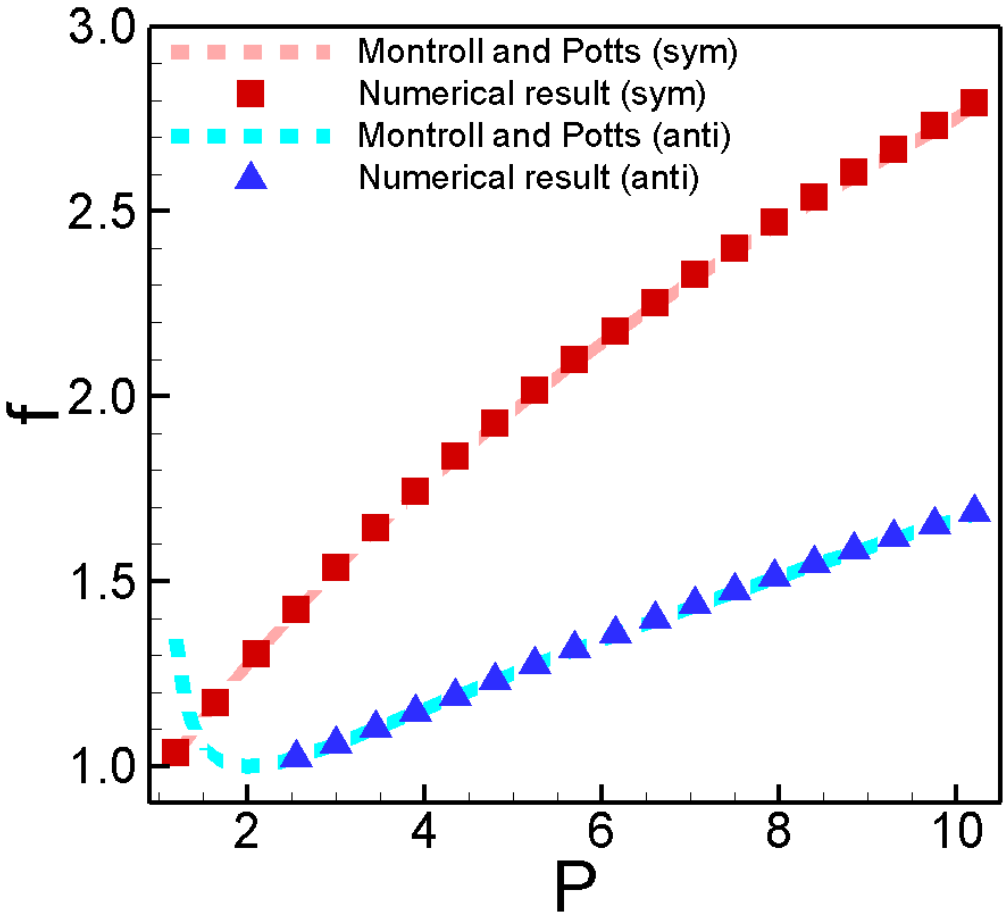

Figure 5.7. The relation between $P(=\gamma'/\gamma)$ and $f(=\omega/\omega_L)$ for $\sigma_G = 0$, or a point defect case. The light red and sky blue dashed lines represent Eq. (5.88) and Eq. (5.90) derived by Montroll and Potts[82], respectively. And the red square and blue triangle are numerical results obtained by solving Eq. (5.73) with the algorithm described in Fig. 5.6. They correspond to symmetric and anti-symmetric modes, respectively.

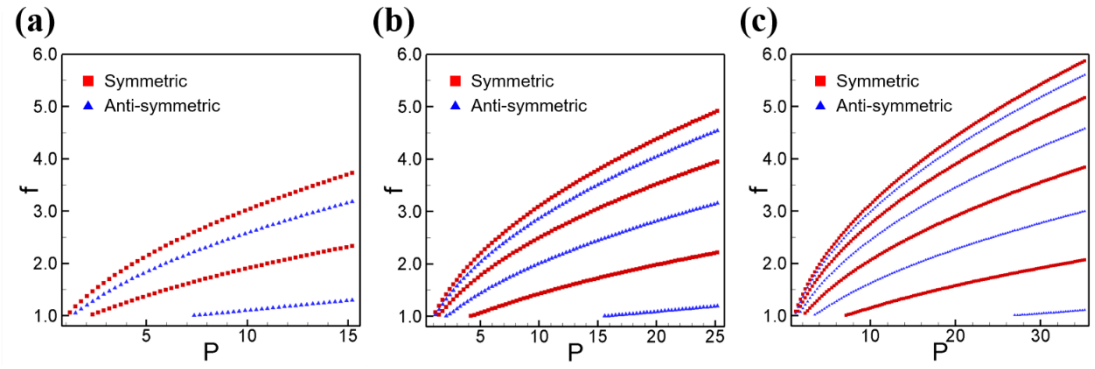

Figure 5.8. The relation between P and f for (a) $\sigma_G = 1$, (b) $\sigma_G = 2$ and (c) $\sigma_G = 3$ that are obtained by solving Eq. (5.73). The red square represents symmetric modes and blue triangle represents anti-symmetric modes.

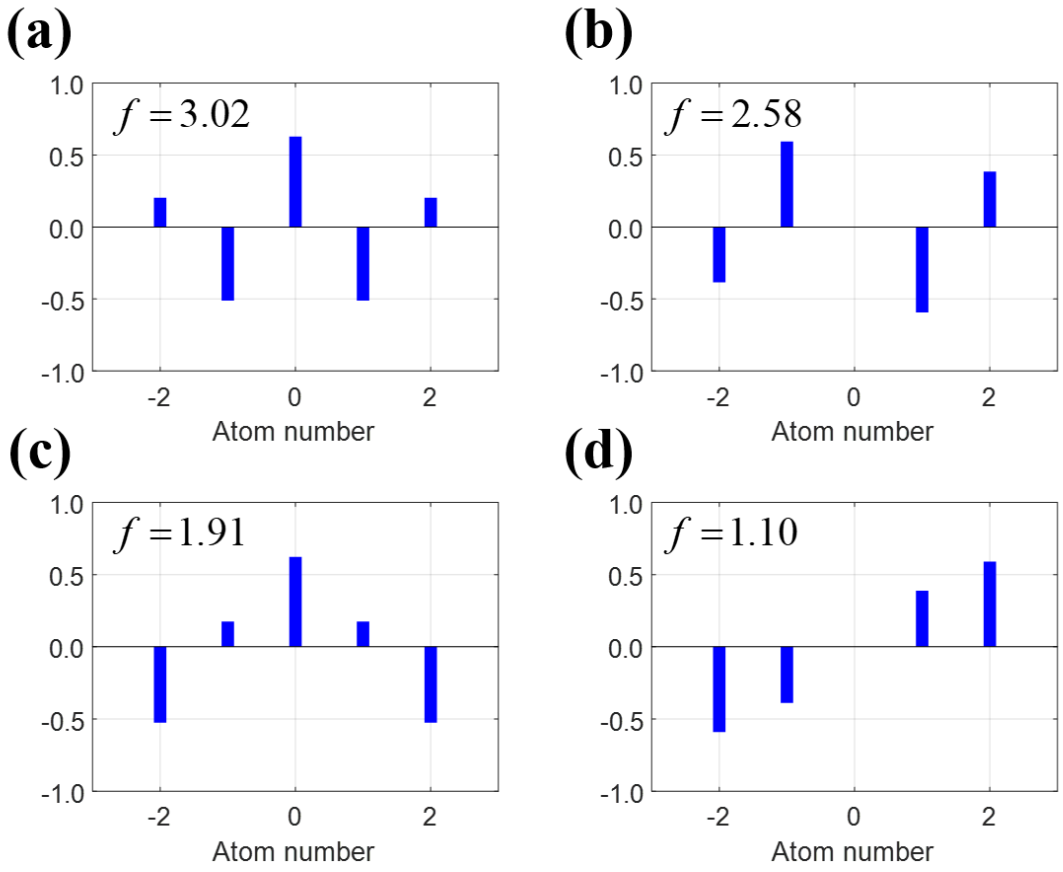

Figure 5.9. Normalized eigenvectors for $\sigma_G = 1$ with $P = 10$. (a) and (c) are symmetric modes and (b) and (d) are anti-symmetric modes.

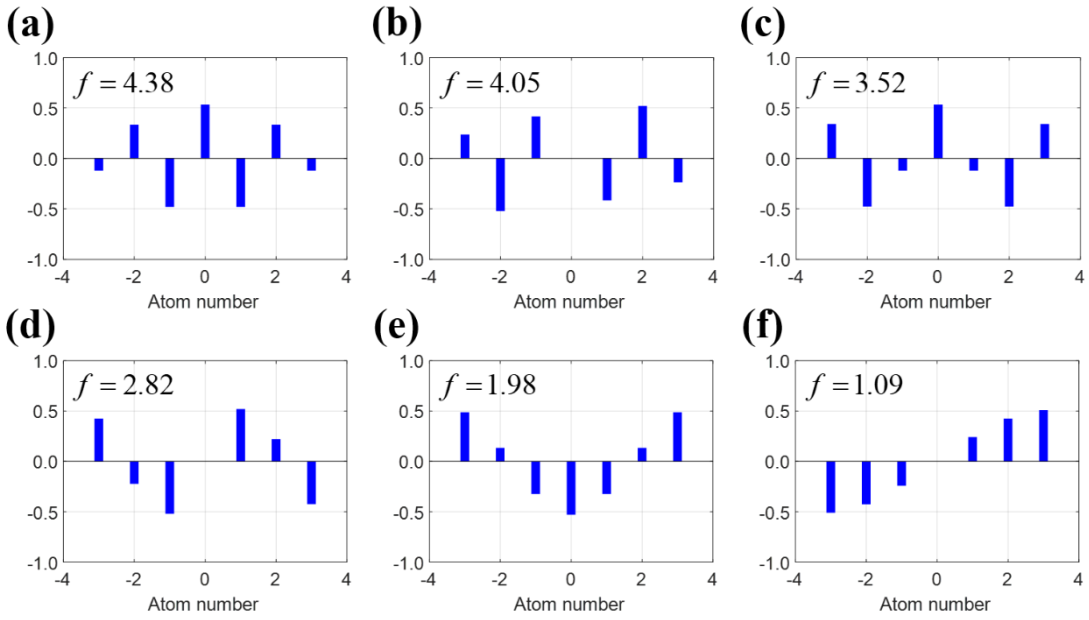

Figure 5.10. Normalized eigenvectors for $\sigma_G = 2$ with $P = 20$. (a), (c) and (e) are symmetric modes and (b), (d) and (f) are anti-symmetric modes.

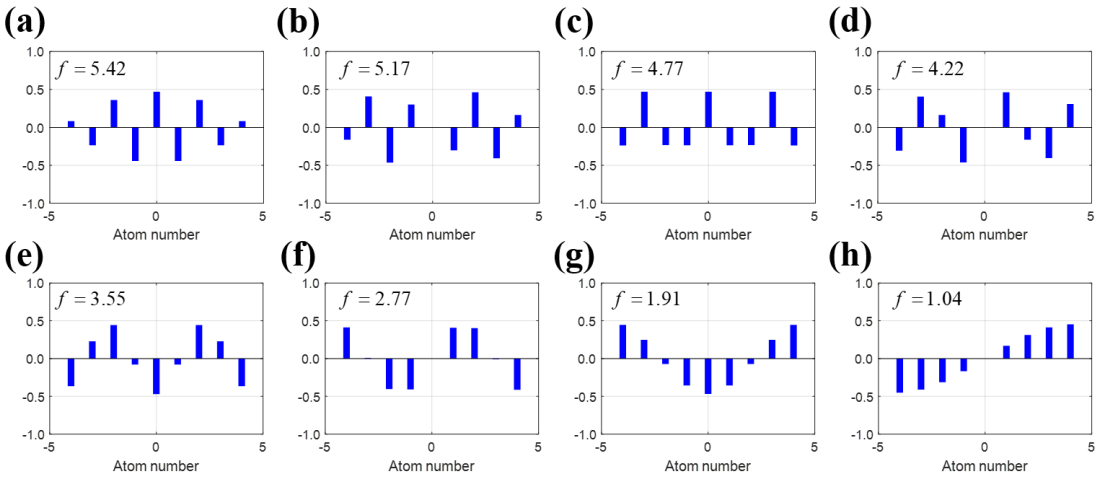

Figure 5.11. Normalized eigenvectors for $\sigma_G = 3$ with $P = 30$. (a), (c), (e) and (g) are symmetric modes and (b), (d), (f) and (h) are anti-symmetric modes.

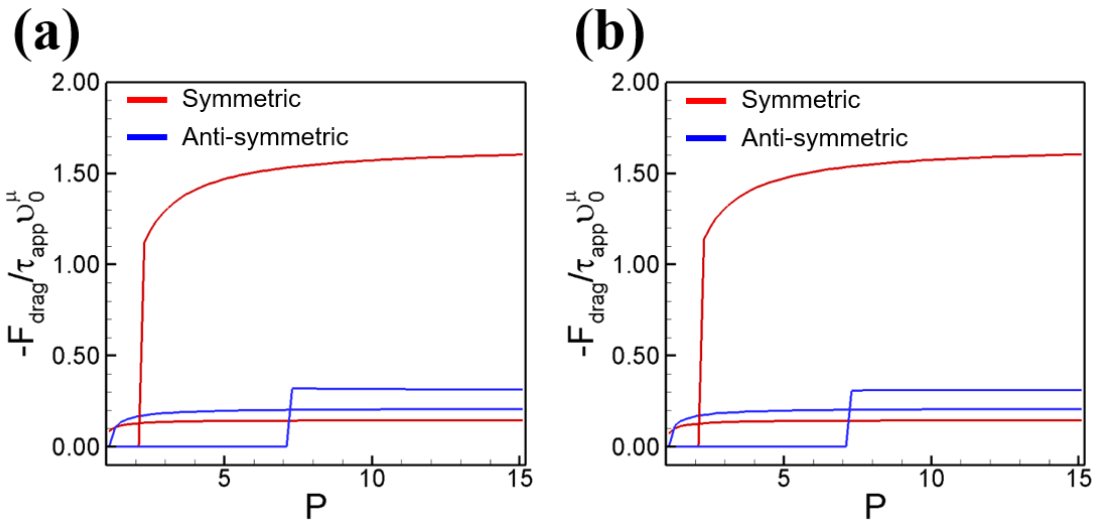

Figure 5.12. Normalized drag force as a function of P for $\sigma_G = 1$ when (a) $R = 2b$ and (b) $R = 8b$. Red and blue lines represent contributions of symmetric and anti-symmetric eigenmodes, respectively. As the eigenmode frequency decreases, it begins to cause the drag at higher P.

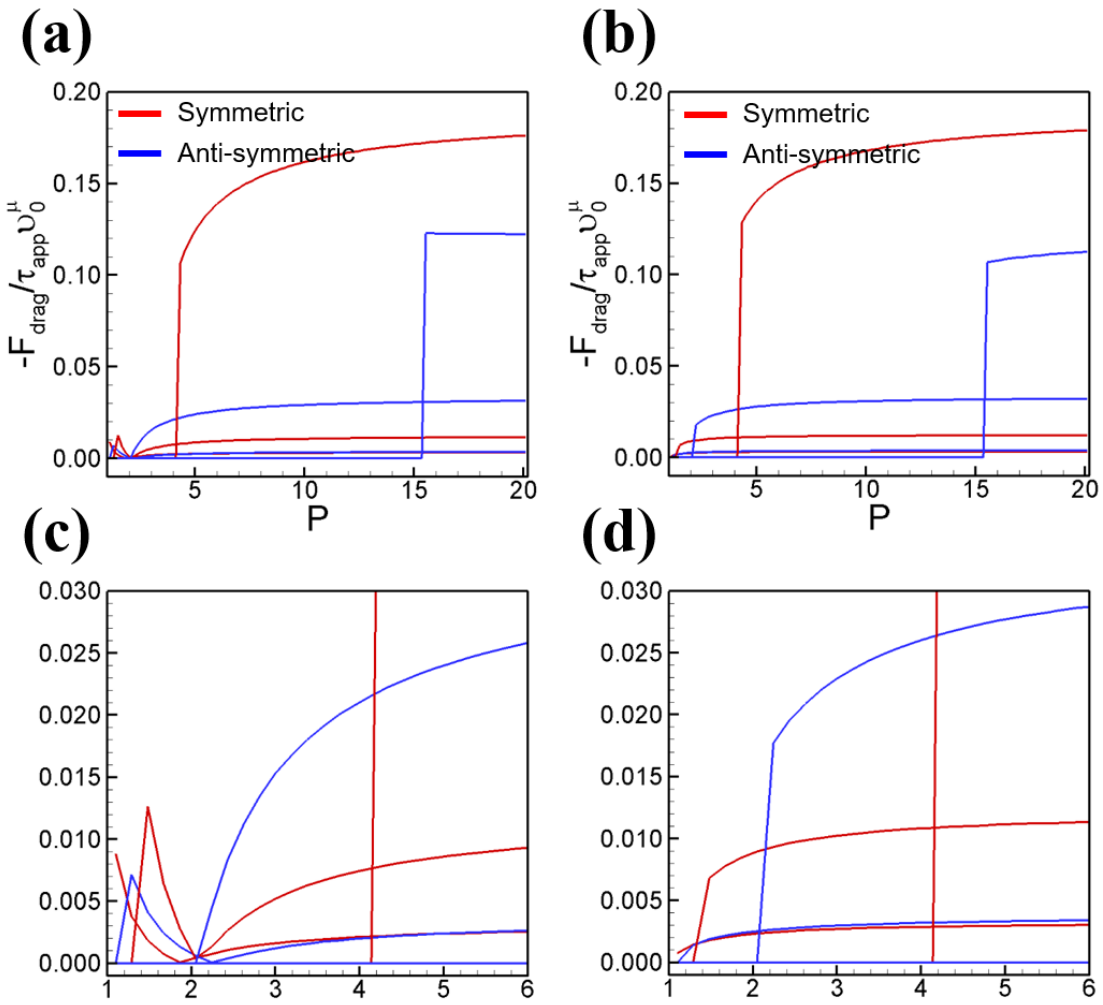

Figure 5.13. Normalized drag force as a function of P for $\sigma_G = 2$ when (a) $R = 3b$ and (b) $R = 9b$. Red and blue lines represent contributions of symmetric and anti-symmetric eigenmodes, respectively. As the frequency of eigenmode decreases, it begins to cause the drag at higher P. (c) and (d) are enlarged figures of (a) and (b) for small P, respectively.

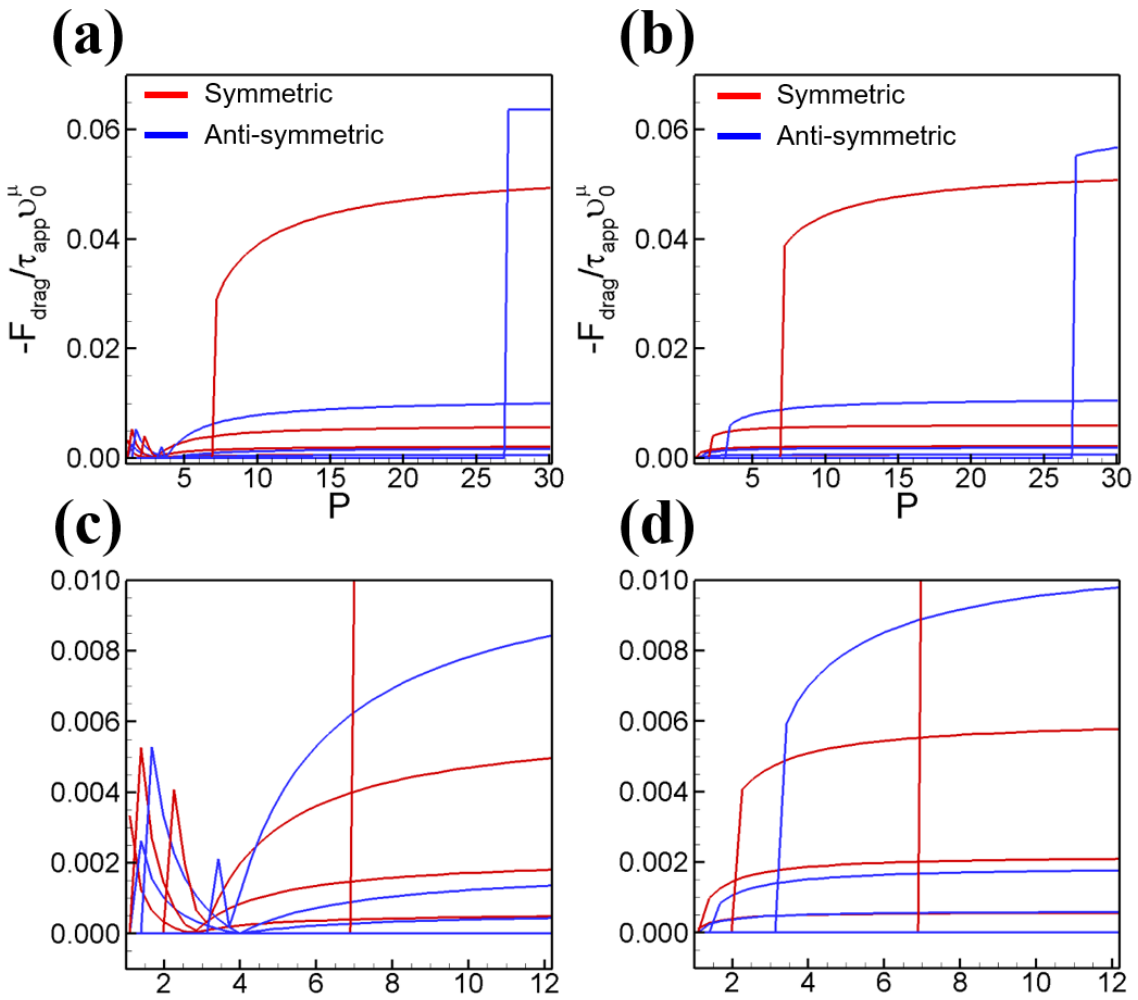

Figure 5.14. Normalized drag force as a function of P for $\sigma_G = 3$ when (a) $R = 4b$ and (b) $R = 10b$. Red and blue lines represent contributions of symmetric and anti-symmetric eigenmodes, respectively. As the frequency of eigenmode decreases, it begins to cause the drag at higher P. (c) and (d) are enlarged figures of (a) and (b) for small P, respectively.

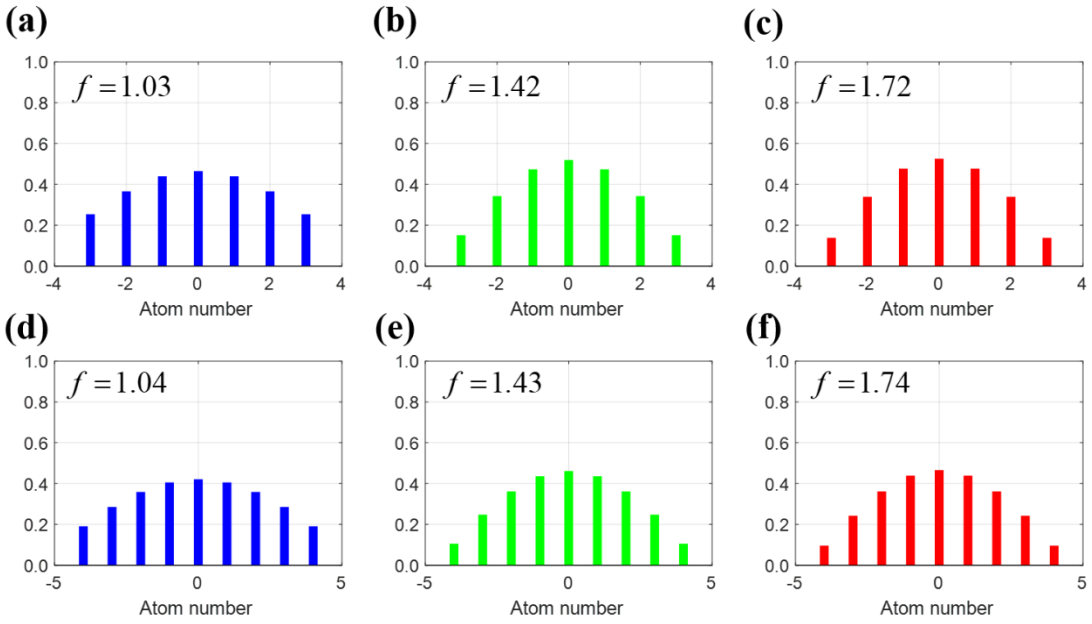

Figure 5.15. Absolute values of normalized eigenvector in mode 1 with changing P. Each figure corresponds to the eigenvector (a) for $\sigma_G = 2$ and $P = 1.1$, (b) for $\sigma_G = 2$ and $P = 2.1$ (c) for $\sigma_G = 2$ and $P = 3.1$, (d) for $\sigma_G = 3$ and $P = 1.1$, (e) for $\sigma_G = 3$ and $P = 2.1$, and (f) for $\sigma_G = 3$ and $P = 3.1$.

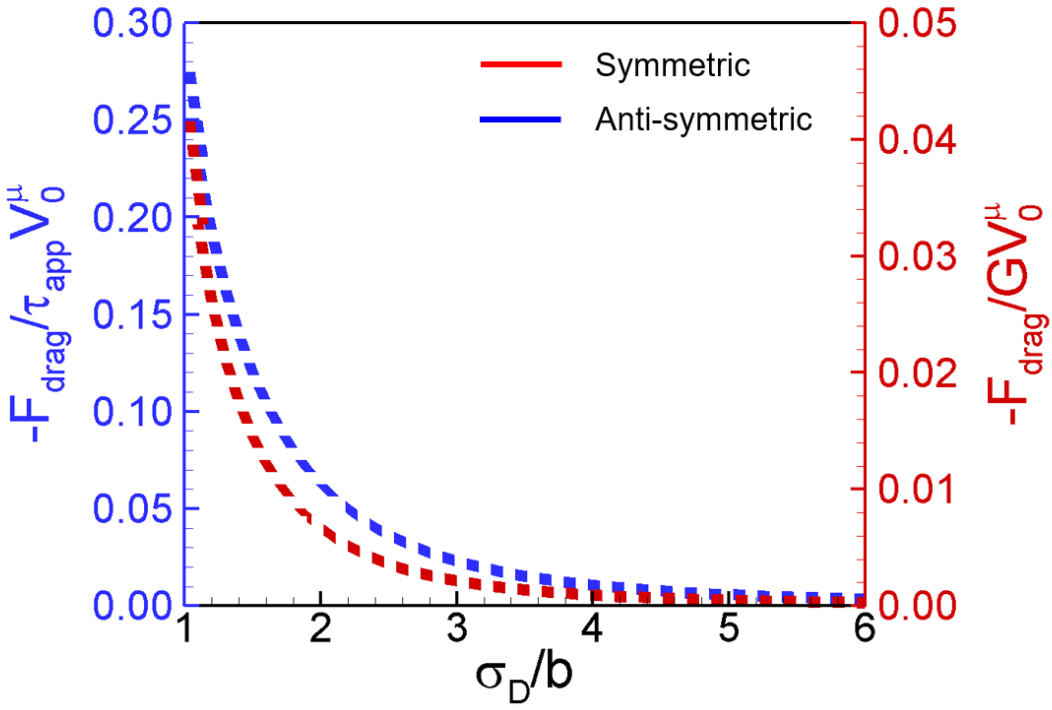

Figure 5.16. Relationship between normalized drag force and core width for symmetric and anti-symmetric modes. Here, $z = 1.00$ is fixed.

ACKNOWLEDGEMENT
(감사의 글)

처음 울산에 내려올 때부터 10년이 지난 지금도 한결같이 아들 걱정해주시는 어머니와 격려해주시는 아버지에게, 그리고 저를 길러 주시고 지금까지도 불편한 몸을 이끌고 매일 손자를 위해 기도해주시는 할머니에게 이 부족한 결실을 바칩니다.

19살의 나이에 처음 울산에 내려와 10대의 마지막과, 20대의 청춘을 전부 언양의 산 속에서 보냈습니다. 그로부터 10년이 지난 지금, 그토록 오랫동안 염원하던 공학 박사가 되어 졸업을 합니다. UNIST 에서의 10년이란 세월은 짧다면 짧고, 길다면 긴 시간이었습니다. 해마다 신입생들이 입학 면접을 보는 광경을 볼 때면, 대학에 입학한 일이 엊그제 일인 것 같다고 느껴지기도 하지만, 각자의 자리로 나아가는 선배와 동기들을 볼 때면 결코 짧지 않은 시간이 흘렀음을 느낍니다. 매일 똑같은 일상의 반복이었지만 저의 대학원 생활을 되돌아보니 많은 어려움이 있었고, 이 어려움과 싸우느라 꽤나 많은 시간을 소비해 온 듯 합니다. 좋은 결실을 맺게 되어 졸업을 하지만, 이로 인해 남게 된 지난날의 아쉬움의 흔적들 또한 기록해보고자 합니다.

대학원 입학 초기 시절, 시간이 흐르면 자연스럽게 학위를 받을 수 있지 않을까 생각하며 어리석게 시간을 버리기도 했었고, 스스로의 무능력함을 대면해 이를 극복하고자 하는 노력 대신 굴복을 택했던 적도 여러 번 있었습니다. 또한 대학원 생활을 오래하면서 캠퍼스 밖 세상 소식에 서서히 둔감해져 연구 외의 모든 것들에 소홀해지는 스스로를 다잡는 데에도 꽤나 어려움이 있었음을 고백합니다. 비록 초라하지만, 오랜 세월 스스로와 싸워 얻어낸 결실이기에, 博士 학위의 무게가 제가 생각했던 것 보다 무겁고 가치 있게 느껴집니다.

지난날의 대학원 생활을 회상하면서 이 지면을 빌어 꼭 인용하고 싶었던 어록이 하나 있습니다. 임진왜란 당시, 첫 해전인 옥포 해전을 앞두고 충무공께서 '勿令妄動 靜重如山'라고 군사들에게 말씀하셨습니다. 당장의 결과에 一喜一悲 하지 말고, 산처럼 무겁게 침착하며 망령되이 움직이지 않는 태도야 말로 저에게 있어서 가장 부족한 능력이요, 학문의 길을 걸어가고자 하는 저에게 가장 필요한 자세가 아닐까 생각되기 때문에 크게 와닿는 듯 합니다. UNIST 에서의 10년간의 경험이 바로 이러한 마음가짐을 배우는데 걸렸던 세월이었습니다.

이러한 스스로의 반성과 깨우침을 넘어, 많은 이들로부터 도움과 격려를 받았기에

글로나마 이들에게 고마운 마음을 전합니다. 우선, 저의 학위 논문 심사위원으로 참석해주셨던 기계공학과의 정하영 교수님과 오주환 교수님, 재료과의 신형준 교수님께 감사의 말씀을 드립니다. 또한 학위과정 내내 연구는 물론이고 연구 외적인 측면에서도 제게 많은 조언과 도움을 주셨던 KAIST의 유승화 교수님, 연세대의 강건욱 교수님께도 너무나 감사드립니다. 그리고 무엇보다도, 이 모든 인연이 있게 해준 분 이시자 학자로서 제가 나아가는 방향을 제시해주신 김성엽 지도교수님께 무한한 감사와 존경을 표합니다. 교수님의 가르침 덕에, 연구자로서 무언가 있어 보이는 것 보단 本質 그 자체에 집중하고, 단순한 결과 해석이나 수식 유도를 넘어 근본적인 원인과 물리적인 의미를 끄집어내는 능력을 기를 수 있었습니다. 이러한 깊은 배움의 과정으로 인해, 결과를 내기까지 오랜 시간이 걸렸지만 끝까지 저를 믿고 아낌없이 지원과 격려를 해주신 교수님의 안목과 인품 또한 제자인 저에게 훌륭한 귀감이 되었습니다. 다시 한번 감사드립니다.

그리고 지난 6년간 가장 많은 시간을 보낸 우리 CAN 랩 식구들에게도 감사의 말을 전합니다. 저와 대학/대학원 동기이자, 연구를 넘어 정치, 사회, 이념 등등의 문제에 대해 수없이 토론하면서 같이 지내온 (사실상 연구를 제외하곤 모든 점에서 저와 반대 의견을 가지고 있는) 호건이형, 교수님을 대신해서 항상 핵심적인 질문을 던져 저를 당황케 하고 매사에 언제나 열정적으로 임해 제게 모범이 되었던 덕탐이형, 랩의 맏형이자 리눅스를 장난감 다루듯이 다루지만 모순적으로 조선시대 선비의 삶을 동경했던 순동이형, 한동안 랩을 먹여 살렸던 과제대장이자 츤데레인 재형이형, 술과 잠을 가까이 하면서도 실력만 있다면 졸업할 수 있다는 것을 보여줘 제게 신선한(?) 충격을 안겨준 진정한 능력자 준호와 이 정신을 이어받은 CAN 랩의 홍일점 지은이에게도 감사의 말을 전합니다. 그리고 앞으로 몇 년간 머신러닝을 연구하며 CAN 랩의 미래를 책임지게 될 현석이와 올 한해 어려운 일들이 많이 있었지만 꿋꿋이 이겨내 다시 미소를 찾은 원호에게 감사를 전함과 동시에 남은 기간 성공적인 대학원 생활을 기원합니다. 또한 타랩임에도 자주 우리 랩에 놀러와 신선한 분위기를 불어놓고 가시는 인간 활력제 창윤이형게도 감사의 말을 꼭 전하고 싶습니다.

더 나아가, 저와 고등학교 때부터 12년의 세월을 함께해 온 세종의 친구들에게도 감사의 말을 남깁니다. 대학 재학시절 항상 같이 붙어 다녔던 수영 중독자 준일이, 동기들 중 가장 대학원 갈 것 같이 생겼으면서 가장 먼저 취업해버린 컴퓨터 천재 (모순왕) 인식이, 물리를 전공하는 것도 모자라 물리 동아리까지 가입해버린 진정한 물리학자 영상이에게도 고맙다는 말을 전합니다. 그리고 고등학교 시절 수학을 그토록 싫어했으면서, 저와 같이 대학원에 진학해 (본인은 부인하지만) 통계를 전공해버린 진환이에게 글을 조금 더 남깁니다. 매일 학생 식당과 구영리의 이곳저곳을 돌아다니며 같이 밥을 먹었던 기억은 소박하지만 제 대학원 생활 중 가장 기억에 남는 추억으로 남을 듯 합니다. 세종의 친구들에게도 각자의 길에서 밝은 미래가 함께하길 기원합니다.

마지막으로, 저의 가장 든든한 후원자인 가족들에게 이 지면을 빌어 글을 남깁니다. 어느덧 타지생활을 한지도 10년이 넘었고, 앞으로 제가 가고자 하는 길 역시 홀로 걸어가야 할 테지만, 그럼에도 불구하고 항상 저를 응원해주시고 격려해 주시

는 부모님과 할머니에게 감사함과 동시에 미안한 마음을 감출 수 가 없습니다. 표현이 서툰 저이지만 항상 감사하고 사랑합니다. 또한 가족들뿐만이 아니라 저 역시 나이를 먹었기에 처음 울산에 내려왔을 당시 가졌던 10대의 패기는 이제 얼마 남아 있지 않지만, 20대 동안 쌓아왔던 경험으로 무장하여 앞으로 나아가고자 합니다.

2019年 12月 17日

工學博士 金淳